Technische
Universität
Braunschweig

emg

Tilman Sumpf

Model-based T_2 Relaxometry using Undersampled Magnetic Resonance Imaging

Dissertation
Braunschweig 2012

Berichte aus dem **Institut für Elektrische Messtechnik und Grundlagen der Elektrotechnik**

Hrsg. Prof. Dr. Meinhard Schilling

Band 43

Model-based T_2 Relaxometry using Undersampled Magnetic Resonance Imaging

Von der Fakultät für Elektrotechnik, Informationstechnik, Physik
der Technischen Universität Carolo-Wilhelmina zu Braunschweig

zur Erlangung der Würde

eines Doktor-Ingenieurs (Dr.-Ing.)

genehmigte Dissertation

von

Tilman Sumpf

aus Aachen

eingereicht am:	09.08.2012
Referent:	Prof. Dr. M. Schilling
Koreferent:	Prof. Dr. J. Frahm
Tag der mündlichen Prüfung:	11.12.2012

2012

Abstract

T_2 relaxometry refers to the quantitative determination of spin-spin relaxation times in magnetic resonance imaging (MRI). Particularly in clinical diagnostics, the method provides important information about tissue structures and respective pathologic alterations. Unfortunately, it also requires comparatively long measurement times which preclude widespread practical applications. To overcome such limitations, a so-called model-based reconstruction concept has recently been proposed. The method allows for the estimation of spin-density and T_2 parameter maps from only a fraction of the usually required data. So far, promising results have been reported for a radial data acquisition scheme. However, due to technical reasons, radial imaging is only available on a very limited number of MRI systems.

The present work deals with the realization and evaluation of different model-based T_2 reconstruction methods that are applicable for the most widely available Cartesian (rectilinear) acquisition scheme. The initial implementation is based on the conventional assumption of a mono-exponential T_2 signal decay. A suitable sampling scheme as well as an automatic scaling procedure are developed, which remove the necessity of manual parameter tuning. As demonstrated for human brain MRI data, the technique allows for a more than 5-fold acceleration of the underlying data acquisition. Furthermore, general limitations and specific error sources are identified and suitable simulation programs are developed for their detailed analysis. In addition to phase variations in image space, the simulations reveal truncation effects as a relevant cause of reconstruction artifacts. To reduce the latter, an alternative model formulation is developed and tested. For noise-free simulated data, the method yields an almost complete suppression of associated artifacts. Residual problems in the reconstruction of experimental MRI data point to the predominant influence of other errors in practice.

The last part of this thesis focuses on the development of a refined T_2 reconstruction technique which employs a signal model that considers contributions from stimulated echoes to the spin-echo signal. The method yields an increased accuracy of the estimated T_2 relaxation times. In comparison, however, the mono-exponential model proves to be less sensitive to artifacts when the data acquisition is highly accelerated. This T_2 relaxometry method is currently evaluated in a first clinical trial.

Zusammenfassung

Der Begriff der T_2 Relaxometrie umfasst die quantitative Bestimmung der Spin-Spin Relaxationszeit in der Magnetresonanz-Tomografie (MRT). Insbesondere in der medizinischen Bildgebung liefert das Verfahren wichtige Aufschlüsse über Gewebestrukturen und ihre Veränderungen, erfordert jedoch verhältnismäßig lange Messzeiten. Zur Überwindung der damit einhergehenden praktischen Einschränkungen wurde kürzlich ein sogenanntes modellbasiertes Rekonstruktionsverfahren vorgeschlagen, das zwei Parameterkarten der Spindichteverteilung und der T_2 Relaxationszeit aus einem Bruchteil der konventionell erforderlichen Datenmenge berechnen kann. Erste vielversprechende Ergebnisse wurden bisher jedoch nur in Verbindung mit einem radialen Abtastschema beschrieben, das aufgrund technischer Komplikationen nur in wenigen MRT-Systemen zur Verfügung steht.

Die vorliegende Arbeit befasst sich mit der Umsetzung und Erprobung modellbasierter T_2 Rekonstruktionstechniken für die in der Praxis vorherrschende kartesische Datenerfassung. Hierzu wird zunächst ein Rekonstruktionskonzept aufgegriffen, das auf dem klinisch weitverbreiteten mono-exponentiellen Signalmodell basiert. Ein geeignetes Abtastschema sowie eine automatische Skalierungstechnik werden entwickelt, deren Kombination das Verfahren erstmalig unabhängig von manuellen Parameteranpassungen macht. Wie anhand von experimentellen Daten demonstriert wird, lässt sich die Datenaufnahme dabei mehr als 5-fach beschleunigen. Weitergehend werden Störeinflüsse und Limitierungen aufgezeigt und zu deren genauerer Analyse spezifische Simulationsprogramme entwickelt. Neben Phasenvariationen im Bildraum zeigen die Simulationen auch Diskretisierungseffekte als eine Ursache von Rekonstruktionsartefakten auf. Zur Reduzierung letzterer wird eine alternative Modellformulierung entwickelt und geprüft. Das Verfahren führt bei rauschfreien simulierten Daten zu einer fast vollständigen Unterdrückung zugehöriger Artefakte. Verbleibende Fehler bei der Rekonstruktion experimenteller MRT-Daten weisen gleichzeitig auf den überwiegenden Einfluss anderer Störquellen in der praktischen Umsetzung.

Der letzte Teil der Arbeit befasst sich mit der Entwicklung einer modellbasierten Rekonstruktion auf der Grundlage eines Signalmodells, das Beiträge von stimulierten Echos in den Spin-Echo-Signalen berücksichtigt. Hiermit lässt sich die Genauigkeit der ermittelten T_2 Relaxationszeiten erhöhen. Im Vergleich erweist sich allerdings das mono-exponentielle Modell bei hoher Akquisitionsbeschleunigung als weniger artefaktanfällig. Das Verfahren findet derzeit Eingang in eine erste klinische Erprobung.

Contents

Abstract **iii**

Zusammenfassung **v**

1 Introduction **1**

2 Magnetic resonance imaging **5**

2.1 Nuclear spins and magnetization 5
  2.1.1 Excitation and reception 7
  2.1.2 Relaxation and Bloch equations 8
  2.1.3 Free induction decay and spin echo 9
  2.1.4 Stimulated echoes 10
2.2 Spatial encoding 11
  2.2.1 Magnetic field gradients 11
  2.2.2 Slice selection 12
  2.2.3 Fourier encoding 13
  2.2.4 Sampling of k-space 14
  2.2.5 Non-Cartesian trajectories 15
2.3 Array coils 16
2.4 Imaging sequence and measurement time 18
2.5 Contrast mechanisms and T_2 relaxometry 19
  2.5.1 T_2 weighting 19
  2.5.2 T_2 relaxometry 20

3 Image reconstruction **21**

3.1 Image reconstruction as a linear inverse problem 21
  3.1.1 Parallel imaging 22
  3.1.2 Iterative reconstruction 24
  3.1.3 Estimation of coil sensitivity profiles 25
3.2 Parallel imaging as a nonlinear inverse problem 26
3.3 Advanced image reconstruction models 27

4 Simulations **29**
4.1 Data discretization and truncation artifacts 29
4.2 Pixel-based phantoms 33
  4.2.1 Oversampling 34
4.3 Analytical phantoms 34
  4.3.1 Elliptical primitives 35
4.4 Shepp-Logan phantom 35
4.5 Relaxation 36
4.6 Transition between discrete and continuous space 36
4.7 Partial volume effects 37

5 Model-based T_2 relaxometry from undersampled Cartesian data **39**
5.1 Data acquisition 40
  5.1.1 CPMG sequence 40
  5.1.2 Fast spin echo sequence 42
5.2 T_2 reconstruction as a nonlinear inverse problem 43
  5.2.1 Undersampling 44
  5.2.2 Multiple receiver coils 46
  5.2.3 Phase 46
  5.2.4 Optimization and gradient scaling 47
  5.2.5 Implementation 48
5.3 Results 49
  5.3.1 Reconstructions from simulated ideal data 49
  5.3.2 Undersampling scheme 52
  5.3.3 The effect of poor gradient scaling 55
  5.3.4 Quantitative accuracy 56
  5.3.5 Imperfection of the CPMG echo train 60
  5.3.6 Human brain reconstructions at different acceleration factors . . 61
  5.3.7 Parallel imaging 67

6 Model violations **69**
6.1 Multi-exponential signal decay 70
  6.1.1 Materials and methods 70
  6.1.2 Results 70
  6.1.3 Discussion 72
6.2 Image phase alternations 74
  6.2.1 Materials and methods 74
  6.2.2 Results 75
  6.2.3 Discussion 77
6.3 A note on accelerated high-field animal MRI 79

7 Truncation and convolution errors **81**

7.1 The effects of circular convolutions 82

7.1.1 Theory 82

7.1.2 Materials and methods 84

7.1.3 Results 85

7.2 Model adaption 88

7.2.1 Theory 88

7.2.2 Error distribution at the ideal estimate 89

7.2.3 Reconstruction algorithm 89

7.2.4 Gradient scaling 91

7.2.5 Initial guess 91

7.2.6 Initialization 92

7.2.7 Results 92

7.2.8 Discussion 96

8 Model-based T_2 relaxometry using the generating function formalism **99**

8.1 Theory 100

8.1.1 Aliasing in z-direction 101

8.1.2 Reconstruction from undersampled data 102

8.1.3 Optimization and gradient scaling 103

8.2 Simulations 103

8.3 Results 104

8.3.1 Adaptive scaling 104

8.3.2 SNR comparison 105

8.3.3 Human brain MRI 107

8.4 Discussion 112

9 Summary and Outlook **113**

9.1 Summary 113

9.2 Future work 115

A Appendix **117**

A.1 Derivatives of the model consistency term for k-MARTINI 117

Abbreviations **122**

Bibliography **132**

Curriculum Vitae **133**

List of Publications **135**

Acknowledgments **137**

1

Introduction

In 1973, Paul Lauterbur [1] demonstrated how the effect of spatially varying magnetic fields on the nuclear spin property may be exploited to acquire images of the proton-density distribution in living objects. Since then, the non-invasive *magnetic resonance imaging* (MRI) technique has evolved to one of the leading tools in biomedical research and clinical diagnostics. The possibility to measure excited spins at different stages of their inherent relaxation process allows for variations of the contrast between different structures. Further, the acquisition of multiple contrasts from the same anatomical region enables the capability to calculate quantitative maps of the underlying relaxation parameters and to classify different tissue types. These properties in combination with the absence of ionizing radiation constitute the major advantages of MRI compared to alternative imaging methods such as X-ray computed tomography (CT) or positron emission tomography (PET). On the other hand, as a drawback compared to optical methods, the acquisition of MR images still comes at the expense of relatively long acquisition times. These time requirements may cause practical limitations, particularly as the avoidance of motion during measurements is crucial for accurate reconstructions. Acceleration of the acquisition process is therefore of major interest for clinical MRI.

Addressing these demands, so-called *parallel imaging* (PI) techniques have been established during the last decade. By exploiting complementary spatial information from multiple receiver coils, related methods allow for a reduction of spatial encoding steps in conventional imaging sequences and as a consequence lead to a reduction of scan time. Unfortunately, these techniques rely on the availability of multiple receiver coils with different spatial sensitivity profiles. In most current systems and for two-dimensional imaging, the net acceleration in PI is therefore usually limited to a factor of 2 - 3. A further drawback of most acceleration techniques is the inherent loss of signal-to-noise ratio (SNR), which can especially be fatal for animal MRI studies which often lack sufficient SNR. On the other hand, when calculating quantitative maps of relaxation parameters, a lot of redundancy may be found in the data of image series with different contrasts. Exploiting such redundancies with the use of *model-based reconstructions* will be the major topic of this thesis. Specifically with respect to T_2 relaxometry, the work by Block et al. [2] demonstrated successful application of a model-based reconstruction method that allows for scan-time acceleration far beyond classical restrictions. However, the previous proof-of-principle implementation imposes several limitations. Especially at low-priced MRI systems, a major issue arises from the use of radial data acquisition schemes. Even though theoretically advantageous, these schemes are also prone to gradient imperfections and are therefore only available on few clinical systems. In combination with the proposed data interpolation steps, the scheme also requires an additional regularization which has to be tuned appropriately. A further limitation with regard to its practical feasibility is the dependency on a heuristically chosen scaling factor, which has to be adapted for different anatomical regions or sources of data.

A major goal of the present work is to further develop the principle outlined by Block et al. [2] towards clinical applicability and routine use. The radial trajectories are therefore replaced by Cartesian acquisition schemes, which are in widespread use in clinical applications. An automatic scaling procedure is developed to remove the necessity of manual parameter tuning. Furthermore, a suitable sampling pattern is proposed to avoid artifacts in the reconstruction and to remove the need for additional regularization terms. The method is then tested towards different data imperfections. Several data simulation routines are developed to understand the limits of the method and to reveal the origin of remaining reconstruction artifacts[1]. Based on the findings, alternative model formulations are evaluated to address the elaborated obstacles.

The initial chapter (Chapter 2) will give a brief overview of the basic principles of MRI which are necessary for the understanding of the later methods. The treatise will focus on spin-echo acquisitions, as those are fundamental to all T_2 parameter-mapping techniques. Chapter 3 introduces the formulation of image reconstruction as linear and nonlinear inverse problems. Based on this formalism, an advanced method for coil-sensitivity estimations is introduced, which has been incorporated in all later reconstruction strategies. The most important principles of the data simulation framework, implemented for evaluation of the later algorithms, are presented in Chapter 4.

---

[1] An artifact is defined as a false feature in the image. It is created by imperfections in the data collection or reconstruction [3].

Chapters 5 to 7 introduce, evaluate, and extend the proposed model-based nonlinear inverse reconstruction method for T_2 parameter mapping from undersampled Cartesian data. While most of the methods are based on the clinically assumed mono-exponential model, Chapter 8 demonstrates the incorporation of a recent advanced signal model, based on a generating function approach.

2

Magnetic resonance imaging

This chapter gives a brief overview of the principles of Nuclear Magnetic Resonance (NMR) and Magnetic Resonance Imaging (MRI). The introduction of imaging principles focuses on spin-echo data acquisitions, which are the basis for the T_2 reconstruction approaches in the later sections. For comprehensive information about MRI, its various sequences and applications, the reader is referred to the textbooks by Haacke et al. [3], Liang et al. [4] and Bernstein et al. [5].

2.1 Nuclear spins and magnetization

NMR was discovered in 1945 by Bloch and Purcell [6, 7]. Their work was honored with the Nobel Prize in physics in 1952. Since then, the technique has evolved to one of the leading tools in diagnostic imaging.

In principle, the NMR effect can be observed in all atoms with nonzero spin quantum number I. In analogy to the total angular momentum of the electron shell, the spin quantum number is composed by the vectorial sum of the individual nucleon spins and their orbital angular moments. The spin is directly associated with a magnetic moment

$$\mu = \gamma I \tag{2.1}$$

where the gyromagnetic ratio γ is a nucleus-dependent property. Placed in an external magnetic field B_0, the Zeemann splitting phenomenon describes different discrete energy states that are given by

$$E_m = -m\gamma\hbar B_0, \tag{2.2}$$

where $\hbar$ is the Planck's constant divided by 2π. The $2I+1$ possible values $m = -I, -I+1, ..., I$ are sometimes called *magnetic quantum numbers* because of their role in magnetic field experiments like that of Stern and Gerlach [8].

Because of their dominant occurrence in all living tissue, the most important nucleus for MRI is the proton in hydrogen (^1H). Its spin quantum number of $I = 1/2$ leads to two possible energy states with magnitude values proportional to the external magnetic field:

$$E_\uparrow = -\gamma\frac{\hbar}{2}B_0 \qquad\qquad E_\downarrow = \gamma\frac{\hbar}{2}B_0. \tag{2.3}$$

The states correspond to a parallel (↑) or anti-parallel (↓) alignment of the magnetic moments μ with the external magnetic field B_0. The energy difference between both states is given by

$$\Delta E = \hbar\gamma B_0. \tag{2.4}$$

According to the Boltzmann relationship, the spin population difference in the two states yields:

$$\frac{N_\uparrow}{N_\downarrow} = e^{\frac{\Delta E}{k_b T}} \tag{2.5}$$

(k_b = Boltzmann constant, T = thermodynamic temperature),

which results in a slightly higher occurrence of the parallel alignment[1]. The average of all magnetic moments within an macroscopic volume therefore yields a bulk magnetization $\vec{M}$ that points along the external field. Its magnitude is given by [4]:

$$M_0 = |\vec{M}| = \frac{\gamma^2\hbar^2 N_s}{4k_B T}B_0 \tag{2.6}$$

and is directly proportional to the external magnetic field strength as well as to the number of spins N_s within the macroscopic volume. The direction of $\vec{M}$ at equilibrium, i.e. the direction of B_0, is usually defined as the z-direction in NMR and MRI.

While the orientation of μ is quantized along the direction of the external field, this quantization does not apply for the transverse components $\vec{\mu}_{xy}$. In fact, quantum mechanical analysis reveals [3, 10] that the expectation values for the proton magnetic moments are precessing[2] clockwise about the z-axis at a fixed polar angle. The frequency of this precession is given by the Lamor equation:

$$\omega_0 = \gamma B_0 \tag{2.7}$$

and is proportional to the external magnetic field. However, as the phase of the precession remains random, the transverse components cancel out in superimposition. Therefore, in thermal equilibrium, the direction of the bulk magnetization remains statically on the z-axis (Figure 2.1). All imaging principles discussed in the next section base on

---

[1] At body temperature and a field strength of 1T, the number of excess spins is approximately 6 parts per million (ppm) [9].

[2] Precession: the motion of a spinning body, such as a top, gyroscope, or planet, in which it wobbles so that the axis of rotation sweeps out a cone [11].

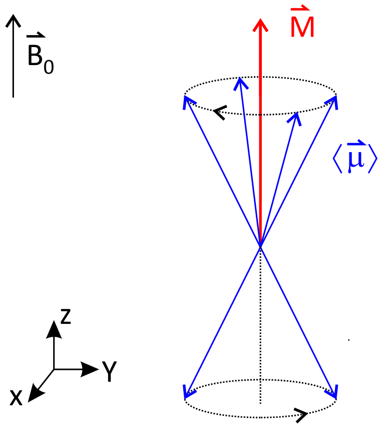

Figure 2.1: *Precession of the proton magnetizations $\vec{\mu}$ in the presence of a constant external field $\vec{B}_0$ pointing in z-direction. Vectorial addition leads to a macroscopic magnetization $\vec{M}$.*

the ability to detect and manipulate this "bulk magnetization" by changing the magnetic environment of the hydrogen protons within observed macroscopic volumes, i.e. the *voxels*.

2.1.1 Excitation and reception

The classical equations of motion[3] state that the application of a magnetic field $\vec{B}_1$ leads to a torque on a magnetic moment $\vec{\mu}$. Assuming no spin interactions, the same applies for the bulk magnetization vector $\vec{M}$:

$$\frac{d\vec{M}}{dt} = \gamma \vec{M} \times \vec{B}_1. \tag{2.8}$$

The orientation of $\vec{M}$ can therefore be influenced by electromagnetic waves that may be sent by a nearby radiofrequency (rf) "transmit" coil. However, according to Equation (2.8) the applied torque is orthogonal to the plane spanned by $\vec{B}_1$ and $\vec{M}$. Due to its alternating nature, the torque of harmonically oscillating B-fields is therefore likely to cancel out over time. However, if the electromagnetic wave is synchronized with the precession frequency and sent perpendicular to z, the resulting torque stays perpendicular to $\vec{M}$. This *resonance condition* enables the possibility to tilt the magnetization away from its longitudinal direction (the z-axis) into the transverse or xy-plane. The procedure is illustrated in Figure 2.2.

As the $\vec{M}$-vector continues precessing, the magnetic field produced by the aggregated proton spins yields a changing flux in a suitable positioned nearby "receiver" coil (Figure 2.3). This is the NMR signal used for detection and quantification of the proton spin-density in MRI. The rf pulse that tips all longitudinal magnetization into

---

[3] In fact, Equation (2.8) can also be derived from a quantum mechanical treatment of the expectation values $\langle\mu\rangle$ under the influence of an external magnetic field. An according derivation is given in [10].

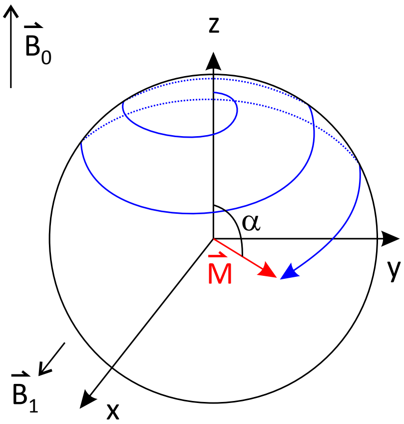

Figure 2.2: *Motion of the macroscopic magnetization $\vec{M}$ under the influence of an excitation field $\vec{B}_1$, oscillating with the Lamor frequency.*

the transverse plane is called a 90°-pulse. Pulses that produce arbitrary *flip angles* are often referred to as α-pulses. In general, the flip angle is proportional to the integral over the envelope $B_1(t)$ of the applied rf pulse [4]:

$$\alpha = \gamma \int_0^{T_{\mathrm{rf}}} B_1(t) dt, \tag{2.9}$$

with T_{rf} the rf-pulse duration.

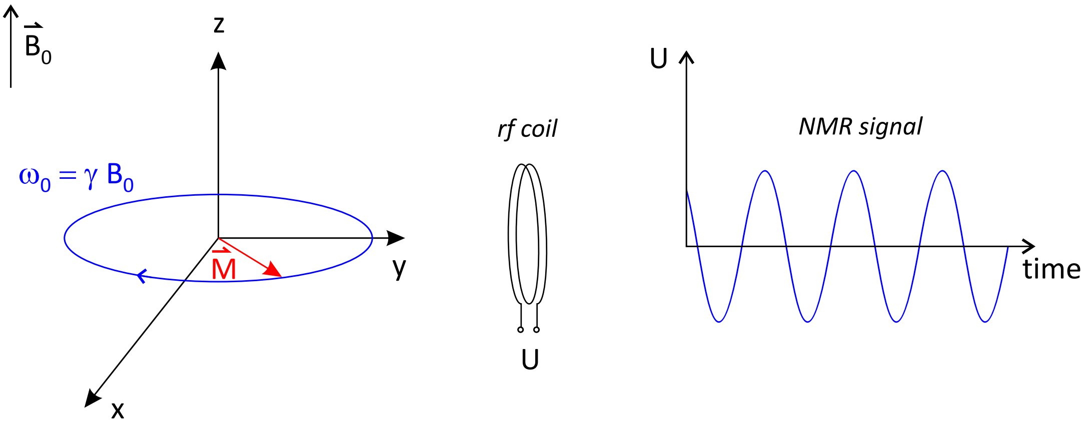

Figure 2.3: *Precession of an excited magnetization vector $\vec{M}$ in the transverse plane. The changing magnetic field induces a voltage U in a nearby receiver coil. The voltage oscillates with the Lamor frequency ω_0.*

2.1.2 Relaxation and Bloch equations

After deactivation of the B_1 field, the spins within an excited region return to their thermal equilibrium state. This *relaxation* process follows an exponential relation:

$$M_z(t) = M_z(0) \cdot (1 - e^{-t/T_1}), \tag{2.10}$$

where the time constant T_1 is often referred to as *spin-lattice* or *longitudinal relaxation* time. The value of T_1 depends on the probability of energy exchanges between the protons with their environment and is therefore a material- or tissue-specific parameter.

In practice, the receivable signal after 90° excitation has usually vanished long before the z-magnetization has fully recovered. This signal loss can be explained by proton interactions that cause the individual spin precession frequencies to fluctuate within a macroscopic volume. The effect causes the spins to dephase until no net magnetization can be measured anymore. The dephasing also follows an exponential relation, characterized by a time constant T_2:

$$M_{xy}(t) = M_{xy}(0) \cdot e^{-t/T_2}. \tag{2.11}$$

According to its nature, T_2 is often called the *spin-spin* or *transverse relaxation* time. A convenient way to illustrate phase relations of spins is the use of a coordinate system that rotates with ω_0 about its vertical axis. According *rotating frame* plots for the T_2 effect are depicted in Figure 2.4.

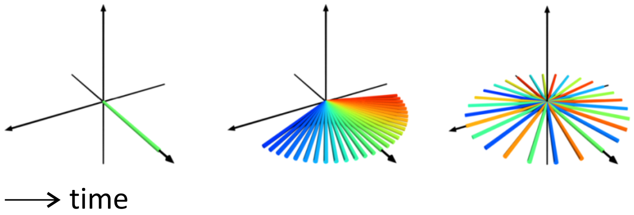

Figure 2.4: *Dephasing of excited proton spins in a rotating frame. Initially, all spins are in phase and superimpose to a single magnetization (left). After some time, the spins have lost coherence such that their magnetic components cancel out from macroscopic view (right).*[4]

In practice, T_1 and T_2 relaxation occur simultaneously. To account for these effects, Bloch extended Equation (2.8) by respective relaxation terms, yielding the *Bloch equations*:

$$\frac{d\vec{M}}{dt} = \vec{M} \times \gamma\vec{B} + \begin{pmatrix} -M_x/T_2 \\ -M_y/T_2 \\ (M_0 - M_z)/T_1 \end{pmatrix}, \tag{2.12}$$

introduced in 1946 [6]. Additional diffusion terms have been later elaborated in [12], but are neglected here for simplicity. Because of their dependence on the individual sample material, T_1 and T_2 offer a powerful tool to distinguish human tissues in clinical MRI.

2.1.3 Free induction decay and spin echo

In addition to the T_2 effects, inevitable local field-inhomogeneities contribute to the dephasing of the spins. The *free induction decay*, measurable after a 90°-pulse, is

---

[4] POV-ray code for the spin plots by courtesy of Dr. Oliver Natt.

therefore characterized by an *effective spin-spin relaxation time* T_2^* with

$$\frac{1}{T_2^*} = \frac{1}{T_2} + \frac{\gamma \Delta H}{2}. \tag{2.13}$$

Here, ΔH describes both the static field inhomogeneity and the effect of the magnetic field gradients [10]. However, while the T_2 effects can be considered to be irreversible, the accumulated spin phase due to ΔH can be revoked with the application of a 180°-pulse. As the pulse inverts the transversal magnetization, a *spin echo* is formed after an echo time TE (Figure 2.5). The effect was first described in 1950 by Hahn [13, 14].

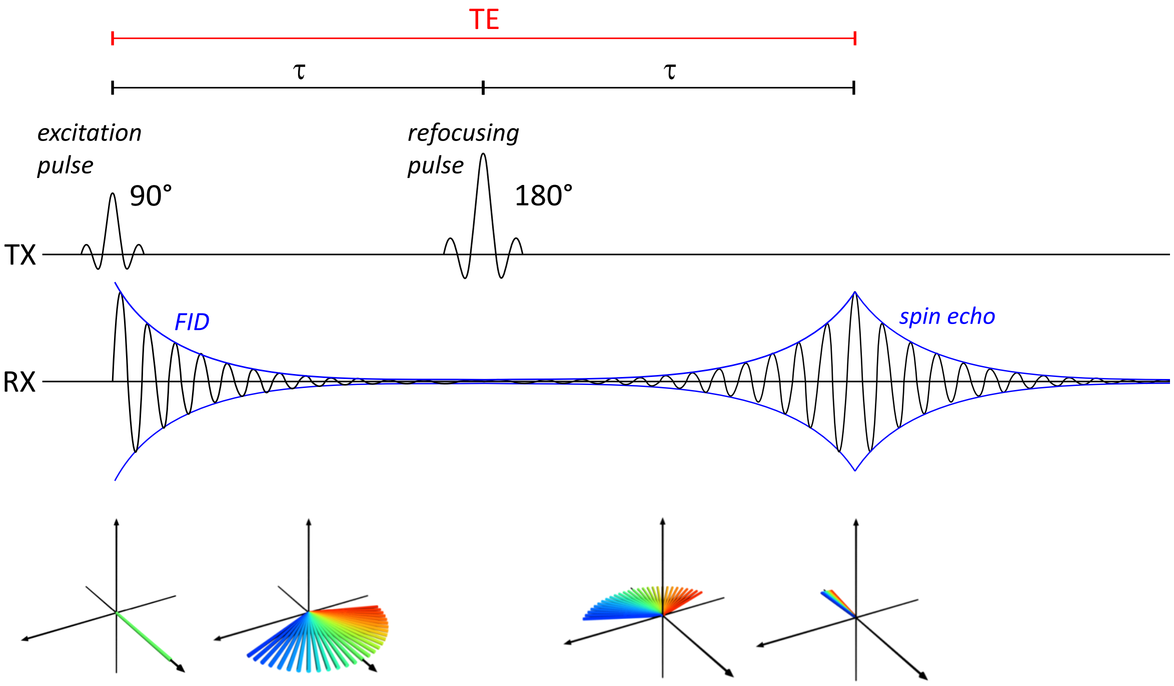

Figure 2.5: *Formation of a spin echo: The application of a 180° pulse causes the previously dephased spins to regain phase coherence at an echo time* TE $= 2\tau$*. TX and RX refer to rf transmission and reception.*

2.1.4 Stimulated echoes

The application of more than two subsequent rf pulses gives rise to a phenomenon known as *stimulated echoes* [13]. A graphical illustration of the formation of these echoes is given in [15]. The effect can yield an undesired perturbation of spin-echo based signal acquisitions (see also Chapter 8). However, when systematically provoked, the formation of stimulated echoes can also be exploited for spectroscopy and fast imaging methods as the STEAM (stimulated echo acquisition mode) sequence introduced in 1985 by Frahm et al. [16, 17].

2.2 Spatial encoding

The methods described in the previous section allow for the detection of a radio signal with an initial amplitude that is proportional to the density of all excited proton spins within the reception range of the rf coil. To calculate two- or three-dimensional images from the signal, it is necessary to distinguish spins from different spatial locations. The fundamental solution to this problem has been published in 1973 by LAUTERBUR [1] who was awarded the Nobel Prize in 2003. Today, his originally proposed technique is referred to as *radial sampling* or *radial encoding*. However, due to strong inaccuracies of the early MRI systems, the technique was soon replaced by more robust *Cartesian sampling* schemes [18]. The basics of Cartesian sampling as well as the involved hardware requirements are subject to the next section.

2.2.1 Magnetic field gradients

As previously introduced, the frequency of the receivable NMR signal is given by the Lamor equation (2.7) and is proportional to the external magnetic environment, i.e. the magnetic field B_0. If B_0 is homogeneous throughout the sample, all involved proton spins have the same resonance frequency. Excitation of this configuration yields a NMR signal with the same single frequency and an amplitude proportional to the overall number of excited spins (assuming no chemical shift). In order to distinguish different regions, the magnetic environment of the sample has to be systematically manipulated during the acquisition procedure. In MRI, this is done by additional *gradient coils* that are placed within the main magnetic field (Figure 2.6). These coils allow to alternate

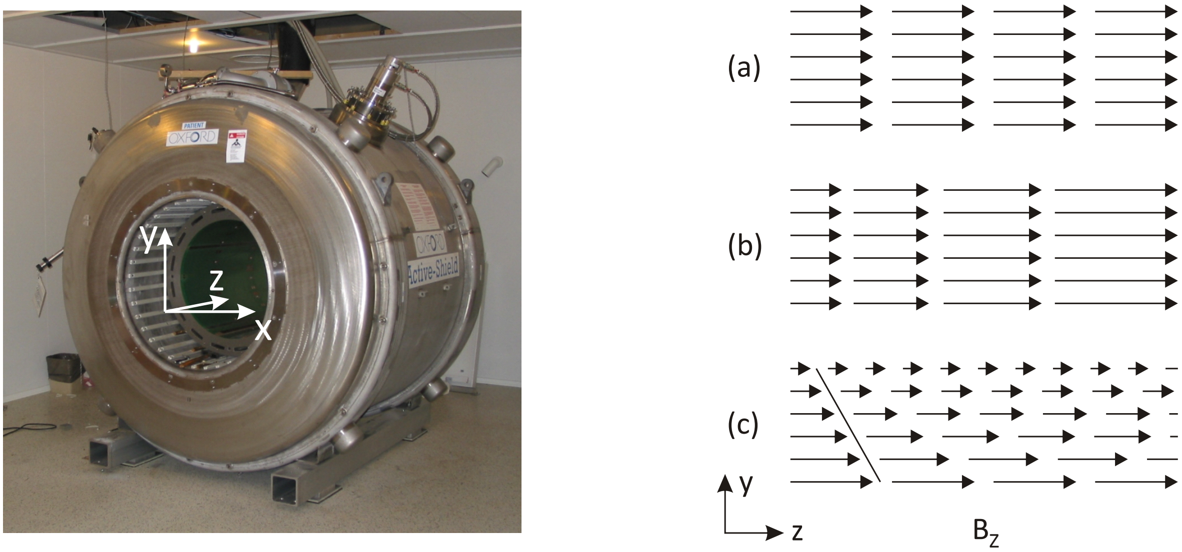

Figure 2.6: *(Left) MRI magnet with gradient inlay. (Right) Idealized magnetic field vectors within the bore: (a) No gradient activated, (b) z-gradient activated, (c) y-gradient activated. Only the z-component is affected by the gradients, while the xy-components ideally remain zero.*

the main field's z-component in any of the three spatial directions. The amplitudes of the gradient fields (measured in mT/m) are often abbreviated with G_x, G_y and G_z, respectively. Consequently, by superimposition, the overall magnetic field gets a spatial dependency:

$$B_z(x, y, z) = B_0 + G_x \cdot x + G_y \cdot y + G_z \cdot z. \tag{2.14}$$

2.2.2 Slice selection

According to the Lamor equation (2.7), an alternation of the magnetic environment of a proton spin ensemble is directly equivalent to an alternation of its precession frequency. Likewise, if the magnetic environment states a linear gradient, the resonance condition of the ensemble changes from a distinct frequency to a continuous range, i.e. a *bandwidth* $\Delta\omega$. Consequently, an excitation pulse with a limited bandwidth of $\Delta\omega_p < \Delta\omega$ will only excite spins within the matching frequency range. The combination of magnetic field gradients with limited bandwidth excitation pulses is called *slice selection* and is illustrated in Figure 2.7. The technique renders the possibility to excite only selected slices within the sample while leaving the surrounding spins in equilibrium state. The profile and the position of the slices can be controlled by the pulse bandwidth, which is usually aimed to be a rectangular function of width Δz:

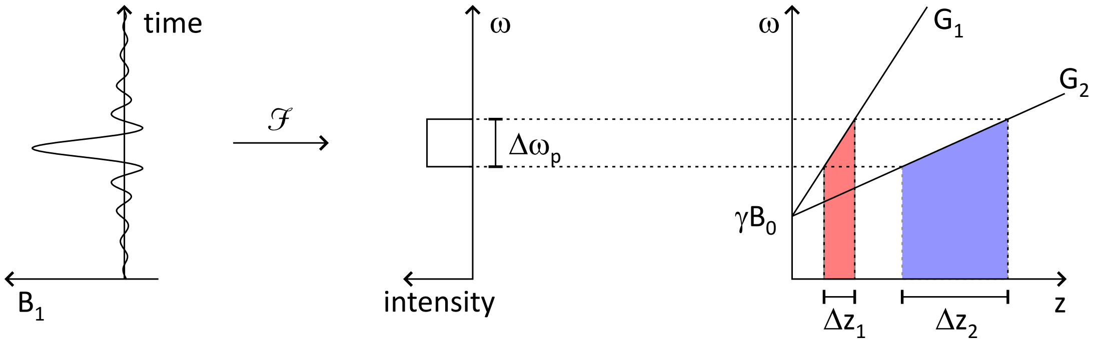

Figure 2.7: *Different gradient strengths (G_1 and G_2) mapping the same pulse with* sinc*-shaped envelope $B_1(t)$ to slices of different thickness at different positions (Δz_1 and Δz_2). $\mathcal{F}$ refers to the Fourier transform.*

$$\Delta\omega_p = \omega_p(z) = \mathrm{rect}(\frac{z - z_0}{\Delta z}), \text{ with} \tag{2.15}$$

$$\mathrm{rect}(z) = \begin{cases} 0 & \text{for} |z| > \frac{1}{2} \\ \frac{1}{2} & \text{for} |z| = \frac{1}{2} \\ 1 & \text{for} |z| < \frac{1}{2}. \end{cases} \tag{2.16}$$

However, due to the Fourier transform relationship, the envelope of the required waveform for this slice profile would be a *Sinus Cardinalis* or sinc function:

$$\begin{aligned} \mathcal{F}[\mathrm{rect}(z)](k) &= \int \mathrm{rect}(z) \cdot e^{-2\pi i k z} dz \\ &= \frac{\sin(\pi k)}{\pi k} \\ &= \mathrm{sinc}(\pi k) \end{aligned} \tag{2.17}$$

which, unfortunately, has an unlimited support. Because in practice only excitation pulses with finite length are feasible, most actual pulse waveforms are composed by a truncated version with additional filtering. This approach causes the slice profile to deviate from its ideal form. The choice of the filter thereby yields a trade-off between a broadened flip-angle distribution within the slice, or the excitation of regions outside the slice due to side lobes of the imperfect profile.

2.2.3 Fourier encoding

The slice-selection technique reduces the spin localization problem from three to two dimensions. The spatial separation of spin density within a slice is usually achieved with a technique called *Fourier encoding.* For Cartesian sampling, the necessary encoding intervals can be divided into so-called phase- and frequency-encoding steps. Both methods are briefly described in the following.

Frequency encoding

After excitation, the nuclear spins within a selected slice precess in phase with uniform Lamor frequency. The resulting NMR signal can be expressed in the complex plane with

$$s(t) = M \cdot e^{-i\omega_0 t}. \tag{2.18}$$

The spectrum of this signal would ideally exhibit a single peak at ω_0 (neglecting chemical shifts and relaxation effects). However, again the Lamor frequency can be spatially altered by the use of gradients. For example, if the selected slice lies in the xy-plane, a gradient G_x, activated during the sampling interval, yields a linear relation between the Lamor frequency and the spatial spin location in x-direction. The voltage U induced in a nearby rf-coil respectively represents the real part of the integral over all frequency components:

$$U(t) = \Re \int M(x) \cdot e^{-i(\omega_0 + \omega_x(x))t} dx, \tag{2.19}$$

with $\omega_x(x) = \gamma \cdot G_x \cdot x$. By so-called *quadrature detection* the carrier signal $e^{-i\omega_0 t}$ can be removed and the real and imaginary parts of the remaining expression can be determined. The procedure yields the demodulated complex signal:

$$s(t) = \int M(x) \cdot e^{-i\omega_x(x)t} dx. \tag{2.20}$$

The spectrum of this signal represents a one-dimensional projection of the in-plane spin density onto the x-axis. As this method encodes spatial locations in the frequency of the received signal, it is often referred to as *frequency encoding*.

Phase encoding

A single measurement of a frequency-encoded slice only yields one-dimensional information about the object. The encoding of two-dimensional images is usually performed by a combination of frequency encoding with a *phase-encoding* strategy:

Similar to frequency encoding, phase encoding employs a linear gradient, say G_y, enabled after the excitation pulse. However, instead of applying the gradient during signal acquisition, this gradient is only activated during a defined preparatory period T_{pe}. After the gradient is switched off, the magnetization within the slice returns to precess with a uniform Lamor frequency. However, the spin components now bear an initial phase angle

$$\varphi(y) = \gamma \cdot y \int\limits_0^{T_{pe}} G_y(\tau) d\tau \tag{2.21}$$

which is linearly related to their location in y-direction.

k-space

The combined application of both frequency and phase encoding strategies is often simplified in a *k-space* formalism, where the *k-space trajectory* is defined by

$$\vec{k}(t) := \frac{\gamma}{2\pi} \int\limits_0^{t} \vec{G}(\tau) d\tau. \tag{2.22}$$

The variables $\vec{k}$ and $\vec{G}$ are hereby vectors in three-dimensional Cartesian space:

$$\vec{k} = \begin{pmatrix} k_x \\ k_y \\ k_z \end{pmatrix}, \qquad \vec{G} = \begin{pmatrix} G_x \\ G_y \\ G_z \end{pmatrix}. \tag{2.23}$$

For two-dimensional encoding, the signal at different k-space positions is related to the spatial distribution of magnetization vectors $M(x, y)$ by:

$$s(k_x, k_y) = \int \int M(x, y) \cdot e^{-i2\pi(k_x x + k_y y)} dx dy \tag{2.24}$$

$$= \mathcal{F}_{xy} \left[M(x, y) \right], \tag{2.25}$$

where $\mathcal{F}_{xy}$ is the two-dimensional Fourier transform.

2.2.4 Sampling of k-space

In practice, the encoding and processing of infinite continuous data is infeasible. Instead, the k-space signal has to be cut off and is usually sampled at a finite number of discrete data positions. The maximal distance of the samples $\Delta\vec{k}$ is hereby limited by the Nyquist-Shannon theorem [19] and the desired *field of view* (FOV). Assuming the FOV to be a rectangle of width W_x and W_y (Figure 2.8, left), the sampling theorem requires:

$$\Delta k_x \leq \frac{1}{W_x}, \qquad \Delta k_y \leq \frac{1}{W_y}. \tag{2.26}$$

In conventional imaging, the k-space is sampled in a line-by-line scheme (Figure 2.8, right), where frequency encoding is used along the x-direction and phase encoding is used along the y-direction. The resulting signal samples $s[n_x, n_y]$ can be described by:

$$s[n_x, n_y] = s(n_x\Delta k_x, n_y\Delta k_y) \tag{2.27}$$

$$= \int_{-\infty}^{\infty}\int_{-\infty}^{\infty} M(x,y)e^{-i2\pi(n_x\Delta k_x x + n_y\Delta k_y y)}dxdy. \tag{2.28}$$

After a sufficient amount of data is sampled, an approximation of the spin-density distribution can be reconstructed from the data by two-dimensional (inverse) discrete Fourier transform (DFT):

$$M[x,y] = \frac{1}{\sqrt{N_x\ N_y}}\sum_{n_y=0}^{N_y-1}\sum_{n_x=0}^{N_x-1} s[n_x,n_y]e^{i\ 2\pi\left(\frac{n_x\ x}{N_x}+\frac{n_y\ y}{N_y}\right)}. \tag{2.29}$$

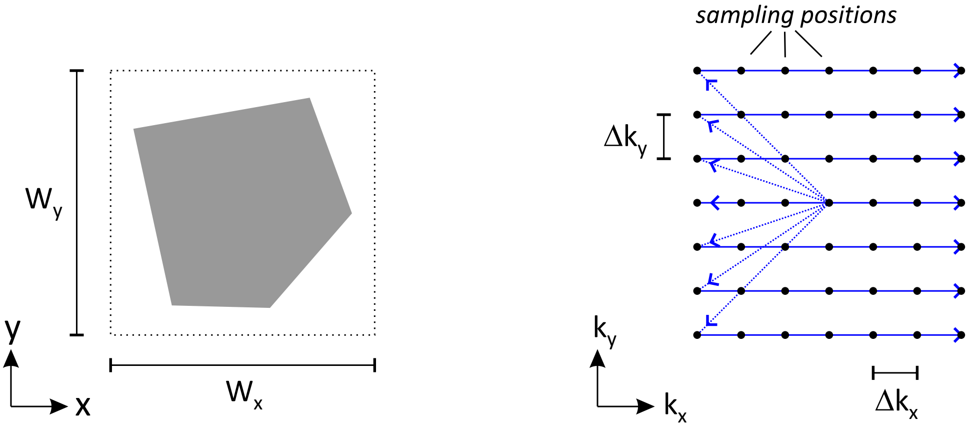

Figure 2.8: *(Left) Illustration of an object bounded by a rectangular field of view (FOV) of width W_x and W_y. The k-space signal of the object is equidistantly sampled on a Cartesian grid (right). The example refers to 7 readout lines, frequency encoded in x-direction. Every line bears an unique phase encoding, applied in y-direction prior to sampling.*

2.2.5 Non-Cartesian trajectories

As has been mentioned before, the most widespread sampling schemes in todays clinical routine are based on Cartesian trajectories. One advantage of this method is the relatively simple image reconstruction by efficient algorithms like the (inverse) fast Fourier transform (FFT). More importantly, the effects of image distortions due to linear gradient imperfections are often negligible. However, with the continuously improved hardware of modern MRI systems, some of these limitations have been resolved [20]. With state-of-the art systems and depending on the application, alternative sampling schemes such as spiral [21], rosette [22], or stochastic [23] trajectories may offer advantages over Cartesian schemes. Especially the radial trajectories, as originally proposed by Lauterbur [1], have been found to be less sensitive to motion [24] and are currently experiencing a renaissance in real-time applications [25, 26].

Considering arbitrary k-space trajectories, the generalized NMR signal equation yields:

$$s(t) = \int M(\vec{r}) \cdot e^{-2\pi i \cdot \vec{r} \cdot \vec{k}(t)} d\vec{r}, \tag{2.30}$$

with $\vec{k}(t)$ the k-space trajectory and $\vec{r}$ a spatial coordinate in image space.

2.3 Array coils

Signal excitation and reception in MRI is performed by rf coils. The sensitivity of these coils has a spatial dependency which can become very important for advanced image reconstruction strategies. The aspect will be revisited in Section 3.1.1. A comprehensive electromagnetic analysis of coil designs in MRI is given in [27]. In general, the coil sensitivity profile is subject to several design properties. For example: Large *volume coils* usually offer a large FOV with a relatively homogeneous profile. These properties are especially advantageous for excitation. However, a large FOV may also involve a comparably high amount of noise in signal reception. Especially for small object sizes, the signal-to-noise ratio (SNR) can therefore significantly be improved with the use of smaller *surface coils* mounted close to the object under observation.

To combine the advantage of both design strategies, modern MRI systems utilize so-called *array coils* consisting of multiple small coils which are electromagnetically decoupled as far as possible. Every coil element requires a separate pre-amplifier and analog-to-digital converter (ADC) channel. The (demodulated) NMR signal obtained by such a multiple receiver coil is given by

$$s_c(t) = \int M(\vec{r}) C_c(\vec{r}) e^{-2\pi i \vec{k}(t) \vec{r}} d\vec{r} + n(t). \tag{2.31}$$

Here the C_c denote the complex-valued spatial sensitivity profiles of every channel c, M and $\vec{k}$ are the magnetization and the chosen k-space trajectory. The signal s_c is further disturbed by noise $n(t)$.

Given a vector $\mathbf{s}_c$ of fully sampled k-spaces from such array coils, reconstruction of individual images $\hat{\mathbf{S}}_c$ for every coil element is possible by inverse discrete Fourier transform (iDFT):

$$\hat{\mathbf{S}}_c = \mathrm{iDFT}\left(\mathbf{s}_c\right). \tag{2.32}$$

Assuming independent and identically distributed Gaussian white noise, the best unbiased estimate of the magnetization can be derived from the individual images by

$$\mathbf{M}_{\text{est}} = \frac{1}{\sum_c |\mathbf{C}_c|^2} \sum_c \bar{\mathbf{C}}_c \cdot \hat{\mathbf{S}}_c \tag{2.33}$$

with $(\cdot)$ denoting point-wise vector multiplication and $\bar{\mathbf{C}}_c$ being the complex conjugate coil-sensitivity profiles [28, 29, 30]. Because Equation (2.33) requires knowledge of the profiles $\mathbf{C}_c$ (see Section 3.1.3), a combined image is often calculated from the root of sum of squares (RSS) instead:

$$\mathbf{M}_{\text{rss}} = \sqrt{\sum_c |\hat{\mathbf{S}}_c|^2}. \tag{2.34}$$

The procedure is illustrated in Figure 2.9 for a four-channel head coil.

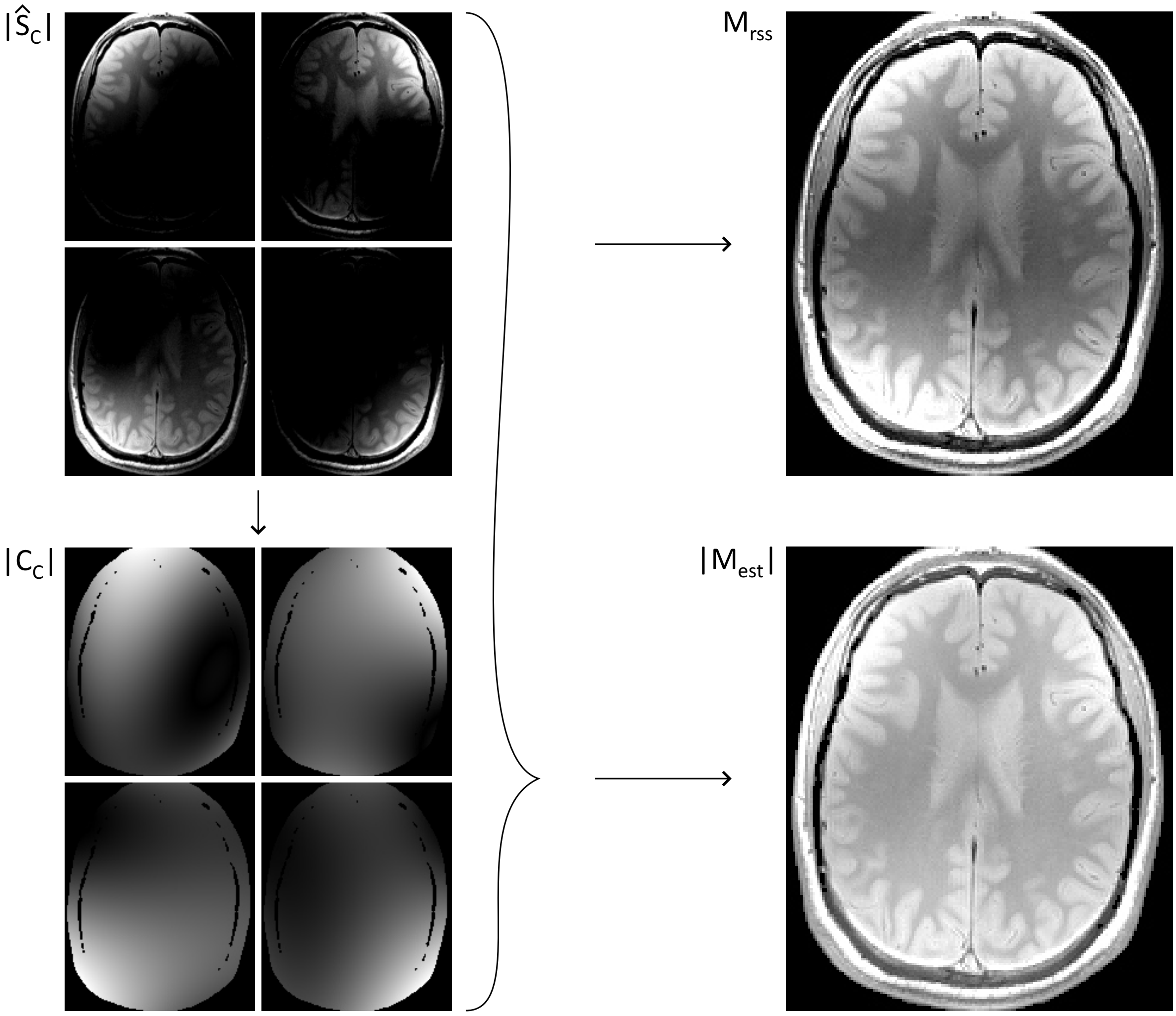

Figure 2.9: *($|\hat{\mathbf{S}}_c|$) Individual magnitude images of a four-channel array coil. ($\mathbf{M}_{\text{rss}}$) RSS combination of the four channels, ($|\mathbf{C}_c|$) magnitude representation of coil-sensitivity estimates, ($|\mathbf{M}_{\text{est}}|$) magnitude image estimate considering the coil sensitivities in ($|\mathbf{C}_c|$).*

2.4 Imaging sequence and measurement time

Figure 2.10 shows the complete timing diagram of the classical spin-echo sequence and demonstrates the acquisition of a Cartesian k-space dataset using magnetic field gradients for slice, phase, and frequency encoding. To collect a full k-space, the illustrated experiment has to be repeated Np times. The time between each repetition is the *repetition time* (TR) and allows the excited spins to return to the equilibrium state prior to subsequent excitations. As TR is usually much longer than the *echo time* (TE), the overall scan time is mainly determined by the product of Np and TR. The choice of these values strongly depends on the particular application. As a compromise between practicability and reduction of T_1-weighting effects, repetition times of 2 to 6 seconds are common at a field strength of 3T. Using a standard number of 256 phase-encoding steps, this requires scan times between 8 and 25 minutes.

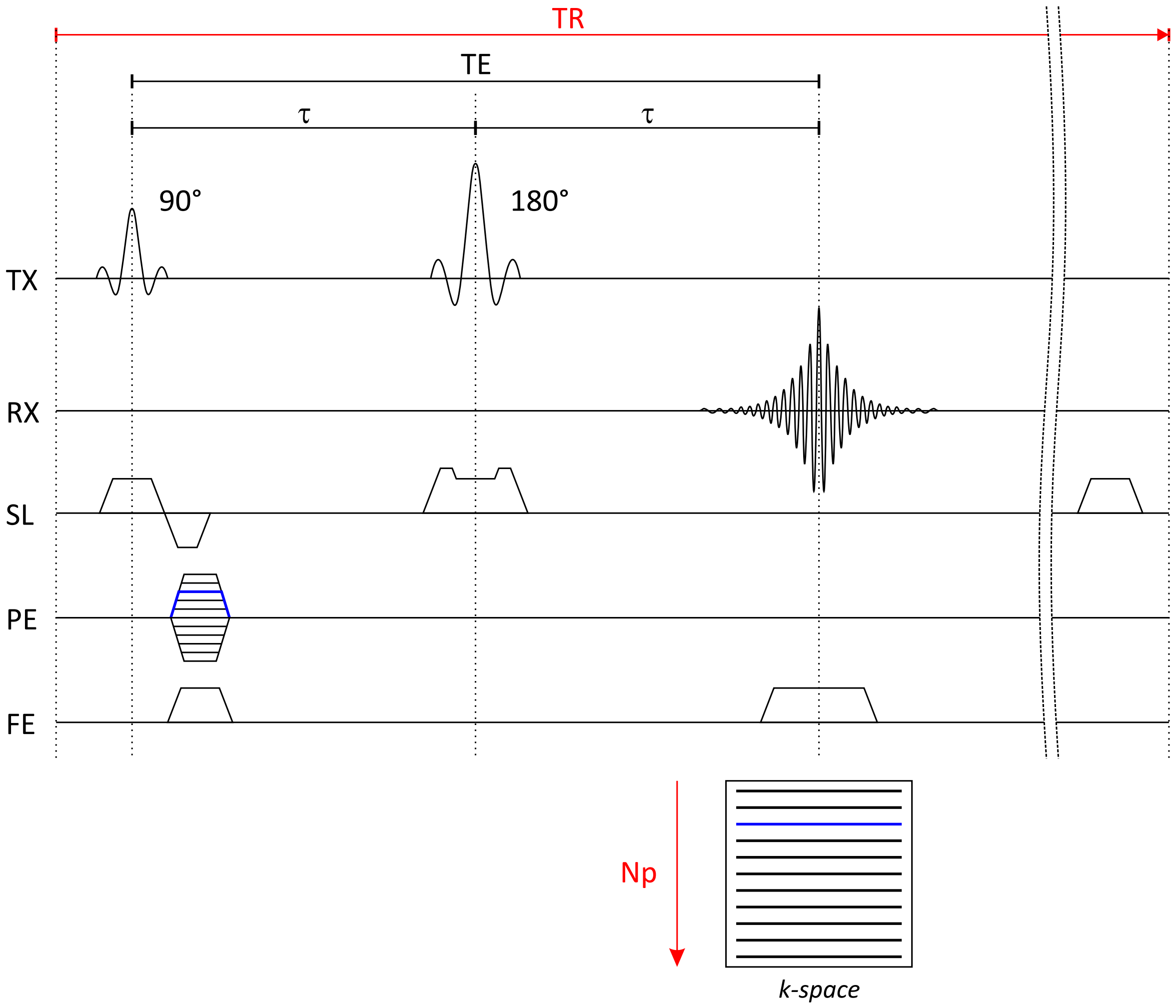

Figure 2.10: *Timing diagram of the classical spin-echo sequence. TX and RX refer to rf transmission and reception. SL, PE, and FE denote the slice, phase, and frequency-encoding gradients. The echo time (TE) is given by 2τ with τ the period between the excitation (90°) and refocusing pulse (180°). Overall scan time is determined by the number of phase-encoding steps (Np) and the repetition time (TR).*

2.5 Contrast mechanisms and T_2 relaxometry

The pixels of an MR image usually represent the relative signal strength of proton spins at different locations translated into gray values. As introduced in Section 2.1.2, the signal decay in MRI is subject to different relaxation effects. As these effects vary significantly between different materials, images acquired at different stages of the relaxation exhibit different contrast between the materials [31]. In 1971, observations by DAMADIAN et al. revealed that the relaxation times in cancerous tissues are altered relative to those of normal tissues [32]. Since then numerous workers studied the dependence of those parameters on tissue type and pathology [33] and several methods have been developed to acquire images at which either of the two relaxation mechanisms is emphasized. The resulting images are said to be T_1-*weighted* or T_2-*weighted*, respectively. The following paragraph introduces a technique for the generation of T_2-weighted images which will be used for all model-based reconstructions in Chapters 5 to 8.

2.5.1 T_2 weighting

The spin-echo sequence (Figure 2.10) is based on the acquisition of spin echoes occurring after the subsequent application of a 90° and a 180° rf pulse, separated by the time interval τ. While the 180° pulse inverts the dephasing effect of field inhomogeneities, it does not compensate for the dephasing due to proton interactions. The signal intensity is consequently subject to the T_2 decay which evolves during the echo time $\mathrm{TE} = 2\tau$. The length of TE can therefore be used to regulate the T_2 weighting of images and is controllable with the interval τ between the two rf pulses. Figure 2.11 shows images of the same anatomical region acquired at different echo times.

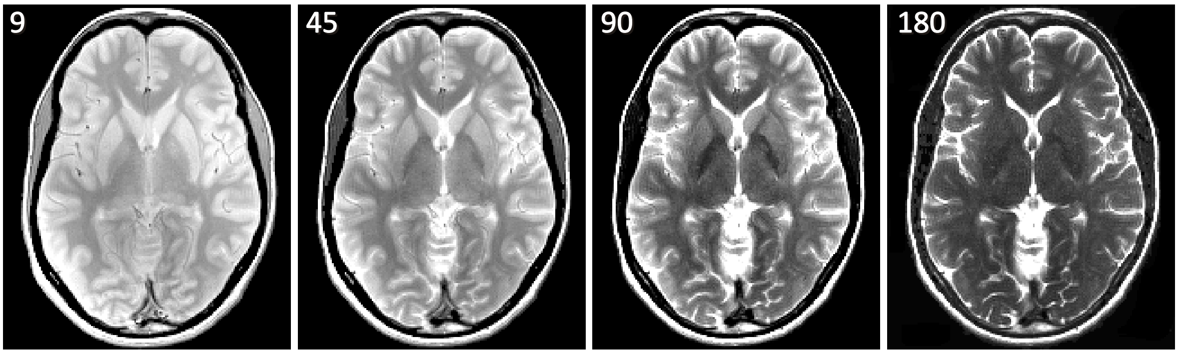

Figure 2.11: *Spin-echo MRI of the human brain at echo times of 9, 45, 90, and 180 ms. The TE values correspond to spin-density contrast, as well as low, moderate, and strong* T_2 *weighting.*

2.5.2 T_2 relaxometry

The acquisition of multiple and differently T_2-weighted images can render the possibility to reconstruct the actual values of T_2 in different image regions. The resulting quantitative parameter maps allow for an unambiguous discrimination of different tissues and offer retrospective calculation of arbitrarily T_2-weighted images. Unfortunately, the diagnostic advantages of parameter maps usually come at the expense of long scan times. However, specifically with respect to T_2 relaxometry, several new methods have been developed and evaluated during this thesis to overcome these limitations.

3

Image reconstruction

Mathematically, traditional MRI reconstruction strategies can be formulated as linear inverse problems, which may be solved by different numerical methods. The formalism as well as the concept of iterative optimization are introduced in the following section and will be used throughout all later reconstruction algorithms in Chapters 5 to 8. The transition to nonlinear inverse problems is demonstrated in Section 3.2 on the basis of a novel parallel imaging approach. The technique will be exploited for the estimation of coil sensitivities in Sections 5.2.2, 7.2.5 and 8.1.2.

3.1 Image reconstruction as a linear inverse problem

According to Equation 2.30 the k-space from an idealized single receiver coil is given by the Fourier transform of a magnetization or spin-density distribution sampled on a chosen k-space trajectory. The relation can be understood as the *forward problem* of MR image reconstruction:

$$y(\vec{k}) = P_k \; \mathcal{F} \; x(\vec{r}), \tag{3.1}$$

where x is the unknown image, y the measured data, $\mathcal{F}$ the Fourier transform and P_k the trajectory defined by the restriction onto the measured k-space positions. Apparently, the reconstruction of x corresponds to the *inverse problem*.

In practice, the k-space trajectory is only sampled on a discrete lattice of time points, so that y is typically only known on a finite area around the origin of a Cartesian grid.

Accordingly, the solution x is not unique, as it yields the original spin-density distribution perturbed with arbitrary combinations of spatial frequencies corresponding to the non-sampled positions in k-space. However, assuming these components to be small, a good spin-density approximation can usually be achieved by choosing the solution with minimal energy or l^2 norm, i.e. by simply assuming all non-sampled k-space points to be zero.

For discrete Cartesian sampling, the image x and the signal y in Equation (3.1) can be replaced by a vector of signal samples $\mathbf{y}$ and a vector of image pixels $\mathbf{x}$. The continuous Fourier transform $\mathcal{F}$ then reduces to a matrix of Fourier coefficients $\mathbf{F}$ from a 2D DFT. Also, for Cartesian sampling, P_k can be reduced to a diagonal matrix $\mathbf{P}$ holding the coefficients of a binary sampling mask. Combination of the linear operations into a single *system-matrix*

$$\mathbf{A} = \mathbf{PF} \tag{3.2}$$

yields the linear system of equations

$$\mathbf{y} = \mathbf{Ax}. \tag{3.3}$$

For fully sampled k-space, the matrix $\mathbf{A}$ is square and has full rank. With that, a unique solution of Equation (3.3) is given by the inverse DFT of the data [34]. However, if the data is undersampled, Equation (3.3) gets underdetermined and has ambiguous solutions. The frequency ambiguity in k-space hereby transforms into a spatial ambiguity in image space, which is determined by the *point spread function* (PSF) of the sampling pattern. For example, if only every second k-space line is acquired, the signal intensity of any single object can arbitrarily be distributed over two virtual object copies in image space. Again a unique solution can be found by assuming all non-sampled lines to be zero. The outcome of this approach yields the ”classical” aliasing artifacts, i.e. two equally weighted object copies in image space, as demonstrated for human brain MRI in Figure 3.1 (center). However, without this constraint, a variety of other reconstruction results represent equally valid solutions of Equation (3.3). Some examples are illustrated in Figure 3.2 for simulated two-fold undersampled k-space data from a numerical phantom. Whereas only the very left image is equal to the reconstruction from fully sampled data, all other images represent equally valid solutions of Equation (3.3).

To allow for an acceleration of the data acquisition process, several methods have been established that rely on the ability to exclude undesired aliased solutions from the parameter space by additional constraints. Some of these approaches will be described in the following.

3.1.1 Parallel imaging

If an undersampled MRI signal is acquired from multiple receiver coils, it is possible to compensate for the missing k-space data by exploiting additional spatial information

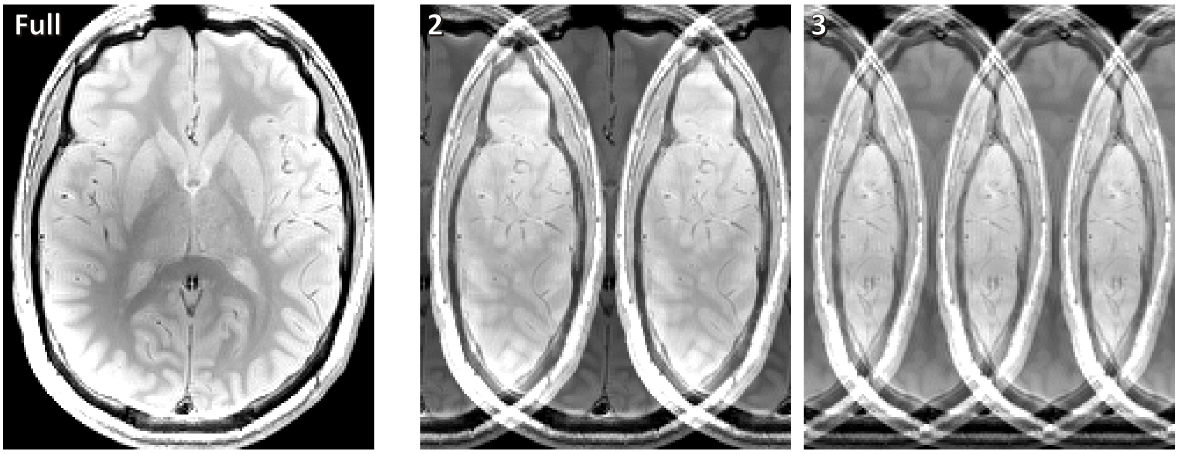

Figure 3.1: *Aliasing artifacts in human brain MRI. (Left) Inverse DFT reconstruction from a fully sampled k-space, (center) and (right) reconstructions from two- and three-fold undersampled k-space. All non-sampled positions in the data vector $\mathbf{y}$ have been set to zero prior the inverse DFT.*

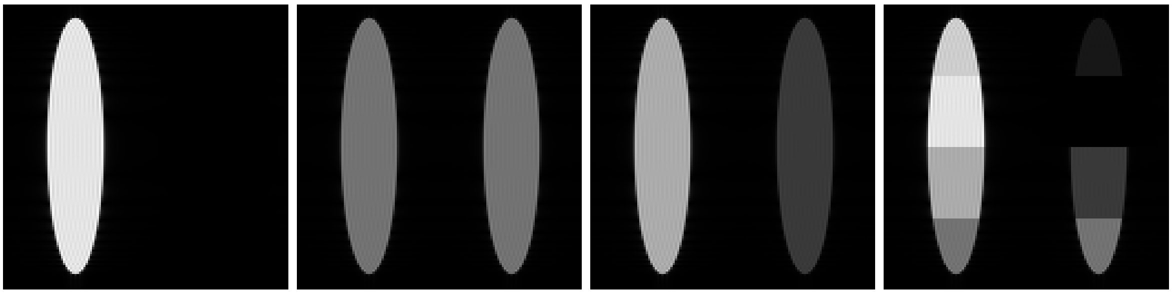

Figure 3.2: *A selection of possible solutions $\mathbf{x}$ for solving Equation (3.3) for two times undersampled k-space data from a numerical phantom. Only the first image is identical to the result from fully sampled data.*

from the coil sensitivity profiles. The concept is known as *parallel imaging* (PI) and allows for the reconstruction of aliasing-free images from a fraction of the data required for conventional MRI. Related methods are usually categorized to be either posed in image space or in k-space. While the general methodology was already published in the late 1980s [35, 36, 37] the first clinical applications were established in 1999 as the SENSE (sensitivity encoding) [38] and the SMASH (simultaneous acquisition of spatial harmonics) [39] algorithm, respectively. Since then, both methods have further been improved to utilize the data of undersampled k-space even more efficiently [40, 41, 42]. A comparison of different approaches is given in [43, 44].

SENSE

If known prior to reconstruction, the system matrix 3.2 can be extended by a matrix $\mathbf{C}$ containing the sensitivity-weighting coefficients from all available receiver coils:

$$\mathbf{A} = \mathbf{PFC}. \tag{3.4}$$

Apparently, with more than one coil element, the number of rows in $\mathbf{A}$ now exceeds the number of columns. Hence the system of equations becomes over-determined and a direct inversion of $\mathbf{A}$ is not feasible. However, a good solution in least-squares sense can often be achieved by the MOORE-PENROSE pseudo inverse [45, 46]

$$\hat{\mathbf{x}} = \mathbf{A}^{\dagger}\mathbf{y}, \qquad \mathbf{A}^{\dagger} = (\mathbf{A}^{H}\mathbf{A})^{-1}\mathbf{A}^{H}, \tag{3.5}$$

with $(\cdot)^{H}$ being the adjoint, i.e. the transposed matrix with each entry replaced by its complex conjugate.

If the sensitivities of the individual elements contribute a sufficient amount of linearly independent row vectors in $\mathbf{A}$, the additional information can be exploited for undersampling. This is the basic strategy behind SENSE [38]. With ideal coil configuration, the method allows for data reduction or acceleration factors (AF) up to the number of coil elements. In practice, however, the achievable acceleration is usually much smaller due to linear dependencies of the profiles or bad conditioning as a consequence of noise. Intuitive introductions of the SENSE algorithm are given in [5]. A tour of parallel imaging strategies from a linear-system perspective is given in [47].

3.1.2 Iterative reconstruction

In practice, the system matrix of MRI reconstruction problems can become very large. For example, storing the Fourier coefficients for the DFT already requires N^2 entries in $\mathbf{A}$. For a single image matrix with a standard size of $N = 256^2$ pixels, this yields more than 10^9 entries for a single receiver coil. A direct calculation of $\mathbf{A}$, $\mathbf{A}^{H}$ and the adjacent inversion can therefore require a high amount of random access memory (RAM). To address possible computational restrictions, it can be beneficial to solve Equation (3.3) iteratively. By avoiding a direct matrix inversion, $\mathbf{A}$ can hereby be replaced by a composition of efficiently implemented subsequent operators. In Equation (3.4), for example, the DFT coefficients $\mathbf{F}$ may be replaced by an FFT implementation, coil-sensitivity weighting and sample masking can be performed by point-wise multiplications. Afterwards, an image estimate $\mathbf{x}$ can iteratively be optimized until its synthesized k-space samples fit best to the measured samples in $\mathbf{y}$. The quality of the estimate is often measured in the least-squares sense by a cost function

$$\Phi(\mathbf{x}) = \frac{1}{2}\|\mathbf{A}\mathbf{x} - \mathbf{y}\|_2^2 \tag{3.6}$$

with the optimal solution

$$\hat{\mathbf{x}} = \underset{\mathbf{x}}{\operatorname{argmin}}\{\Phi(\mathbf{x})\}. \tag{3.7}$$

Several numerical algorithms are available to efficiently minimize Equation (3.6) with respect to the vector of unknowns $\mathbf{x}$. A popular choice is the conjugate-gradient (CG) method, introduced in 1952 [48]. This algorithm requires the calculation of the cost function gradient $\nabla\Phi$. For the linear optimization problem in Equation (3.6), the gradient is given by

$$\nabla\Phi(\mathbf{x}) = \mathbf{A}^H\mathbf{A}\mathbf{x} - \mathbf{A}^H\mathbf{y} = \mathbf{A}^H(\mathbf{A}\mathbf{x} - \mathbf{y}), \tag{3.8}$$

which again can be implemented in operator form, if the adjoint operators are available.

3.1.3 Estimation of coil sensitivity profiles

Parallel imaging methods exploit spatially varying coil sensitivity profiles. The solution of Equation (3.7) therefore requires knowledge of the underlying profiles $\mathbf{C}$ (Figure 2.9). Unfortunately, the sensitivities are not only dependent on the coil design, but also on the dielectric properties of the object within the FOV. As these conditions may change between different experiments, the coefficients have to be recalibrated for every patient and setup. Good estimates of $\mathbf{C}$ can be acquired in a preparation scan, where the reconstructed images of the array coil are divided by the image of the whole-body volume coil [37]. However, the inherent additional scan time spoils the original effort of acceleration. Also, patient movements and body fluids may spoil the accuracy of the coil profiles with respect to subsequent scans. To avoid these limitations, most current parallel imaging implementations employ so-called autocalibration methods. Hereby, a small region in the center of k-space is sampled at full Nyquist rate (Figure 3.3) [41, 49]. The lines can subsequently be filtered and inversely Fourier transformed to create low-resolution images for every coil element. Depending on the implementation, coil profiles may subsequently be taken from low-order polynomials, fitted to the individual images [50].

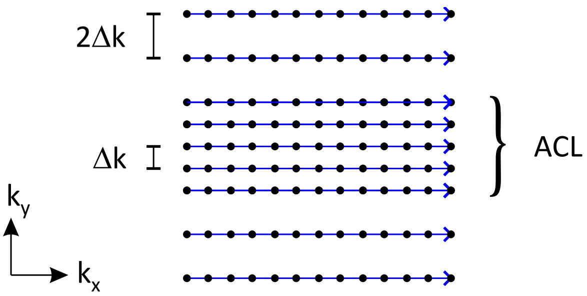

Figure 3.3: *Cartesian k-space sampling with autocalibration lines (ACL). While the higher frequency components are two-fold undersampled in phase direction, the center part is acquired at full Nyquist rate and can respectively be used for inverse DFT reconstruction of an aliasing-free low-resolution image for coil-profile estimation.*

3.2 Parallel imaging as a nonlinear inverse problem

The quality of auto-calibrated coil profiles depends crucially on the number of autocalibration lines. To reduce scan-time overhead, it is desirable to keep the number of those lines as low as possible. On the other hand, an insufficient number of lines may degrade the estimated profiles to a point where subsequent PI methods yield residual artifacts in the reconstructions. Addressing these limitations, recent publications show that PI reconstructions can be significantly improved by a joint estimation of coil sensitivities and image content [51, 52]. The image acquisition process is hereby understood as an operator A, which maps an image content $\mathbf{M}$ and coil sensitivity profiles $\mathbf{C}_c$ to the measured data vector $\mathbf{y}$. Different to the conventional SENSE approach, the sensitivities are hereby treated as part of the vector of unknowns $\mathbf{x}$:

$$A : \mathbf{x} \mapsto \begin{pmatrix} \mathbf{P}_k\mathbf{F}\left\{\mathbf{C}_1 \ \mathbf{M}\right\} \\ \vdots \\ \mathbf{P}_k\mathbf{F}\left\{\mathbf{C}_N \ \mathbf{M}\right\} \end{pmatrix}, \qquad \mathbf{x} = \begin{pmatrix} \mathbf{M} \\ \mathbf{C}_1 \\ \vdots \\ \mathbf{C}_N \end{pmatrix}. \tag{3.9}$$

With that, the system A becomes nonlinear, such that an actual matrix implementation is not possible anymore. Still Equation (3.9) can be solved by nonlinear numerical optimization. However, without additional constraints, the equation is highly underdetermined - even for the fully sampled case. For example, multiplying the ideal $\mathbf{M}$ in Equation (3.9) by an arbitrary error e does not affect the validity of the solution, if the $\mathbf{C}_c$ are multiplied by the inverse of the error. Hence, an infinite number of physically incorrect solutions will still satisfy the numerical optimization. This problem is solved in [51] by an additional regularization term, which penalizes high frequencies in the spectrum of the coil profiles. Therefore, the operator and the representation of the coil profiles are transformed with a preconditioning matrix $\mathbf{W}$ which contains a polynomial weighting of the Fourier transformed sensitivities:

$$\underbrace{\begin{pmatrix} \mathbf{M} \\ \hat{\mathbf{C}}_1 \\ \vdots \\ \hat{\mathbf{C}}_N \end{pmatrix}}_{\hat{\mathbf{x}}} = \underbrace{\begin{pmatrix} \mathbf{I} & & & \\ & (1+s||\vec{k}||^2)^l \ \mathbf{F} & & \\ & & \ddots & \\ & & & (1+s||\vec{k}||^2)^l \ \mathbf{F} \end{pmatrix}}_{\mathbf{W}^{-1}} \underbrace{\begin{pmatrix} \mathbf{M} \\ \mathbf{C}_1 \\ \vdots \\ \mathbf{C}_N \end{pmatrix}}_{\mathbf{x}} \tag{3.10}$$

with $\mathbf{I}$ the identity, $||\vec{k}||$ the distance to the k-space center, and l and s empirically chosen weighting parameters. A transformed but equivalent system of equations is created

$$\hat{\mathbf{x}} = \mathbf{W}^{-1}\mathbf{x} \tag{3.11}$$

$$\hat{A}\hat{\mathbf{x}} = A\mathbf{W}\hat{\mathbf{x}} = \mathbf{y} \tag{3.12}$$

such that the unknown $\hat{\mathbf{C}}_n$ are defined in frequency domain. Equation (3.12) is subsequently solved with the iteratively regularized Gauss-Newton method (IRGNM).

During this work, the method has been re-implemented using the CG-DESCENT algorithm [53]. The preconditioning has hereby been omitted, keeping the vector of unknowns $\mathbf{x}$ in the image domain. Instead, the regularization term

$$R_c(\mathbf{C}_c) = \left\|(1 + s\|\vec{k}\|^2)^l \ \mathbf{F} \ \mathbf{C}_c\right\|_2^2 \tag{3.13}$$

with the weights $(1 + s||\vec{k}||^2)^l$ has been directly added to the cost function:

$$\Phi(\mathbf{x}) = \frac{1}{2}\|A\mathbf{x} - \mathbf{y}\|_2^2 + \lambda \sum_c R_c(\mathbf{C}_c). \tag{3.14}$$

In addition to being more intuitive, the regularization (3.13) can easily be adapted to other image-space minimization problems, discussed in the later sections of this thesis. However, while the approach produced excellent results for carefully chosen weighting parameters, it turned out to be less robust than the original implementation by Uecker et al. This may be due to numerical disadvantages of the excessive amplifications of high frequency components in the regularization term. The occurrence of high penalty values during reconstruction is precluded when solving the transformed system of equations (3.12) as only the inverse polynomial weightings have to be applied during the iterative optimization. Most coil sensitivity estimations in this thesis have therefore been performed using adapted versions of the original source code[1].

3.3 Advanced image reconstruction models

The framework of parallel imaging methods demonstrates how data acquisition can be accelerated by using the combined data of different receivers to reconstruct a single aliasing-free image from undersampled multichannel data. However, the general idea of exploiting complementary sources of image information is not restricted to sensitivity profiles. In recent years, new techniques have evolved that make use of several different kinds of prior information about data dependencies or image properties. For example, methods based on compressed sensing allow for data reduction by considering the reconstructed images to be sparse in suitably chosen domains [54, 55, 56, 57]. Most recently, such sparsity transforms were extended to the T_1 and T_2 parameter space and used for dictionary-based reconstructions of corresponding maps [58] employing the orthogonal matching pursuit (OMP).

Another strategy is to directly describe sequence specific data-dependencies in a suitable model and then try to estimate the correct model parameters from a set of (potentially undersampled) k-space samples [2, 59, 60, 61, 62]. To categorize this relatively new field of reconstruction methods, the circumscribing term *model-based reconstruction*

---

[1] http://www.eecs.berkeley.edu/~uecker/code.html

has been introduced in the MRI community. An overview of several related studies and methods is given in [63]. Chapters 5 - 8 deal with the realization of respective methods which are tailored specifically to spin-echo based Cartesian data acquisitions.

4

Simulations

The success of a model-based reconstruction technique strongly depends on the ability to accurately model underlying data dependencies. In practice, the MRI data acquisition process comprises several sources of error which can yield violations of the model assumptions. As will be demonstrated in Chapters 5 and 6, these violations in turn can cause artifacts in the reconstructions. In order to elaborate and understand the limitations of the different reconstruction methods, several numerical phantoms have been created during this thesis. These programs allow for the generation of simulated k-space samples with controllable error sources such as Gaussian noise, phase distortions, gradient imperfections, data truncation or violations of the ideal relaxation behavior. In particular, these phantoms also allow for the generation of ideal data which are completely free of any of those errors. As will be shown in Section 5.3.2, a critical weakness of standard models can be found in the effects of data discretization. To analyze related mechanisms, it is beneficial to review the previously introduced image reconstruction procedures from a signal processing perspective. The formalism, introduced in the following section, will be revisited in later sections describing the generation of phantoms (Sections 4.2 and 4.3) as well as for model extensions in Chapter 7.

4.1 Data discretization and truncation artifacts

The MRI signal usually represents the Fourier transform (FT) of an object $M(\vec{r})$ that is bound by a finite field of view, i.e. has compact support. The k-space representation of the object, on the other hand, is usually non-compact and may have infinite support.

As the encoding and processing of infinite continuous data is infeasible, the k-space is normally cut off and sampled at a finite number N of discrete sample points $s[n]$. Subsequent inverse discrete Fourier transformation (iDFT) yields a discrete vector of image pixels $\hat{M}[n]$ that inevitably differs from the original $M(\vec{r})$ in several ways.

The finite sampling procedure can be described as a multiplication of the original signal $s(\vec{k})$ with a comb function

$$\mathrm{comb}(k) = \sum_{n\in\mathbb{Z}} \delta(k-n) \tag{4.1}$$

$$(\delta = \textsc{Dirac}\text{ delta function})$$

and a window function that masks out all data outside a finite sampling period. The process can be written in operator notation:

$$\hat{s}(\vec{k}) = \mathrm{III}_{\Delta k} \cdot \Pi \cdot s(\vec{k}), \tag{4.2}$$

where

$$\mathrm{III}_{\Delta k} = \frac{1}{\Delta k}\,\mathrm{comb}\left(\frac{k}{\Delta k}\right) \tag{4.3}$$

represents a comb function with spacing Δk, and

$$\Pi = \mathrm{rect}\left(\frac{k}{N_s\ \Delta k}\right) \tag{4.4}$$

$$(N_s = \text{number of samples})$$

is the rectangular data acquisition window. $\hat{s}(\vec{k})$ represents the sampled data in continuous space. According to the convolution theorem:

$$\mathcal{F}(f\cdot g) = \mathcal{F}(f) * \mathcal{F}(g), \tag{4.5}$$

the operator multiplications in k-space transform into convolutions with the Fourier transformed operators in image space. With

$$\mathcal{F}^{-1}\ \mathrm{III}_{\Delta k} = \mathrm{comb}\left(\frac{x}{\Delta x}\right) \qquad (\Delta x = 1/\Delta k) \tag{4.6}$$

$$= \mathrm{III}_{\Delta x} \tag{4.7}$$

and

$$\mathcal{F}^{-1}\ \Pi = N_s\ \Delta k\ \ \mathrm{sinc}(N_s\ \Delta k\ \pi x) \tag{4.8}$$

$$= \mathcal{W}, \tag{4.9}$$

the inverse Fourier transform of the sampled data yields

$$\mathcal{F}^{-1}\ \hat{s}(\vec{k}) = \mathcal{F}^{-1}\left[\mathrm{III}_{\Delta k}\cdot \Pi \cdot s(\vec{k})\right] \tag{4.10}$$

$$= \mathrm{III}_{\Delta x}\ *\ \mathcal{W}\ *\ M(\vec{r}) \tag{4.11}$$

which is an infinite periodical replication of the original object M convolved with the sinc function $\mathcal{W}$. The process is illustrated in Figure 4.1 (b - f) for a one-dimensional line of the object in Figure 4.1 (a). In conventional MRI reconstruction, the continuous inverse Fourier transform in Equation 4.10 is replaced by a discrete inverse Fourier transform and only evaluated for a finite number of image space positions, i.e. *pixel*. Object replications therefore have no disruptive effect on the result, as long as the distance Δx is greater or equal the reconstructed field of view. The sinc convolution, however, leads to non-negligible image distortions. The effect is most pronounced on sharp edges or discontinuities of the original object which contain many high-frequency components and thus cannot be accurately recovered from a limited number of discrete Fourier coefficients [64, 65]. Due to their origin and shape, related artifacts are often referred to as truncation, Gibbs-ringing [66, 67] or simply ringing artifacts.

Windowing

The ringing artifacts originate in the convolution of the image with the FT of the sampling window. The choice of the window affects the shape of its FT and thus the induced artifacts. A reduction of image ringing can be achieved by applying a smoother window function. Prominent choices are the Hamming, Kaiser-Bessel or Blackman-Harris window [68]. However, the inherent dampening of high frequencies inevitably induces a certain degree of image blurring and therefore an effective loss of resolution.

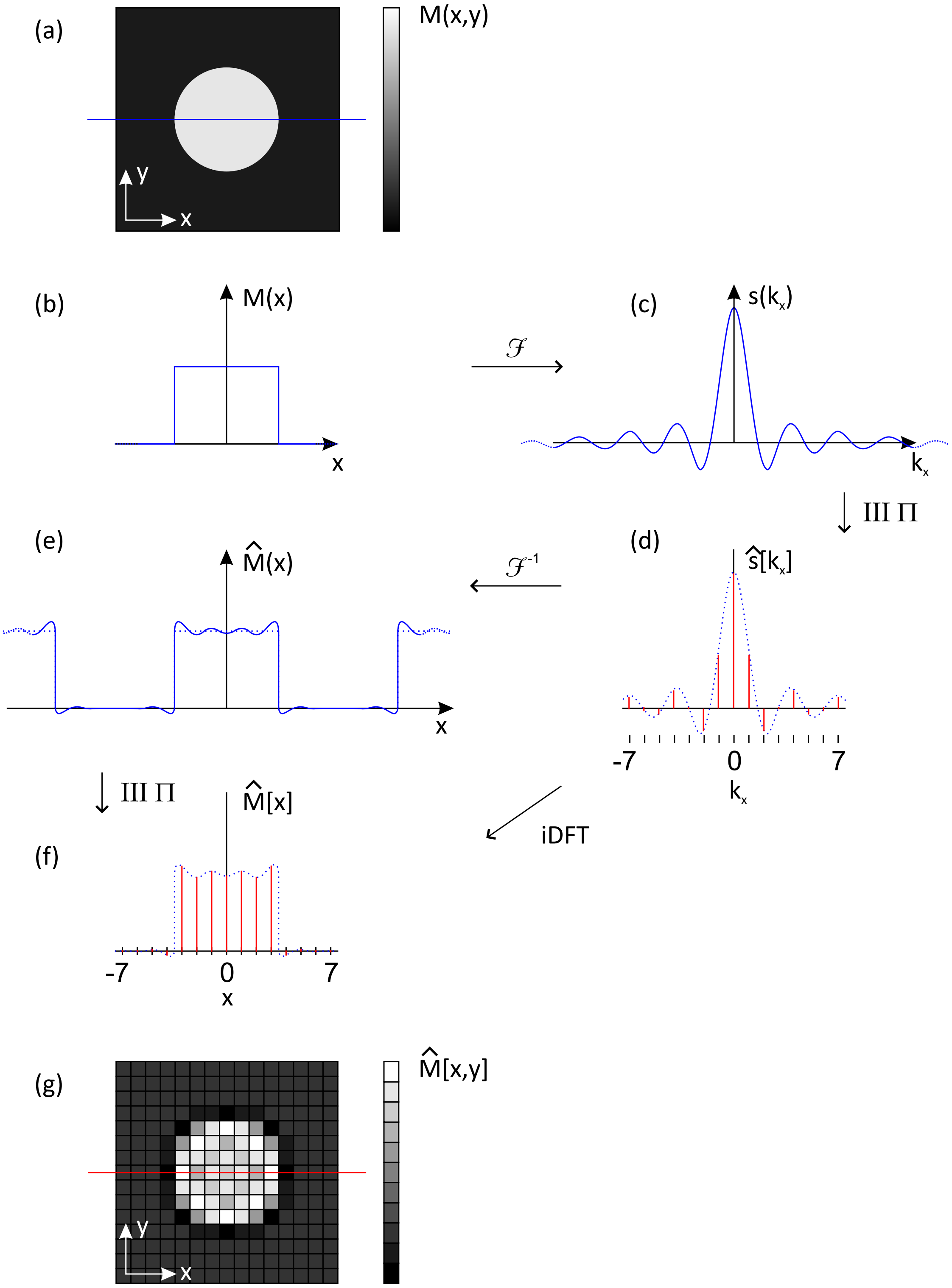

Figure 4.1: *Reconstruction process: (a) Magnetization of a continuous object, coded by gray-scale values (ideal image). (b) 1D line from the center of the image, (c) FT of the line with infinite support, (d) finite number of discrete signal samples, (e) continuous iFT of the samples, (f) iFT of the samples, evaluated at a finite number of discrete points (pixel), (g) matrix of 15 × 15 pixels, coded by 11 quantized gray-scale values (reconstructed image).*

4.2 Pixel-based phantoms

As demonstrated above, traditional image reconstructions in MRI represent the inverse FT of a set of k-space samples, illustrated by pixels in image space. A simple method for the simulation of MRI data is therefore to define an arbitrary image matrix of pixels on a discrete grid and then approximate respective k-space samples from their DFT. This strategy is utilized in Chapters 5 and 6 to study the isolated effects of different error sources. Respective phantoms will be referred to as *pixel-based phantoms* in the following. The advantage and main weakness of this approach are discussed here:

Even though pixels are commonly represented by color-coded two-dimensional areas, the actual basis of these areas are point values without any spatial extent. On the contrary, true objects in MRI can usually be considered as being continuous on a macroscopic level. The difference is illustrated in Figure 4.2 for a continuous rectangular object in image space. The image in (a) represents the idealized object representation on a 15×15 point pixel grid. From a signal processing perspective, a single line of pixels from the object in (a) can be described as a series of Kronecker delta functions at discrete positions in image space, as illustrated by the solid vertical lines in Figure 4.2 (b).

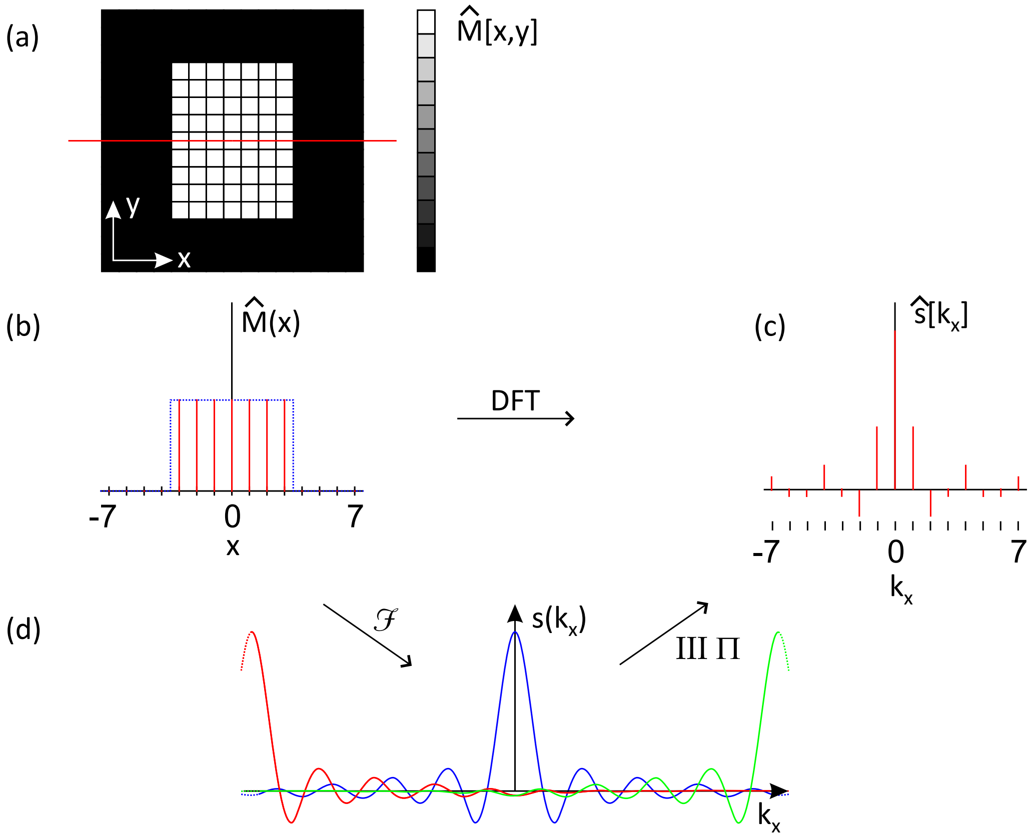

Figure 4.2: *Creation of pixel-based phantom data. A theoretically continuous rectangular object is "sampled" at discrete pixel positions in image space (a, b) and synthetic k-space samples are derived from the pixel's DFT (c). The samples represent the (truncated) superimposition of the replicated continuous FT of the original object (d).*

The pixels can therefore be understood as samples of the originally continuous object in image space (dashed line). Applying the DFT on the pixels is equivalent to calculating the continuous FT of a periodically repeated representation of the image matrix. Accordingly, the respectively synthesized k-space data represents samples from superimposed periodic repetitions of the FT of the original object (Figure 4.2, d) and are therefore rather unrealistic simulations for MRI. However, the implicit periodicity of the simulated k-space data also allows for iDFT reconstructions that are free of the previously described truncation effects. This feature allows for an exclusive analysis of other error sources such as multi-exponential signal evolutions (Section 6.1) or phase perturbations in image space (Section 6.2).

4.2.1 Oversampling

A weakness of pixel-based phantoms in terms of realism is the neglect of object information in-between the pixels. More realistic k-space data simulations are therefore possible by increasing the resolution of the object definition in image space. This *pixel-oversampling* process is illustrated in Figure 4.3 (c). After applying the DFT on the pixels, a good low-resolution approximation of the continuous object in (a) can be gained by only using the central DFT points later on. The accuracy of this approach increases with the oversampling factor.

4.3 Analytical phantoms

More accurate simulations of MRI samples can be gained by constructing phantoms from a composition of primitives, from which the continuous FT is known analytically. For example, the FT of a rect function (Figure 4.3, a) is well known to be a sinc function [69] [70] (Figure 4.3, b). Accordingly, the k-space of a two-dimensional rectangle can be calculated from the relation:

$$s_{\text{rect}}(k_x, k_y) = 2\pi \cdot a_x \cdot a_y \cdot \operatorname{sinc}(a_x \cdot k_x) \cdot \operatorname{sinc}(a_y \cdot k_y), \tag{4.12}$$

where a_y, a_x denote the size of the rectangle in x- and y-direction. A composition of rectangular objects in image space therefore transforms into a superimposition of sinc functions in k-space. Rotation of the individual primitives can be performed according to the rotation property of the FT [69], i.e. by an equivalent rotation of the k-space sample positions. Off-center positioning in image space is possible according to the shifting theorem, i.e. by respective phase modulation of the samples in k-space. As evaluation of Equation (4.12) is valid for any real numbers in $k_{x,y}$, the approach allows for an easy simulation of arbitrary trajectories as well as trajectory imperfections. Simulations performed by this strategy will be referred to as *analytical phantoms* in the following.

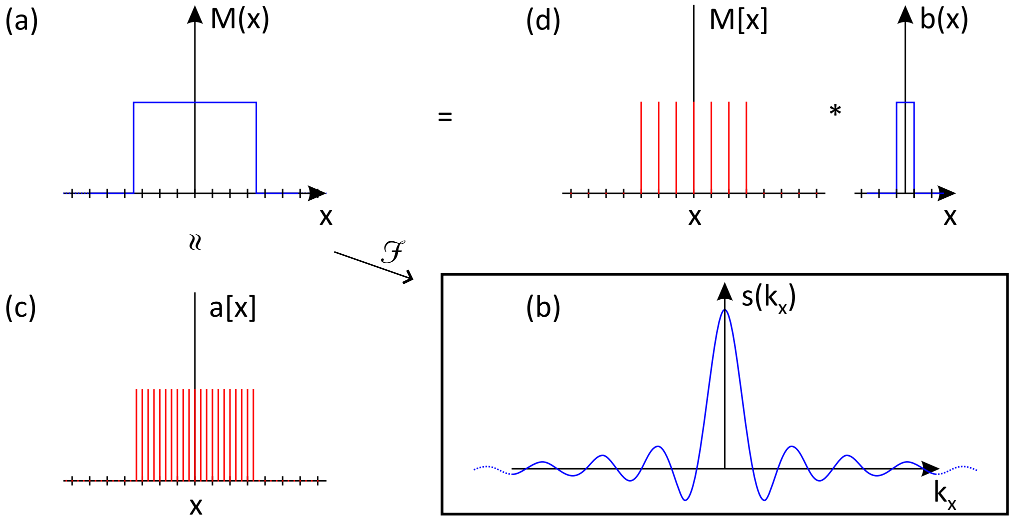

Figure 4.3: *Continuous rectangular object (a) and its analytical k-space signal (b). On a discrete pixel grid, the object can be approximated by a high number of δ functions (c). For the special case of having all object discontinuities positioned exactly in-between adjacent pixel positions, the object in (a) can also be emulated by convolution of a low-resolution δ-comb with a box having the width of the inter-pixel distance (d).*

4.3.1 Elliptical primitives

As demonstrated in the work of Kak and Slaney [71] and Van de Walle et al. [72], the 2D FT of an ellipse can also be expressed analytically. This expression allows to simulate samples from numerical phantoms with elliptical primitives. Using Cartesian coordinates respective k-space samples can be calculated by:

$$s_{\text{circ}}(k_x, k_y) = \frac{a \cdot J_1\left(b \cdot \sqrt{(a/b \cdot k_x)^2 + k_y^2}\right)}{\sqrt{(a/b \cdot k_x)^2 + k_y^2}}, \tag{4.13}$$

with $J_1(\cdot)$ denoting the first-order Bessel function of the first kind and a and b the axes of the ellipse [73]. A three-dimensional analytical representation of an elliptical MRI phantom has been published in 2007 by Koay et al. [74].

4.4 Shepp-Logan phantom

The most prominent schematics for a head phantom were introduced in 1974 by Shepp and Logan [75] [76]. The design mimics the geometric attenuation properties of the head in computerized tomography (CT) and has widely been used to derive simulated CT projections in image space [71]. However, as all features of the phantom are represented by elliptical primitives, it is also suitable for MRI data simulations using the methods introduced before. The design has therefore been incorporated into the data simulation framework. A pixel-based representation of the 2D *Shepp-Logan phantom* is shown in Figure 4.4 (left) for an image matrix of 256 × 256 pixels. An iDFT reconstruction from a respective analytical implementation is illustrated in Figure 4.4 (right). The magnification highlights the difference between the two approaches.

Figure 4.4: *Reconstruction of the Shepp-Logan head phantom from pixel-based (left) and analytical implementation of the original schematics (right). While in (left) the pixel quantization in image space yields staircase-shaped structures, the reconstruction in (right) comprises ringing artifacts at intensity transitions.*

4.5 Relaxation

Modulation of the amplitudes of phantom primitives allows for simulating (multi-) spin-echo data at different echo times TE. Different phantoms have been implemented offering compartments with variable spin-density and T_2 values. The signal decay has hereby been approximated by either traditional mono-exponential modeling (see Section 5.2) or values calculated from a generating function (GF) for CPMG sequences, introduced in Section 8.1. k-space distortion due to T_2 effects during readout have been neglected in both cases. Also a sufficiently high repetition time has been assumed to avoid additional contributions from T_1 effects.

4.6 Transition between discrete and continuous space

Figure 4.5 (left) demonstrates the inverse DFT of samples from an analytical phantom, created from superimposed sinc functions and evaluated for a 256 × 256 point Cartesian data matrix without any trajectory errors. The magnification highlights the occurring ringing artifacts at intensity transitions. The phantom was designed in a way that the transitions between all primitives in image space are positioned exactly in-between pixel positions. The approach assures that every voxel covers a perfectly homogeneous (simulated) spin-density distribution. Due to this special design, the k-space data of the phantom can be understood as the FT of a respective pixel-based phantom, convolved with a box-car function having the width of the inter-pixel distance in image space. An analogue relation is illustrated for a single one-dimensional box in Figure 4.3 (d). As a consequence, all remaining truncation artifacts in Figure 4.5 (left) can be removed by dividing the k-space of the phantom with the FT of a pixel width box-car function. A respective reconstruction is illustrated in Figure 4.5 (center) which is identical to an analog pixel-based implementation of the phantom. However, this "de-ringing" approach fails as soon as any of the primitives is shifted by an arbitrary fraction of the pixel-distance.

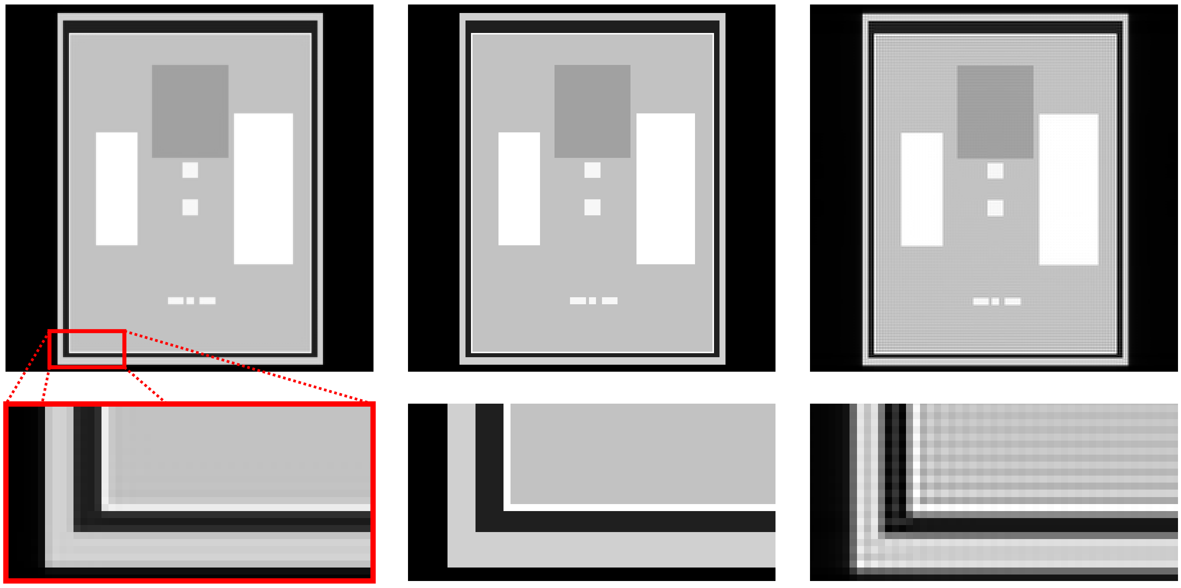

Figure 4.5: *Reconstructions of an analytical phantom from box-shaped primitives. The optimal alignment of all compartments yields minimal ringing in (left), which can be completely removed by proper windowing of the data prior the inverse DFT (center). The ringing is substantially increased when the compartments of the phantom are shifted by half the inter-pixel distance (right).*

4.7 Partial volume effects

Due to limited resolution, most true MR images inevitably contain regions with non-homogeneous spin-density distribution or different tissue types within single voxels. The phenomenon is known as *partial volume effect*. The overlap of different image-intensity regions yields an increase of ringing artifacts. The effect is illustrated in Figure 4.5 (right). Here, all compartments of the phantom have been shifted such that all intensity transitions are placed at the “center” of the later pixel positions. The design yields the worst possible increase of image ringing for the given compartment composition. While rectangular or cubical phantom primitives allow to explicitly control the overlap of image regions, all compartment borders implicitly involve partial volume effects when using elliptical primitives as in Figure 4.4.

Both, partial volume effects as well as ringing can yield violations of the traditional relaxation models for multi-echo experiments [77]. The phenomenon will be shown to cause additional artifacts in some of the relaxometry approaches of the later sections.

5

Model-based T_2 relaxometry from undersampled Cartesian data

As introduced in Section 2.5, the signal evolution in MRI depends on different relaxation effects which are subject to the chemical environment of water protons. In clinical practice, the T_2 relaxation time (or relaxation rate $R = 1/T_2$) is of particular relevance, as it exhibits pronounced sensitivity to pathologic tissue alterations. The spin-echo sequence, introduced in Section 2.4, allows for the acquisition of T_2-weighted images with different contrasts by controlling the echo time TE. However, depending on resolution and TR, the good diagnostic image quality comes at the expense of rather long scan times.

The following chapter deals with the realization of a model-based reconstruction approach designed to substantially speed up the data acquisition process for T_2-weighted images and T_2 relaxometry. The method is based on an iterative nonlinear inversion of a mono-exponential signal model for multiple spin-echo acquisitions and will be abbreviated MARTINI (model-based accelerated relaxometry by iterative nonlinear inversion). Reduction of scan time is achieved by modification of the conventional Cartesian fast spin echo (FSE) protocol. An introduction to the principles of multi-echo aquisitions and FSE extensions is given in the initial section of this chapter (Section 5.1). The treatise is followed by theory and implementation of the MARTINI approach (Section 5.2). An automatic gradient-scaling method is elaborated to avoid ill-conditioning of the reconstruction problem and a dedicated undersampling pattern is introduced to minimize aliasing artifacts in the parameter maps. The method is then evaluated using the data simulation strategies discussed in Chapter 4 as well as human brain MRI data acquired with a conventional clinical MRI system.

5.1 Data acquisition

5.1.1 CPMG sequence

In 1954, Carr and Purcell extended the spin-echo sequence (Section 2.4) by multiple equispaced refocusing pulses [78]. The method allows for observations of the transversal magnetization at multiple echo times within a single repetition. The basic sequence was further improved in 1958 by Meiboom and Gill with the introduction of an alternating pulse phase-cycling scheme to compensate for flip-angle imperfections [79]. Today, implementations of this approach are known as Carr-Purcell-Meiboom-Gill- or CPMG-sequence.

The acquisition of k-space samples from a train of successively refocused spin echoes enables the reconstruction of multiple differently T_2-weighted images without additional scan time requirements. The set of images can further be used for T_2 relaxometry (see Section 2.5.2), for example by pixel-wise fitting of the echo time signal to a mono-exponential curve. However, compared to fast gradient-echo methods like FLASH (fast low angle shot) [80, 81] or FISP (fast imaging with steady state precession) [82], the acquisition of fully sampled CPMG data still requires a substantial amount of scan time.

Figure 5.1 depicts the timing diagram of the fundamental CPMG sequence, which will be the basis of all data acquisitions in the following section. In contrast to the traditional (single-) spin-echo approach, the introduction of additional 180° refocusing pulses causes the occurrence of multiple subsequent echoes after every excitation. The number of these echoes is usually equivalent to the number of applied refocusing pulses and often abbreviated as NE. Within each repetition, sampling of the resulting *echo train* yields one k-space line at every echo time TE. Still, for full k-space coverage, the experiment has to be repeated by the number of phase-encoding steps Np. As in the single-echo approach, the overall scan time is therefore again mainly determined by the product of Np and TR.

Timing limitations

To comply with the *CPMG condition* [5], the echo times in a CPMG sequence are required to be equally spaced. The minimal possible echo spacing Δt is determined by the pulse durations as well as the length of the slice-rephase gradient, the phase-encoding gradient and the frequency-dephase gradient. The latter depend on the field-of-view, bandwidth, and resolution as well as the maximal gradient amplitude and patient safety requirements. Typical values for Δt range from 5 to 25 ms.

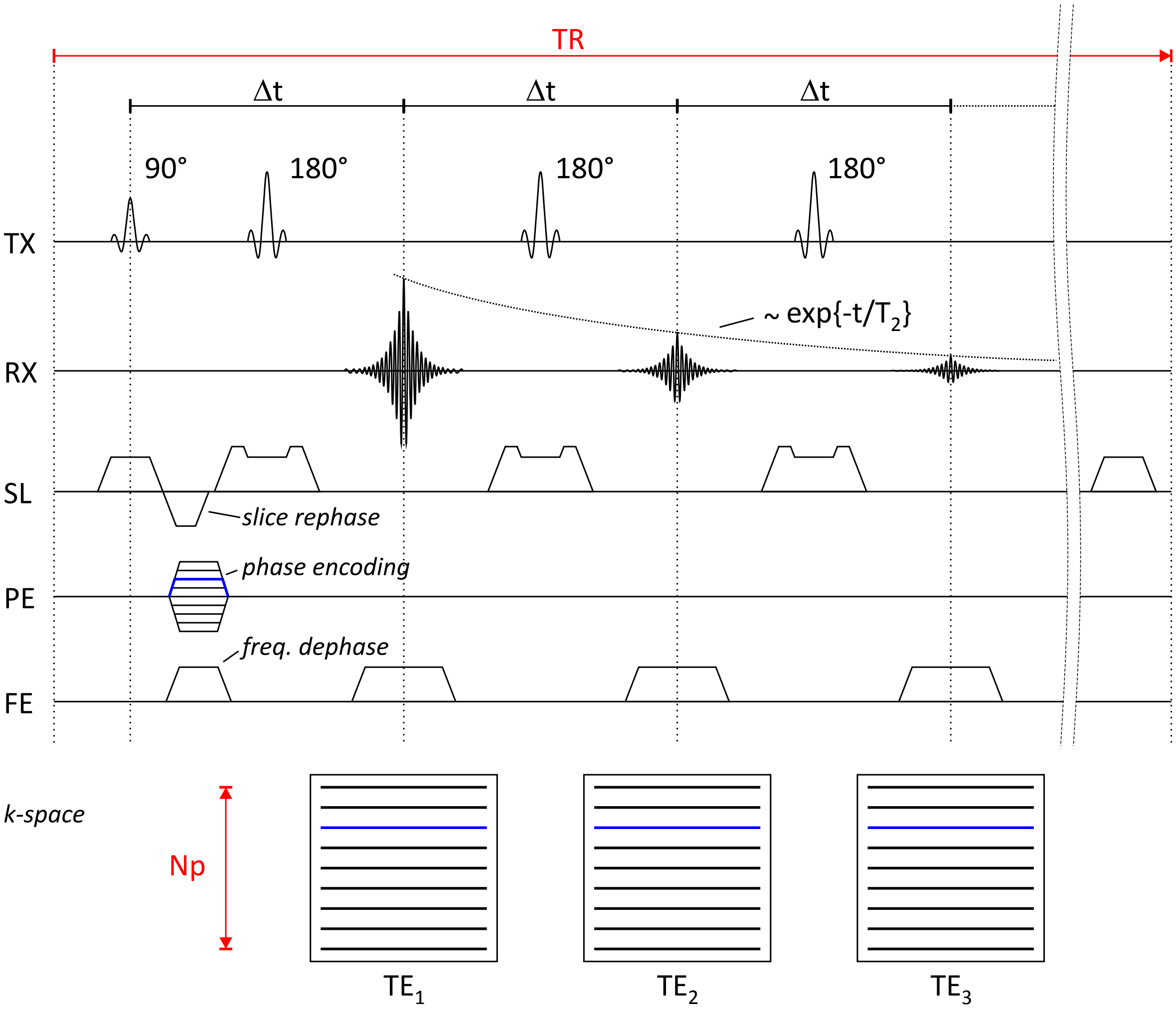

Figure 5.1: *Pulse sequence of the CPMG sequence. The diagram depicts the timing of rf transmission and reception (TX/RX) as well as the gradients for slice selection (SL), phase encoding (PE), and frequency encoding (FE). The sequence yields* NE *fully sampled k-space datasets representing the spin-echo signal at equidistant echo times* $\mathrm{TE}_n = n \cdot \Delta t$*. The overall scan time is determined by the number of phase encoding steps (Np) times the repetition time (TR).*

Number of echoes

Depending on the system's field strength, the T_2 values of most human tissues are smaller than 200 ms [5]. Considering that the signal intensity usually reaches noise level for echo times larger than five times T_2, a reasonable choice for the number of echoes seems to be given by $\mathrm{NE} = 5 \cdot T_{2,\mathrm{max}}/\Delta t$. However, with respect to gradient duty cycles, SAR and disc-space limitations, NE is usually restrained to less than 20 in clinical practice. Accordingly, the maximal echo time is usually smaller than 500 ms. However, the time constants for the longitudinal spin-relaxation (T_1) is in the order of seconds [83, 84]. To avoid T_1 weighting and SNR loss, the repetition time TR should ideally be chosen larger than five times the maximal T_1 within relevant tissue. However, to avoid excessive scan times, TR is often restrained to 2 - 6 seconds in practice. Still, the repetition time is usually much longer than every echo time in the sequence.

Therewith, the overall scan time can be considered independent on the actual number of echoes acquired in every repetition. This explains why a reduction of intermediate images in image space does not accelerate the data acquisition for T_2 relaxometry.

5.1.2 Fast spin echo sequence

The introduction of additional phase-encoding gradients renders the possibility to phase-encode the signal of subsequent echoes differently. By combining the distinctively encoded samples of all echoes to a fully sampled "composite k-space", this strategy allows for a retrospective reconstruction of T_2-weighted images and was originally proposed as single-shot RARE (rapid acquisition with relaxation enhancement) in 1986 [85]. Since then a number of variations and modifications have been developed [86, 87, 88] and many different names have been proposed, including fast spin echo (FSE), turbo spin echo (TSE), fast acquisition interleaved spin echo (FAISE) and others. In the following, the acronym FSE will be used as a collective term.

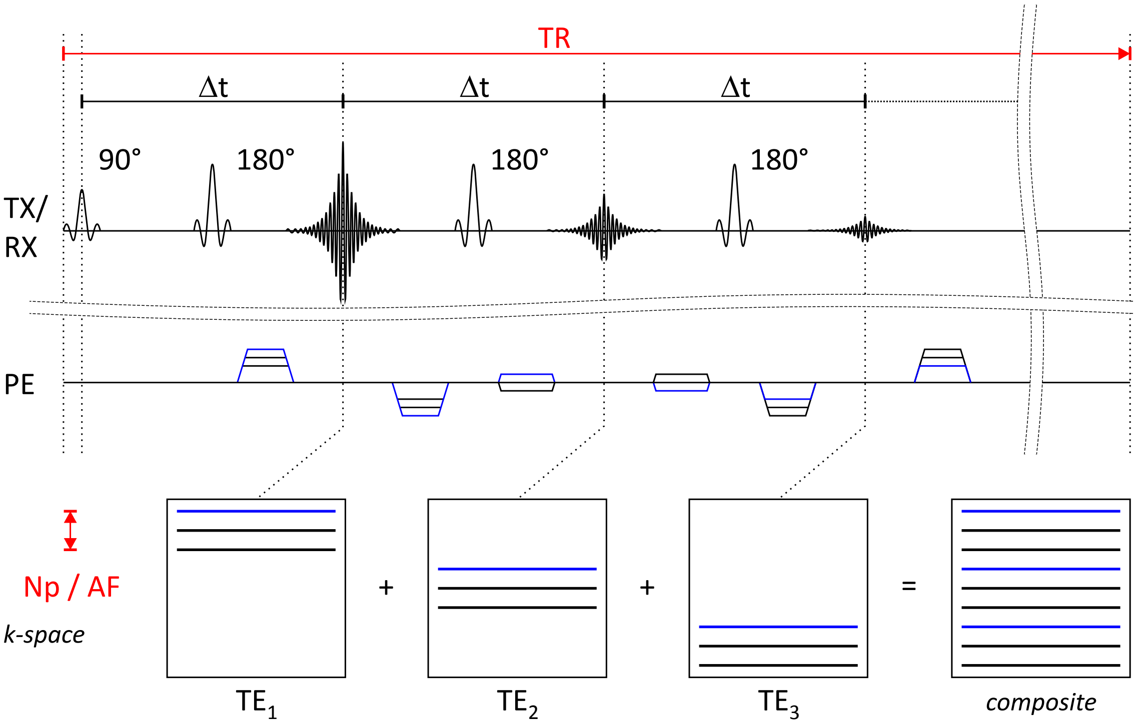

Figure 5.2: *Timing diagram of a fast spin echo sequence for an acceleration factor of 3. The differently phase-encoded k-space lines of subsequent echoes are combined into a "composite" data set, which can be used for image reconstruction by inverse DFT.*

Compared to the traditional (single-) spin-echo imaging, FSE acquisitions allow for a substantial reduction of scan time. The acceleration factor (AF)[1] is hereby given by the number of echoes that are combined in the composite k-space. As image contrast is

---

[1] In the context of FSE, the acceleration factor is sometimes also referred to as the *RARE factor*, abbreviated "RF".

predominantly determined by the low spatial frequencies, FSE reconstructions are often characterized by the *effective echo time* TE_{eff} at which the central k-space lines have been acquired. An exemplary FSE acquisition scheme with an AF of 3 and $\text{TE}_{\text{eff}} = \text{TE}_2$ is illustrated in Figure 5.2.

Unfortunately, reconstructions from composite k-spaces not only yield mixed contrasts, but also cause a certain degree of spatial blurring, edge enhancement, and ghosting artifacts due to the associated alteration of the point spread function [5]. The illustrated sampling pattern in Figure 5.2 is therefore not necessarily the ideal choice for actual FSE imaging and a variety of other encoding schemes can be beneficial instead [89, 90]. However, these limitations are to be resolved with the model-based reconstruction method, described in the following.

5.2 T_2 reconstruction as a nonlinear inverse problem

The MRI signal obtained from a single receiver coil with uniform sensitivity is given by Equation (2.30) which is repeated here for convenience:

$$s(t) = \int M(\vec{r}) \cdot e^{-2\pi i \cdot \vec{r} \cdot \vec{k}(t)} d\vec{r}. \tag{5.1}$$

Again, $M(\vec{r})$ denotes the transverse magnetization, $\vec{r}$ is a position in image space and $\vec{k}(t)$ the chosen k-space trajectory. For spin-echo experiments, the magnetization at echo time TE can be modeled by an exponential decay

$$M_{\text{TE}}(\rho, R) = \rho(\vec{r}) \cdot e^{-R(\vec{r}) \cdot \text{TE}} \tag{5.2}$$

with ρ the spin density and $R(\vec{r}) = 1/T_2(\vec{r})$ the tissue-specific transverse relaxation rate. As the sampling interval is usually much shorter than T_2, the signal decay during the acquisition window is neglected here.

The combination of Equations (5.1) and (5.2) can be understood as a nonlinear model to derive the expected k-space signal $s(t)$ for any pair of estimated parameter maps $\rho(\vec{r})$ and $R(\vec{r})$. For a finite number of samples, the Fourier transform in Equation (5.1) can again be substituted by a two-dimensional DFT, denoted with $\mathbf{F}$ in the following. By stacking all parameter map pixels in a general vector of unknowns $\mathbf{x}$:

$$\mathbf{x} = \begin{pmatrix} \boldsymbol{\rho} \\ \mathbf{R} \end{pmatrix} \tag{5.3}$$

an expected vector of discrete k-space samples can be calculated from the nonlinear system of equations

$$\hat{\mathbf{s}}_{\text{TE}} = \mathbf{P}\ \mathbf{F}\ M_{\text{TE}}(\mathbf{x}). \tag{5.4}$$

In analogy to the single-image reconstruction in Section 3.1, Equation (5.4) is considered to be the forward problem of the aspired reconstruction approach, where $\mathbf{P}$ again holds the coefficients of a binary sampling mask. Reconstruction of the unknown parameter maps in $\mathbf{x}$ can therefore be performed by minimizing the cost function:

$$\Phi(\mathbf{x}) = \frac{1}{2} \sum_{\mathrm{TE}} \|\mathbf{P}\ \mathbf{F} M_{\mathrm{TE}}(\mathbf{x}) - \mathbf{s}_{\mathrm{TE}}\|_2^2 \tag{5.5}$$

yielding a common optimal solution

$$\hat{\mathbf{x}} = \underset{\mathbf{x}}{\operatorname{argmin}} \{\Phi(\mathbf{x})\} \tag{5.6}$$

for all acquired k-space positions and echo times. While $\mathbf{P}$ and $\mathbf{F}$ are linear operators, the model M represents a nonlinear operator. The minimization process therefore requires a sophisticated numerical optimization algorithm capable of dealing with nonlinearities.

5.2.1 Undersampling

The MARTINI approach condenses the total information of all multi-echo samples into only two distinct parameter maps and thereby highlights the pronounced redundancy in the original data. This redundancy may in turn be exploited to reduce the number of phase-encoding steps per echo, i.e. to undersample the k-space for each echo time. Figure 5.3 illustrates the reconstruction procedure for a dataset of 3 echoes and an undersampling pattern that omits every second line in k-space. As shown in Section 5.1.2, the undersampling factor in single-slice FSE acquisitions directly transfers into an equivalent acceleration factor (AF). Compared to conventional full k-space acquisitions, the two-fold undersampling in Figure 5.3 therefore corresponds to a two-fold reduction of scan time.

Undersampling pattern

If Equation (5.2) would correctly model the relaxation process for every pixel, artifact-free reconstructions should be achievable with arbitrary sampling patterns that collect sufficient independent data to cope with the existing unknowns. Similar to the data acquisition of FSE images (Section 5.1.2) it is therefore a good strategy to encode subsequent echoes differently, such that the combined data of several subsequent echoes offer full k-space coverage. With respect to PI methods, a periodically interleaved scheme (Figure 5.4, left) seems a reasonable choice. However, the signal in real images does not always comply with the assumption of a mono-exponential T_2 decay. Besides random errors due to noise, systematic model violations may originate from sequence imperfections, partial volume effects and truncation artifacts. Thus, the minimum of the cost function (5.5) can be expected to be greater than zero even for simulated fully sampled data. As will be shown in Section 5.3, these effects can cause remaining artifacts in the case of undersampling. The underlying reasons for these observations are elaborated in more detail in Chapter 6. However, the practical impact of the

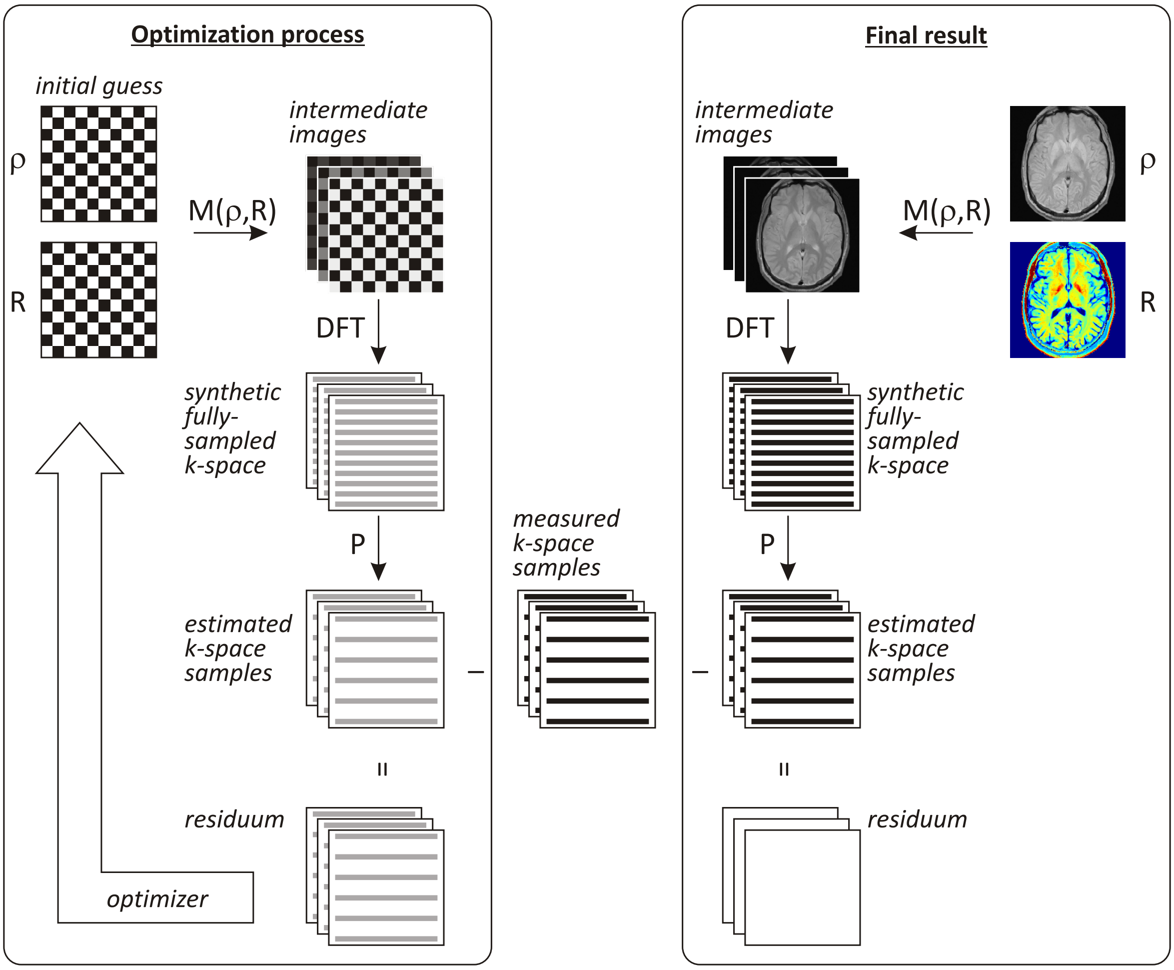

Figure 5.3: *Iterative model-based reconstruction process: (Left) An initial guess of the unknown parameter maps $\boldsymbol{\rho}$ and $\mathbf{R}$ is used to create synthetic fully sampled k-space data. The data is projected onto the trajectory of actually measured data by the operator P. The difference between estimated and measured samples yields a residuum, which is then iteratively minimized by a numerical optimization algorithm. For an optimal result (right) the modeled and measured samples are identical, yielding an empty residuum.*

occuring artifacts has been found to strongly depend on the point spread function of the sampling pattern. For example, the comb-shaped PSF of a periodically interleaved pattern (Figure 5.4, left) can yield distinct aliased copies of model-violating image regions which may be misinterpreted as actual object features. The coherence of these artifacts can be reduced with the use of a random pattern as chosen for reconstructions based on compressed sensing. Because the randomization of k-space acquisitions works most efficiently when applied in two dimensions, this strategy is most promising for 3D MRI. However, for 2D acquisitions, better results will be shown to be achievable by the application of a blocked pattern (Figure 5.4, right). A comparison of the different sampling strategies is given in Section 5.3.2.

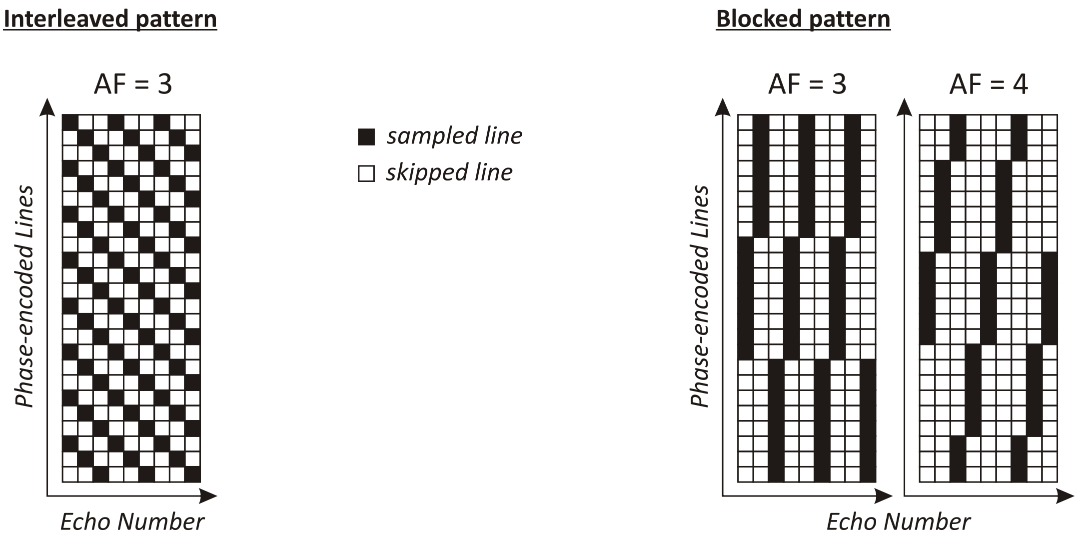

Figure 5.4: *Cartesian encoding with a 3-fold accelerated interleaved undersampling scheme (left) as well as a blocked undersampling scheme for acceleration factors 3 and 4 (right). The example refers to a k-space of 24 phase-encoded lines and 9 echoes.*

5.2.2 Multiple receiver coils

If multiple receiver coils are available, the reconstruction can be combined with PI by including the sensitivity profiles $\mathbf{C}_c$ of the coil elements c into the signal model. Accordingly, Equation (5.5) is extended to

$$\Phi(\mathbf{x}) = \frac{1}{2}\sum_{c}\sum_{TE} \|\mathbf{P}\ \mathbf{F}\ \mathbf{C}_c\ M_{\mathrm{TE}}(\mathbf{x}) - \mathbf{s}_{\mathrm{TE},c}\|_2^2. \tag{5.7}$$

This can improve the condition number of the system of equations, but requires estimates of the coil sensitivities $\mathbf{C}_c$. However, as demonstrated in Figure 5.2, a suitable undersampling scheme can allow for the creation of a composite k-space by combination of multiple echoes. This data can be exploited for coil sensitivity extraction, for example by using the nonlinear inverse approach from Section 3.2. In the following experiments, this strategy was applied as an initial step. To avoid an additional increase of the parameter space, the resulting sensitivities were then kept constant during the minimization of the cost function (5.7).

5.2.3 Phase

While in most clinical applications only the magnitude of the locally varying magnetization vectors is considered, the image-space representation of the actual MRI signal is complex-valued. To account for the potentially varying phase in image space, Equation (5.2) can be extended by a phase map $\varphi(\vec{r})$, yielding:

$$M_{\mathrm{TE}}(\rho, R, \varphi) = \rho(\vec{r}) \cdot e^{-R(\vec{r})\cdot \mathrm{TE} + i\varphi(\vec{r})}. \tag{5.8}$$

Respective extensions of the cost function (5.7) and its gradient allow for a joint reconstruction of a phase vector $\boldsymbol{\varphi}$ and the parameter maps $\boldsymbol{\rho}$ and $\mathbf{R}$. The approach is examined in more detail in Section 6.2. However, for stationary objects, most image-space phase modulation originates from the coil profiles. To avoid an increase of the parameter space, the preluding sensitivity estimation algorithm was therefore constrained such as to shift all phase information into the complex coil sensitivities, while the parameter maps $\boldsymbol{\rho}$ and $\mathbf{R}$ were assumed to be real.

5.2.4 Optimization and gradient scaling

The parameter space of the minimization problem in Equation (5.6) is usually very large[2]. Finding a solution to Equation (5.6) therefore requires a highly efficient optimization algorithm. In [2] the CG-Descent algorithm [53] was proposed in this context. While the method proved to be very efficient for well formulated problems, it also appeared to be very sensitive to variations in the data scaling. To prevent the problem from being *poorly scaled* [91], a heuristically chosen scaling factor for the echo-time vector was introduced by Block et al. [2] which has to be adjusted for different sources of data. Unfortunately, the success and speed of the reconstruction depend crucially on a proper choice of these variables, even for fully sampled data. The effect is demonstrated in Section 5.3.3. To address this problem, a data-driven method is introduced in the following, allowing for an automatic and proper scaling of the reconstruction problem:

To comply with the CPMG condition, the echo times TE are usually equally spaced:

$$\mathrm{TE}_n = n \cdot \Delta t, \tag{5.9}$$

where Δt is referred to as *echo spacing* and n is the *echo number*. With that, the signal model in Equation (5.2) can be simplified to:

$$M_n(\boldsymbol{\rho}, \hat{\mathbf{R}}) = \boldsymbol{\rho} \cdot \hat{\mathbf{R}}^n, \tag{5.10}$$

with $(\cdot)$ denoting point-wise vector multiplication and $\hat{\mathbf{R}} = \exp(-\mathbf{R} \cdot \Delta t)$. By introducing the two additional diagonal scaling matrices $\mathbf{L}_\rho$ and $\mathbf{L}_R$ the modified model function reads:

$$M_n(\tilde{\boldsymbol{\rho}}, \tilde{\mathbf{R}}) = (\mathbf{L}_\rho \tilde{\boldsymbol{\rho}}) \cdot (\mathbf{L}_R \tilde{\mathbf{R}})^n. \tag{5.11}$$

---

[2] For example, a standard MR image matrix size of 256 × 256 pixels yields a vector of unknowns with $N = 2 \cdot 256^2 > 10^5$ entries.

Assuming $\tilde{\boldsymbol{\rho}}$, $\tilde{\mathbf{R}}$ and $\mathbf{P}$ to be real, the gradient of the cost function is

$$\nabla\Phi(\tilde{\mathbf{x}}) = \begin{pmatrix} \nabla_{\tilde{\boldsymbol{\rho}}}\Phi \\ \nabla_{\tilde{\mathbf{R}}}\Phi \end{pmatrix}, \tag{5.12}$$

$$\begin{aligned}
\nabla_{\tilde{\boldsymbol{\rho}}}\Phi &= \sum_c \sum_n \mathbf{L}_\rho \, (\mathbf{L}_R \tilde{\mathbf{R}})^n \, \mathbf{K}_{c,n} && (5.13)\\
&= \sum_c \sum_n \mathbf{L}_\rho \hat{\mathbf{R}}^n \, \mathbf{K}_{c,n}, && (5.14)\\
\nabla_{\tilde{\mathbf{R}}}\Phi &= \sum_c \sum_n n \, \mathbf{L}_R^n \tilde{\mathbf{R}}^{n-1} \, \mathbf{L}_\rho \tilde{\boldsymbol{\rho}} \, \mathbf{K}_{c,n} && (5.15)\\
&= \sum_c \sum_n n \, \mathbf{L}_R^n \hat{\mathbf{R}}^{n-1} \boldsymbol{\rho} \, \mathbf{K}_{c,n} && (5.16)\\
\text{with } \mathbf{K}_{n,c} &= \bar{\mathbf{C}}_c \, \mathbf{F}^{-1} \left[\mathbf{P} \; \mathbf{F} \; M_n(\tilde{\mathbf{x}}) \; \mathbf{C}_c - \mathbf{s}_n\right]. && (5.17)
\end{aligned}$$

where $\bar{\mathbf{C}}_c$ refers to the complex conjugate coil sensitivities and $\mathbf{F}^{-1}$ to the inverse two-dimensional DFT. As a result, the two main components of the gradient near an estimated solution can be equalized using the diagonal scaling matrices

$$\begin{aligned}
\mathbf{L}_\rho &= \left(\sum_n \hat{\mathbf{R}}^n\right)^{-1}, && (5.18)\\
\mathbf{L}_R &= \left(\sum_n n \; \hat{\mathbf{R}}^{n-1} \boldsymbol{\rho}\right)^{-1}. && (5.19)
\end{aligned}$$

If the number of echoes NE is at least twice the chosen acceleration factor, a suitable undersampling scheme can allow for the creation of two or more FSE type images at different effective echo times. With that, an initial estimate for the vectors $\hat{\mathbf{R}}$ and $\boldsymbol{\rho}$ can be created by standard fitting procedures prior to the main reconstruction. However, a direct calculation of pixel-specific scaling matrices from such estimates can provoke disadvantageous gradient amplifications within noisy or low-intensity image regions. A more robust solution was obtained by reducing the diagonal scaling matrices to scalar values derived from the respective means of the initial estimates.

5.2.5 Implementation

The routines for the cost function and its gradients were implemented in MATLAB (MathWorks, Natick, MA), while the iterative optimization was performed using a C implementation of the CG-Descent algorithm. The algorithm was initialized with a homogeneous map of zeros for $\boldsymbol{\rho}$, while the elements of the initial vector for $\hat{\mathbf{R}}$ were set to the mean value of the initial estimate, previously obtained for dimensioning of the scaling variables.

Reconstruction results have been retrospectively filtered by a validity mask, eliminating regions with values below 15 % of the arithmetic mean of the final $\boldsymbol{\rho}$. Also the values of $\mathbf{R}$ were limited to a minimum of $0.2\,\mathrm{s}^{-1}$, corresponding to a maximum T_2 value of 5000 ms.

To compare the reconstruction results with a "gold standard", the MATLAB `nlinfit` program has been used for pixel-wise fitting of an exponential function to the magnitude intensity decay in image space. In contrast to the CG-Descent optimization approach, the gradient has hereby been approximated using the internal finite-difference method rather than the explicit analytical expression.

5.3 Results

5.3.1 Reconstructions from simulated ideal data

To validate the performance of the MARTINI algorithm under ideal conditions, a numerical pixel-based phantom with noiseless and strictly mono-exponential signal decay was defined, offering compartments with equal spin density but different T_2 relaxation times (Table 5.1). Simulated k-space samples for a single receiver coil were derived from the DFT of 16 differently T_2 weighted images (i.e. different echo times) for an image matrix of 150 × 150 pixels and an echo spacing of $\Delta t = 10\,\mathrm{ms}$. Undersampling was performed by selecting respective lines from the fully sampled reference. The respective first-echo data matrix (out of 16) is shown in Figure 5.5 (top) for the fully sampled reference, as well as for simulated undersampling factors of 5 and 15 using the interleaved sampling scheme.

The bottom rows in Figure 5.5 demonstrate parameter map reconstructions from the data using the MARTINI approach for different AF. After 200 CG iterations, the reconstructed values for the fully sampled reference perfectly match with the designated design specifications. A ROI analysis of the uniform spin-density map exhibits a standard deviation of $\delta\boldsymbol{\rho}_1 \approx 10^{-15}$ which is close to the machine precision. The results for 5-fold undersampling are practically identical, even though the SD in the spin-density map is slightly higher after 200 iterations ($\delta\boldsymbol{\rho}_5 \approx 10^{-12}$). Only the highest undersampling factor of 15 yields some barely visible artifacts in the T_2 map (white arrow) which disappear if the number of iterations is increased to 500 (right). On the other hand, for undersampling factors up to 10, visually flawless results are already reached after less than 100 CG iterations.

Using the same idealized phantom data, the experiments have been repeated with the blocked sampling scheme (Figure 5.6). Again, the reconstructed maps after 500 iterations remain visually indistinguishable from the reference up to the maximal undersampling factor of 15.

Compartment:	bottom	center	top	surrounding
ρ [au]	1	1	1	1
T_2 [ms]	50	100	200	500

Table 5.1: *Spin-density and T_2 values of the numerical phantom used in Section 5.3.*

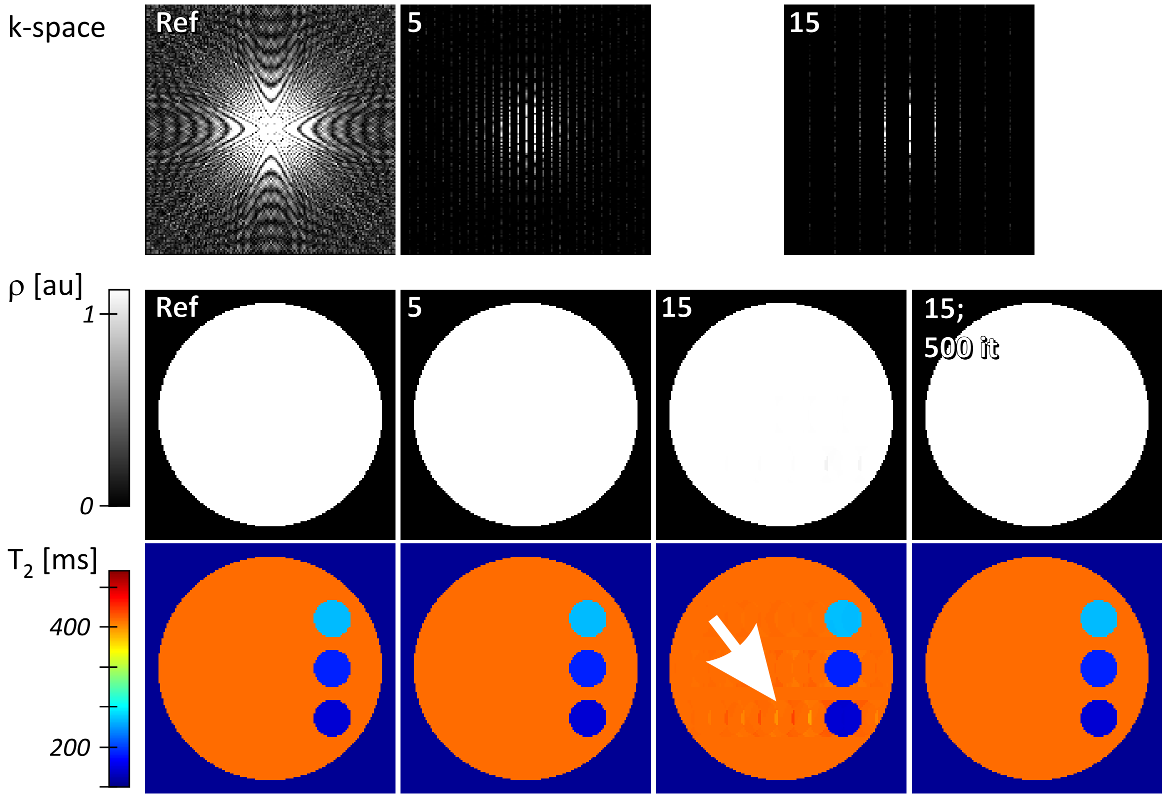

Figure 5.5: *(Top) First-echo k-space and (bottom) reconstructions of a spin-density map (*$\boldsymbol{\rho}$*) and* T_2 *map of a pixel-based numerical phantom. The fully sampled reference (Ref) is compared to MARTINI reconstructions with interleaved undersampling at acceleration factors of 5 and 15 using 200 (5 and 15) as well as 500 CG iterations (15; 500 it).*

When increasing the undersampling factor beyond $\mathrm{NE}-1$, a proper dimensioning of the scaling parameter is not possible anymore, as the initial fitting requires at least two composite k-space datasets with different effective echo times $\mathrm{TE}_{\mathrm{eff}}$. But even when keeping the pre-scaling at a fixed reference, residual artifacts in the reconstruction are ineligible for both sampling patterns, regardless of a high number of 1000 iterations (Figure 5.7).

In general, the maximal possible undersampling for ideal data mainly depends on the number of available echoes with non-void signal intensity in every pixel. For example: When doubling the overall echo time range to $\mathrm{TE}_{max} = 320\,\mathrm{ms}$ by selecting an echo spacing of $\Delta t = 320\,\mathrm{ms}/16 = 20\,\mathrm{ms}$ (rather than 10 ms), reconstructions at 15-fold undersampling and 500 iterations yield artifacts originating from the compartment with the shortest T_2 (50 ms). On the other hand, when increasing the number of echoes within the original echo time range to $\mathrm{NE} = 76$, i.e. selecting a $\Delta t = 160\,\mathrm{ms}/76 \approx 2.1\,\mathrm{ms}$, artifact-free reconstructions can still be achieved with a simulated acceleration factor of $\mathrm{AF}_{max} = 75$, even though a substantially higher number of approximately 2000 iterations is required in this case.

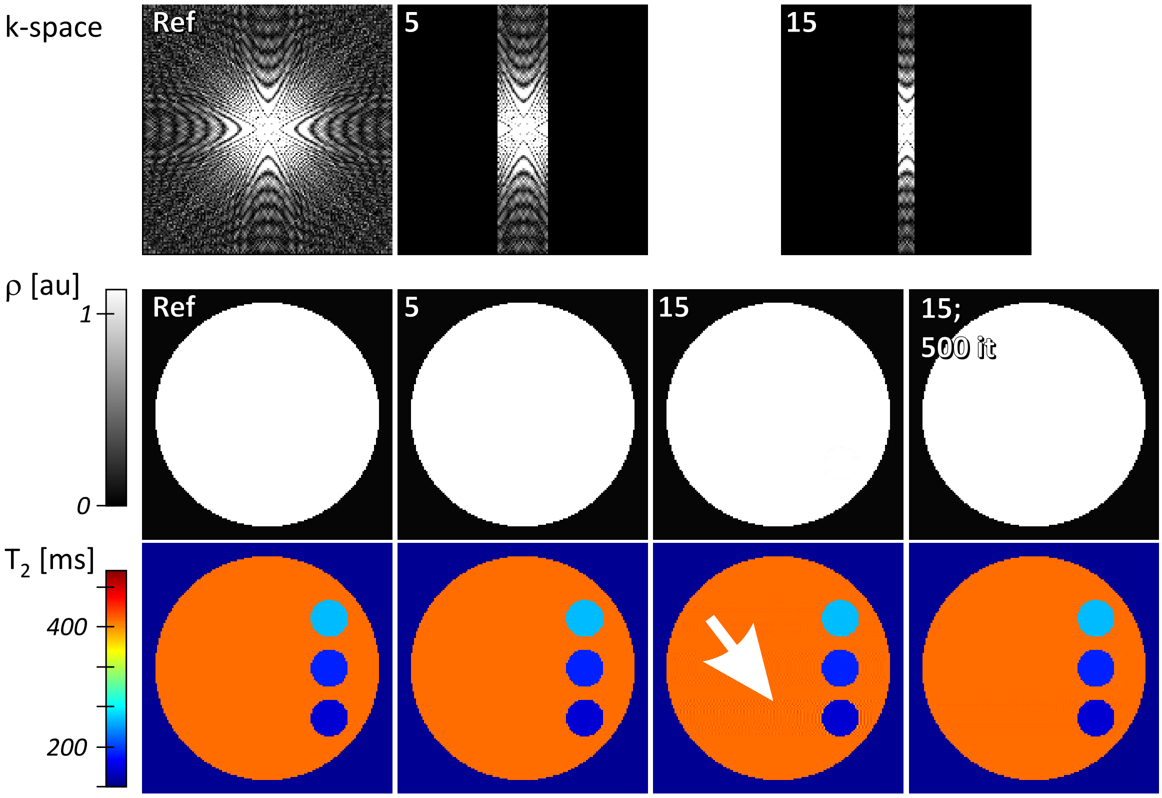

Figure 5.6: *(Top) First-echo k-space and (bottom) reconstructions of a spin-density map ($\boldsymbol{\rho}$) and T_2 map of a pixel-based numerical phantom. The fully sampled reference (Ref) is compared to MARTINI reconstructions with blocked undersampling at acceleration factors of 5 and 15 using 200 (5 and 15) as well as 500 CG iterations (15; 500 it).*

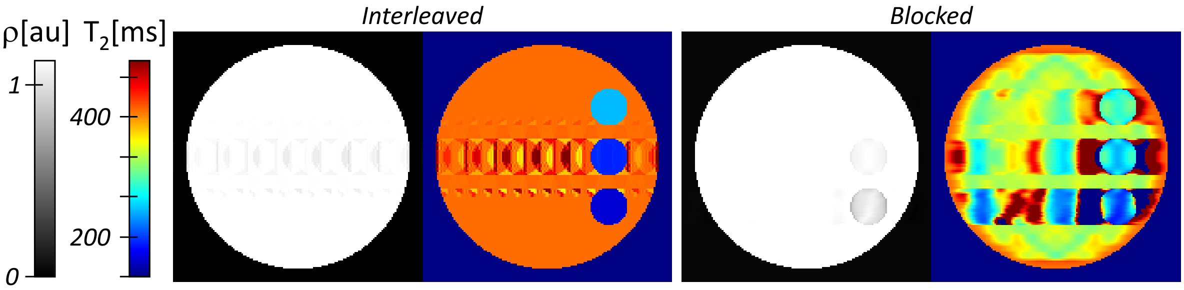

Figure 5.7: *MARTINI reconstructions of a spin-density map ($\boldsymbol{\rho}$) and T_2 map of a pixel-based numerical phantom using 1000 CG iterations and an undersampling factor of $150/9 \approx 16.7$ that exceeds the number of echoes. The results correspond to (left) the interleaved and (right) the blocked sampling scheme.*

5.3.2 Undersampling scheme

As has been mentioned before, the data of true MR images do not always comply with the assumption of a mono-exponential decay. This can already be demonstrated by reconstructing truncated k-space samples derived from analytical rather than pixel-based k-space phantoms. Respective simulations have been performed for a phantom with the same spatial layout as in the former section, using simulated data for a 160×160 image matrix, 16 echoes, echo spacing $\Delta t = 10\,\mathrm{ms}$ and an idealized single receiver coil without noise.

Figure 5.8 (a) shows a T_2 and spin-density map for the fully sampled data and 200 CG iterations. Due to the circular shape, the compartments involve partial volume effects with the surrounding, such that affected voxels exhibit a multi-exponential signal behavior. In addition, the estimated maps reveal residual ringing artifacts at T_2 discontinuities which are most pronounced for the strongest T_2 difference (white arrow) between the first compartment (50 ms) and its surrounding (500 ms). As a consequence, both the compartment borders and the adjacent ringing reappear in the reconstructed spin-density map (black arrow).

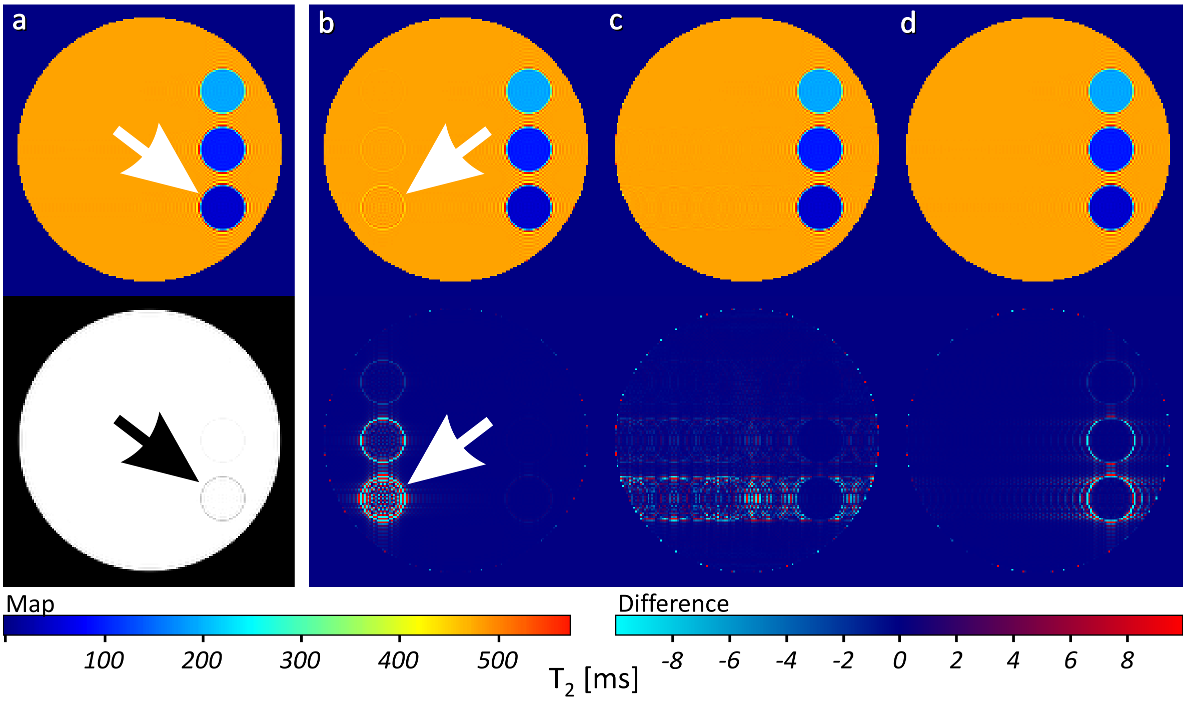

Figure 5.8: *(Top) Estimated T_2 maps of a noiseless numerical phantom from (a) fully sampled data as well as undersampled data using an interleaved (b), a random (c), and a blocked scheme (d). (Bottom) The maps represent the corresponding spin-density map (a) and T_2 difference maps with respect to the fully sampled reconstruction (b-d). Residual artifacts (arrows) refer to ringing in (a) and aliasing in (b), the latter of which is reduced in (c) and (d).*

The application of an interleaved undersampling pattern is demonstrated in Figure 5.8 (b). Despite the fact that the undersampling factor was only 2, aliased copies of the object's discontinuities become visible in the reconstructed maps (arrows).

The situation is improved when using a random pattern. Respective reconstructions are shown in Figure 5.8 (c). Similar to Figure 5.4 (left) the applied pattern was designed in an interleaved manner, where samples from odd echoes were selected randomly while even echoes fill the previously open k-space positions. This strategy turned out to be more efficient than an echo-independent random sampling. As can be seen in the difference maps, the aliasing artifacts are weaker and spread out along the phase-encoding direction of the image.

Finally, Figure 5.8 (d) demonstrates that an even better suppression of artifacts can be achieved with the application of a blocked undersampling scheme, despite residual artifacts restricted to T_2 discontinuities and respective structural borders.

A similar comparison of different sampling strategies is summarized in Figure 5.9 for MRI of the human brain using a single-receiver coil and the scan parameters specified in Table 5.2. The results confirm the observations for simulated data. Based on these findings, all applications of the model-based reconstruction to human MRI data were accomplished with the use of a blocked undersampling scheme.

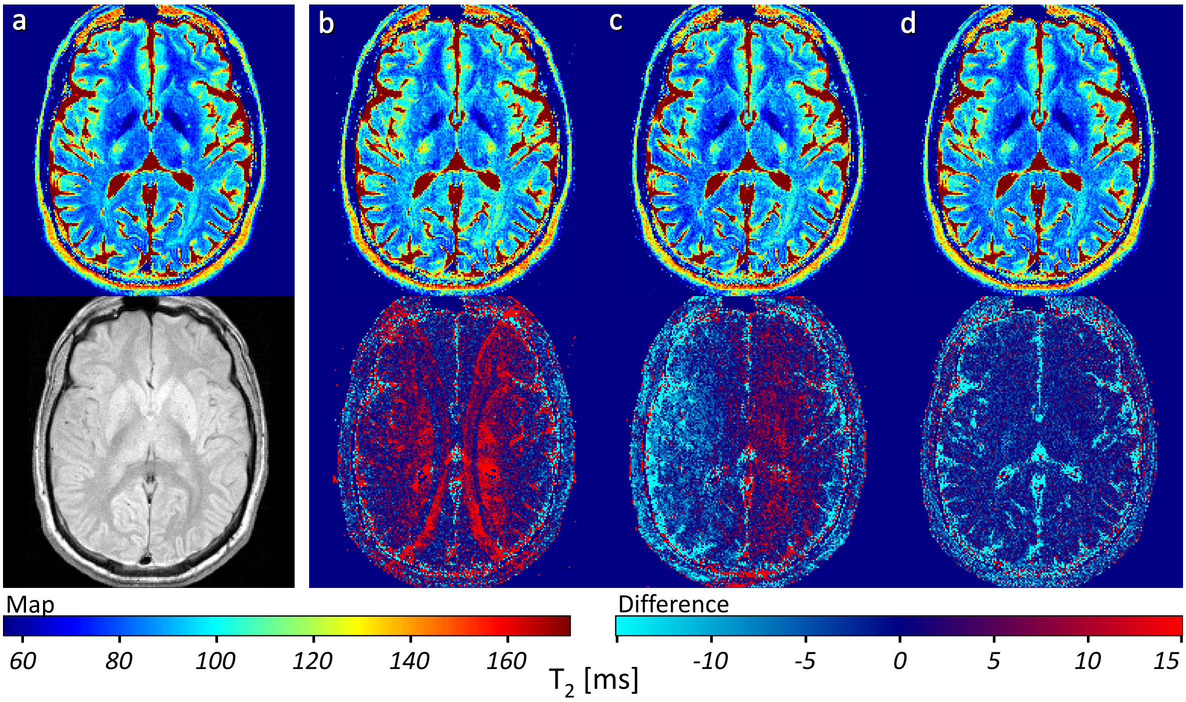

__Figure 5.9:__ (Top) Estimated T_2 maps of the human brain from fully sampled data as well as undersampled data (a) using an interleaved (b), a random (c), and a blocked scheme (d). (Bottom) The maps represent the corresponding spin-density map (a) and T_2 difference maps with respect to the fully sampled reconstruction (b-d).

Scanner hardware	
field strength	3 T
manufacturer	Siemens Healthcare, Erlangen, Germany
system	Tim Trio
MSE Sequence	
NE	32 (only echo 2 to 17 are used later on)
Δt	12.2 ms
FOV	$192 \times 160\,\mathrm{mm}^2$
slice thickness	4 mm
matrix	192×160
TR	3000 ms
scan time	8 min

Table 5.2: *MRI parameters for human brain acquisitions, evaluated in Section 5.3.*

5.3.3 The effect of poor gradient scaling

To demonstrate the effect of poor gradient scaling, reconstructions of fully sampled data from the previously introduced analytical phantom were repeated without the automatic scaling procedure. The images in Figure 5.10 (Man. scale) depict the result after 80 CG iterations, where the scaling matrices $\mathbf{L}_M$ and $\mathbf{L}_R$ have been replaced by the identity $\mathbf{I}$ and the input data has been initially multiplied by a heuristically optimized scalar tuning factor. The results are in close agreement to a reference reconstruction using traditional pixel-wise fitting (Figure 5.11, Fit). To emphasize deviations in compartments with low T_2 values, the images in this example comprise relaxivity maps R_2 $= 1 / T_2$ rather than the clinically more common T_2 maps.

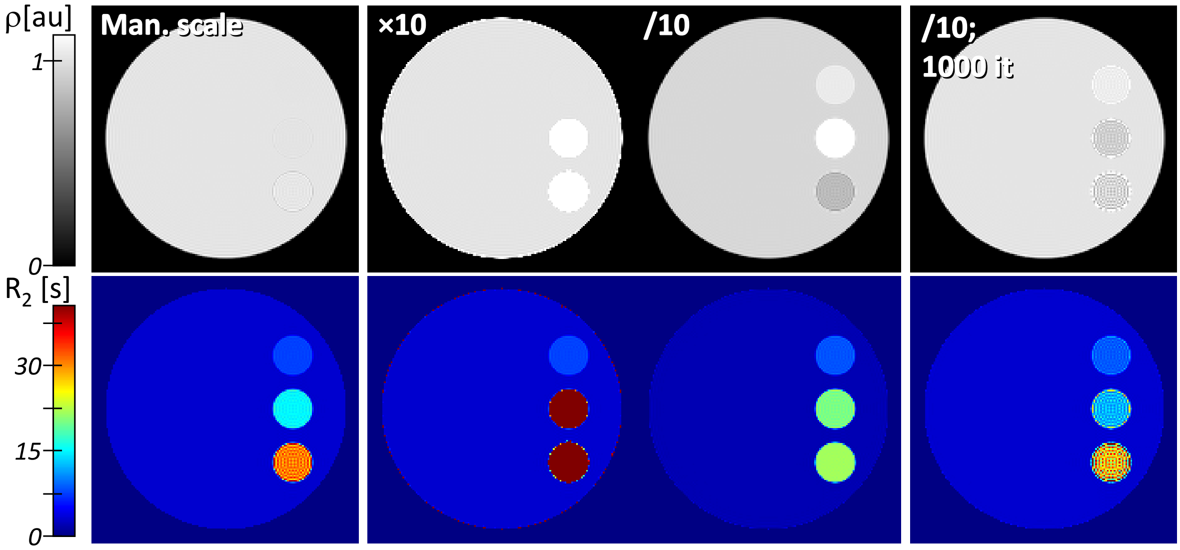

Figure 5.10: *MARTINI reconstructions of a fully sampled numerical phantom at different manually selected tuning factors. At a fixed number of 80 CG iterations, a correct result can only be achieved with optimal tuning (Man. scale). A 10-fold increased or decreased tuning factor (×10 and /10) provokes substantial errors. For the lower factor, the errors are still present when increasing the number of iterations to 1000 (/10; 1000 it).*

Figure 5.10 (×10 and /10) represent MARTINI reconstructions from the same data, where the tuning has been distorted by either multiplication or division by a factor of 10. As a result, the reconstructions strongly deviate from the optimal solution, especially for regions with relatively small T_2 values. While for the higher tuning factor a correct reconstruction can be regained by an approximately two-fold increased number of iterations, reconstruction for the smaller scaling is still erroneous after 1000 CG iterations (Figure 5.10, /10; 1000 it).

Finally, Figure 5.11 (Auto scale) demonstrates that optimal tuning can also be achieved with the automatic gradient scaling procedure, introduced in Section 5.2.4.

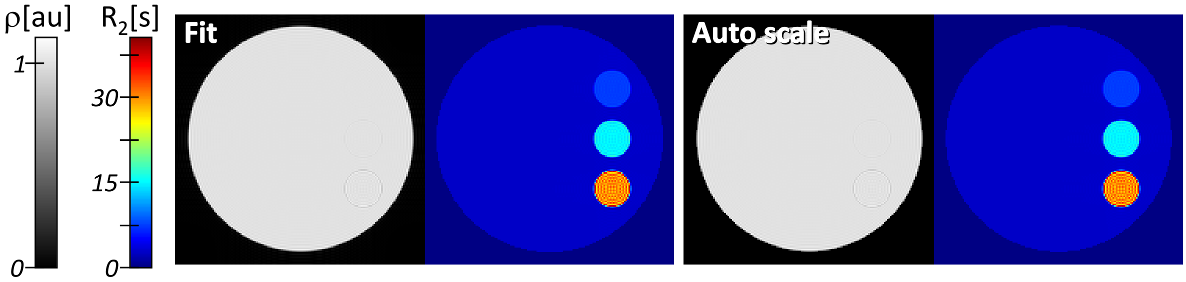

Figure 5.11: *Spin-density and R_2 map reconstructions from a fully sampled numerical phantom. The images in (Fit) correspond to traditional pixel-wise fitting of magnitude images. (Auto scale) refers to MARTINI reconstructions using 80 CG iterations and automatically determined gradient scaling coefficients.*

5.3.4 Quantitative accuracy

To evaluate the accuracy and noise stability of the reconstruction technique, another analytical phantom has been defined offering a much wider range of T_2 values up to 1000 ms. The parameters are summarized in Table 5.3. The presence of noise was simulated by adding Gaussian noise with a standard deviation (SD) ranging from 1 % to 5 % of the uniform spin-density signal. For a given experimental condition and echo train, this was accomplished by adding uncorrelated noise (same amplitude) to the real and imaginary parts of the k-space data of all echoes.

The left column in Figure 5.12 shows reconstructed T_2 maps of the noiseless phantom for different acceleration factors using again the blocked undersampling scheme and a single receiver coil. The compartments of this phantom have been encircled by distinct borders of void signal intensity, precluding partial volume effects with the surrounding. The remaining source of signal deviations from a strictly mono-exponential decay is, therefore, reduced to truncation artifacts. Except for ringing, the reconstructed parameter maps remain free of visible artifacts up to an undersampling factor of approximately 8.9 (160/18). The result for an undersampling factor of 10 slightly differs from the fully sampled map by a barely visible residual aliasing artifact around the compartment with the highest relaxivity difference to the surrounding (green arrow).

The influence of partial volume effects on the reconstruction is demonstrated in the center column of Figure 5.12, where the signal void between the compartments has

NE	16			
Δt	10 ms			
matrix	160 × 160			
compartment	right	lower left	upper left	surrounding
ρ [au]	1	1	1	1
T_2 [ms]	50	100	200	1000

Table 5.3: *Parameters of the numerical phantom used in Section 5.3.4.*

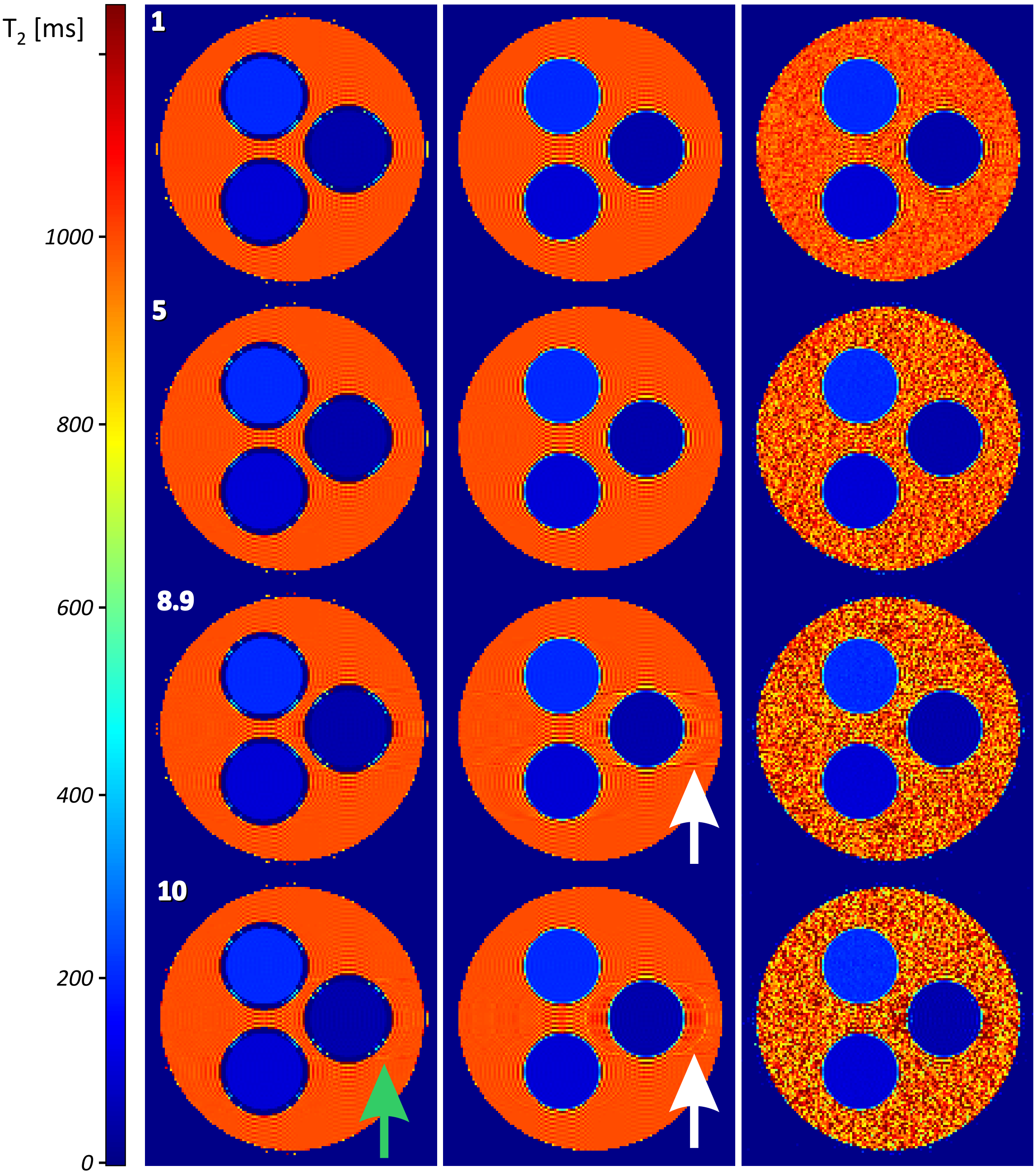

Figure 5.12: *MARTINI reconstructions of T_2 maps from analytical phantoms for undersampling factors of 1, 5, 8.9 and 10. (Left) No noise, compartments isolated from the surrounding, (center) no noise, compartments directly embedded in the surrounding. (Right) same as (center) but with noise corresponding to 1 % SD of the initial spin-density signal for all echoes.*

been removed. The artifacts are now more pronounced and become already visible at 8.9-fold undersampling (white arrow).

In the presence of Gaussian noise with a SD that corresponds to 1 % of the spin-density signal, all aliasing artifacts become invisible as shown in the right column of Figure 5.12.

A quantitative ROI-based analysis of mean T_2 estimates is summarized in Table 5.4. As a “gold standard”, all values are compared with the results of a pixel-based nonlinear least-squares fit of a set of T_2-weighted magnitude images that were obtained by

Undersampling	$T_2 = 50$ ms	$T_2 = 100$ ms	$T_2 = 200$ ms	$T_2 = 1000$ ms
No Noise, Isolated Compartments				
Standard Fitting	50.0 ± 2.2	100.0 ± 1.9	200.0 ± 2.5	1000.0 ± 6.6
1	50.0 ± 2.3	100.0 ± 1.9	200.1 ± 2.4	1000.3 ± 6.6
5	50.0 ± 2.6	100.0 ± 2.0	200.0 ± 2.5	999.6 ± 7.4
8.9	50.0 ± 3.5	100.0 ± 2.2	200.1 ± 2.7	999.3 ± 6.2
10	50.3 ± 5.9	100.0 ± 2.7	200.0 ± 2.8	1000.0 ± 6.8
No Noise, Compartments Without Isolation				
Standard Fitting	50.1 ± 2.6	100.0 ± 2.5	200.0 ± 3.0	1000.0 ± 6.6
1	50.0 ± 2.6	100.0 ± 2.5	200.0 ± 3.0	999.9 ± 6.6
5	50.1 ± 3.1	100.0 ± 2.6	200.0 ± 3.1	1000.0 ± 5.4
8.9	50.2 ± 4.2	100.1 ± 2.9	200.1 ± 3.2	1000.0 ± 10.2
10	50.6 ± 6.5	100.1 ± 3.5	200.0 ± 3.3	1000.4 ± 9.3
Noise Level = 1 % (Compartments Without Isolation)				
Standard Fitting	50.1 ± 2.7	100.1 ± 2.7	200.1 ± 4.4	1004.8 ± 57.8
1	50.0 ± 2.7	100.0 ± 2.6	200.1 ± 4.5	1005.3 ± 58.1
5	50.1 ± 3.9	99.9 ± 4.0	200.5 ± 9.4	1021.9 ± 152
8.9	50.7 ± 7.1	100.2 ± 5.7	200.6 ± 10.7	1039.2 ± 208
10	52.9 ± 12.9	100.8 ± 6.6	201.1 ± 12.0	1058.5 ± 260
Noise Level = 5 % (Compartments Without Isolation)				
Standard Fitting	52.8 ± 4.6	102.3 ± 7.3	201.8 ± 17.3	1137.0 ± 484
1	50.1 ± 4.4	101.2 ± 7.6	200.3 ± 16.5	1138.7 ± 521
5	51.5 ± 14.1	104.3 ± 18.3	208.0 ± 44.6	n.a.
8.9	55.2 ± 22.7	107.0 ± 31.3	217.6 ± 65.2	n.a.
10	54.1 ± 28.1	110.0 ± 37.3	255.8 ± 498	n.a.

Table 5.4: *T_2 relaxation times from MARTINI reconstructions of numerical phantoms. T_2 values (ms) represent mean ± SD, n.a. = not available. Noise levels are characterized by their SD in percent of the uniform spin-density signal. Standard pixel-based fitting refers to a set of fully sampled T_2-weighted magnitude images.*

(inverse) DFT of the respective fully sampled k-space data. The influence of Gaussian noise has been evaluated for SD levels of 1 % and 5 %, which correspond to SNR values of 100 and 20 (single coil). For comparison, fully sampled studies of the human brain resulted in a SNR above 200 (initial echoes) for multi-channel recordings, and above 40 for the single coil. Simulations were performed for undersampling factors of 1, 5, 8.9 and 10.

For noiseless data, all T_2 estimates closely agree with the values obtained by standard fitting and are very accurate up to the highest undersampling factor of 10. Residual T_2 deviations have to be ascribed to truncation artifacts, as the removal of the compartment isolations only causes negligible changes in the SD values, and the reconstruction

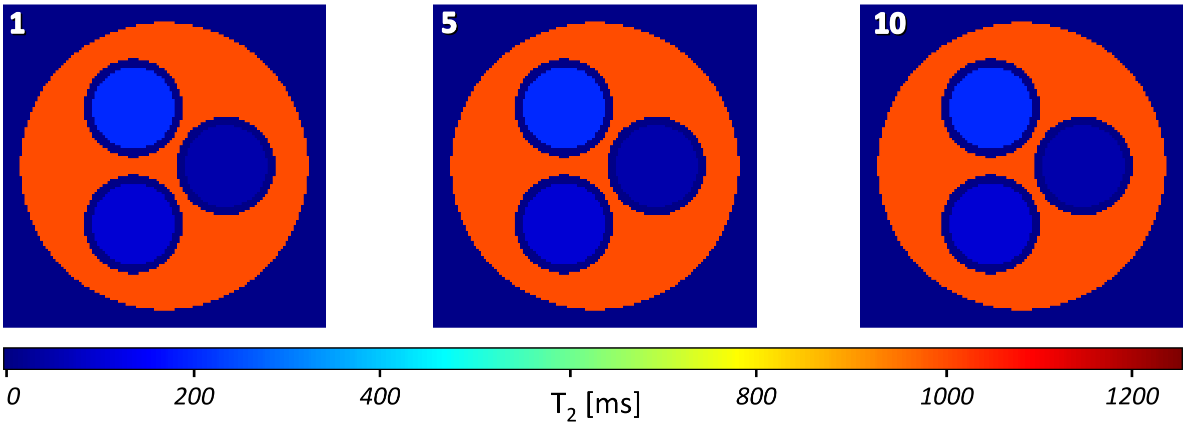

Figure 5.13: *MARTINI reconstructions of T_2 maps from a pixel-based phantom without noise for undersampling factors of 1, 5, and 10.*

accuracy for a ringing-free pixel-based version of the same phantom (Figure 5.13) can again be pushed close to the machine precision for all the undersampling factors up to 10.

Similar good results are obtained for the condition with 1 % noise, although at the expense of slightly increased SD values for the T_2 estimates. In this case, the mean T_2 values up to 200 ms deviate from the correct values by less than 2 % for undersampling factors up to 8. Larger errors of up to 4 % for the compartment with $T_2 = 1000$ ms must be ascribed to the fact that the 16 simulated echoes covered a period of only 160 ms which is far from being adequate for long T_2 relaxation times. This effect becomes stronger for higher acceleration factors and noise levels. While the results for a 5 % noise level still allow for an undersampling factor of 5, when accepting a 4 % error for T_2 estimates up to 200 ms, some T_2 estimates in the surrounding become limited by the applied mask. Pertinent results are discarded.

5.3.5 Imperfection of the CPMG echo train

Unfortunately, in addition to truncation, true MR images suffer from several side effects that perturb the signal acquisition. Besides flow and diffusion [92] as well as static field inhomogeneity [93], unwanted stimulated echoes due to radiofrequency pulse imperfections can superimpose to the spin-echo signal and yield deviations from the mono-exponential model. These model violations can cause major errors in the estimation of T_2, even for traditional magnitude fitting [94] [95]. Especially in 2D multi-slice CPMG acquisitions the signal strength of the first echo is often systematically lower than that of the second echo. An example is shown in Fig. 5.14 (left) for the signal decay of a single selected pixel from a fully sampled CPMG echo train of the human brain using the parameters in Table 5.2.[3]

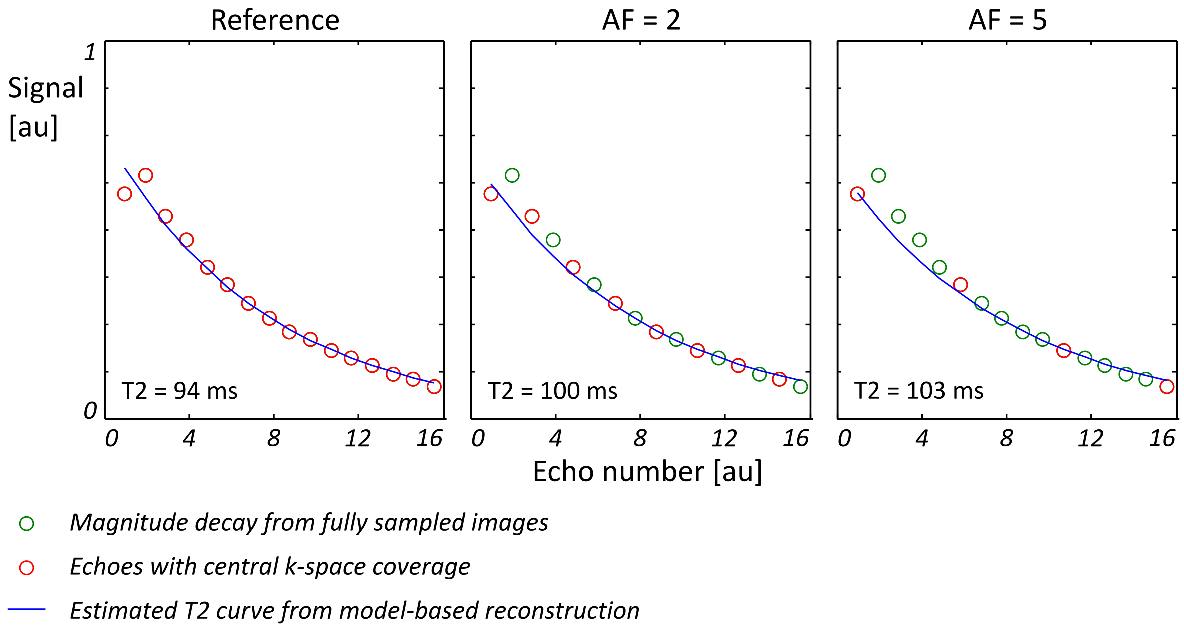

Figure 5.14: *Signal decay in a single pixel from a CPMG acquisition of the human brain. Circles represent magnitude intensity values from fully sampled reference images. The curves represents the result from MARTINI reconstruction using fully sampled as well as 2- and 5-fold undersampled data (blocked pattern). Red circles mark the echo times at which central k-space positions have been acquired. The procedure causes a drift in the reconstructed T_2 that depends on the undersampling / acceleration factor (AF).*

As the image-intensity information is not equally distributed in k-space but predominantly condensed in the central samples of k-space, the hypo-intense first echo from CPMG acquisitions can cause a systematic drift of the estimated T_2 values when using undersampling. For example, if the blocked sampling scheme is used, central k-space lines are only covered every AF echoes. As a consequence, the relative influence of the

---

[3] As can be seen from the sequence parameters, the original dataset involved 32 echoes with full k-space sampling. However, because the latest echoes exhibit very low SNR, only the first 16 echoes are considered here.

first echo with respect to the rest of the echo train increases with higher acceleration. The effect is demonstrated in Fig. 5.14 (center) and (right). The drift in T_2 estimates can be reduced when shifting the sampling scheme in a way that the first central block is covered in the second echo, rather than the first one. However, we observed that this practice can increase the occurrence of undersampling artifacts in the reconstructions. Better results could be achieved by simply discarding the samples of the first echo, which seems to be common practice even for traditional magnitude fitting [96] [97]. The superior stability of T_2 values is demonstrated in Fig. 5.15.

As a consequence, all reconstructions in the following section are performed by neglecting the first echo. Also, due to the SNR limitations in later echoes and to decrease unnecessary SAR exposure in follow-up studies, the analyzed data are restricted to echoes 2 to 17.

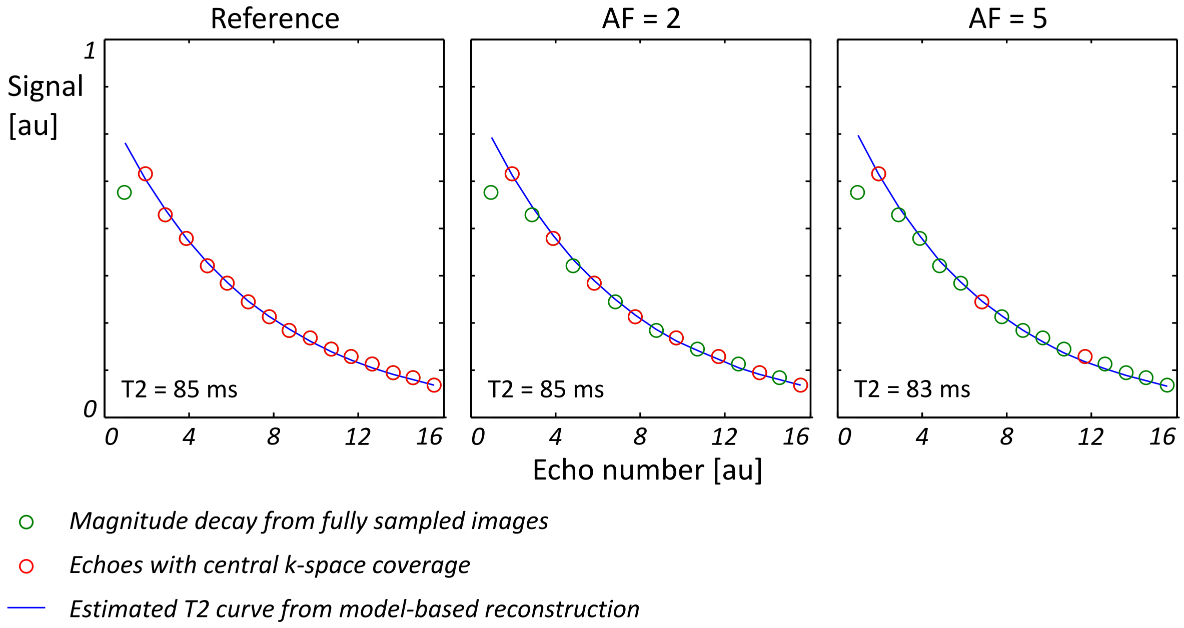

Figure 5.15: *Signal decay in a single pixel from a CPMG acquisition of the human brain. Circles represent magnitude intensity values from fully sampled reference images. The curves represents the result from model-based reconstruction from fully sampled as well as 2- and 5-fold undersampled data, where the first echo has been discarded. Red circles mark the echo times at which central k-space positions have been acquired. The reconstructed T_2 values remain relatively stable for the different acceleration factors.*

5.3.6 Human brain reconstructions at different acceleration factors

To demonstrate the performance of the MARTINI method, spin-density and T_2 maps of the human brain (scan parameters in Table 5.2) have been reconstructed for different degrees of undersampling using the blocked scheme and a single-element head coil for data acquisition. The results are illustrated in Figure 5.16 and again compared with a pixel-based fit of fully sampled magnitude images. As can be seen, the parameter maps from the MARTINI reconstructions remain free of visible artifacts up to an undersampling factor of 5. However, with this coil the SNR decrease for fewer acquisitions becomes already visible for undersampling factors larger than 2. The experiment was, therefore, repeated with a 32-element head coil as shown in Figure 5.17. In this case, the magnitude images for the pixel-based fit were obtained from the sum-of-squares of the Fourier transformed data of all individual coil elements. The MARTINI reconstruction benefits from the much better SNR and yields acceptable T_2 maps for an undersampling factor of at least 5. The reconstructions for a factor of 10 exhibit small artifacts such as vertical ghosts near the hemispheric fissure.

Complementing the determination of parameter maps, MARTINI reconstructions allow for the estimation of T_2-weighted images at arbitrary echo times. Figure 5.18 depicts respective images (same section as in Figure 5.17) for an undersampling factor of 5 and echo times that range from spin-density contrast to weak, moderate, and strong T_2 contrast. Unlike conventional fast spin-echo images, these images exhibit “true” T_2 contrast for the chosen echo time (rather than a mixed contrast of several echo times). They also remain free from blurring which arises from a modulation of the point spread function when combining phase-encoded echoes with different intensities.

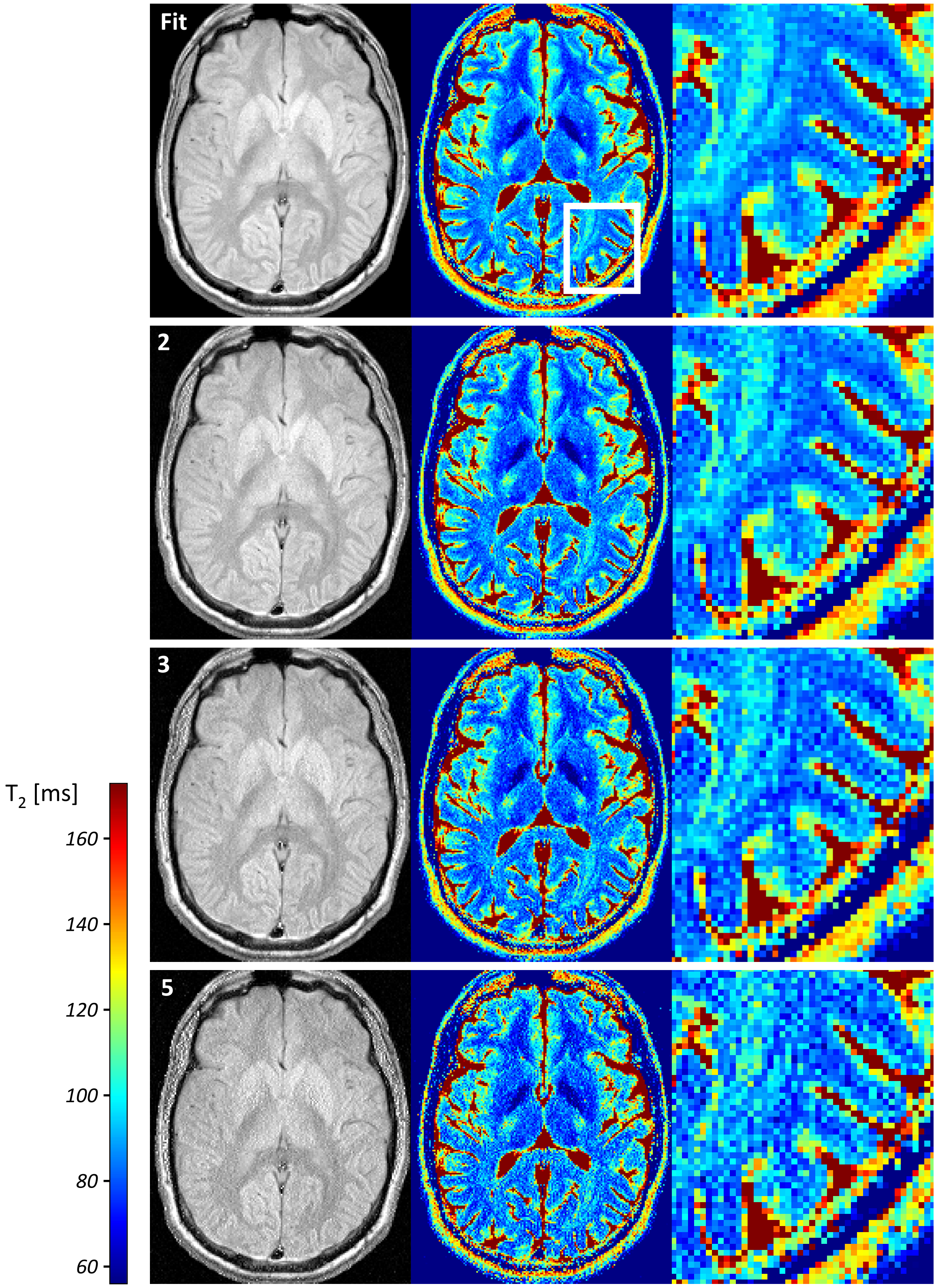

Figure 5.16: *Standard fitting (fully sampled k-space data) versus MARTINI reconstructions of (left) spin-density and (center, right) T_2 maps of the human brain for a single receiver coil and undersampling factors of 2, 3, and 5.*

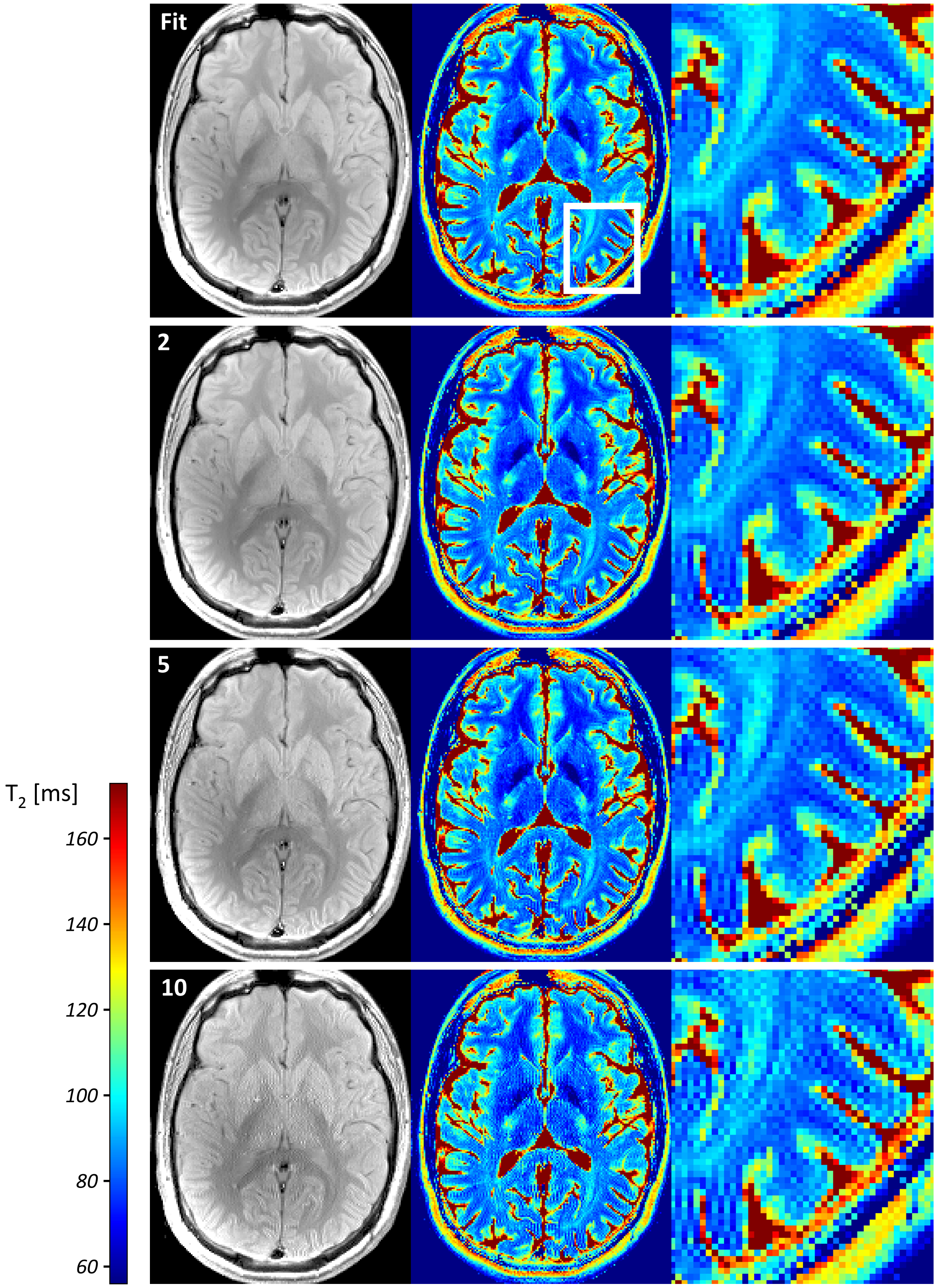

Figure 5.17: *Standard fitting (fully sampled k-space data) versus MARTINI reconstructions of (left) spin-density and (center, right) T_2 maps of the human brain for a 32-element coil and undersampling factors of 2, 5, and 10.*

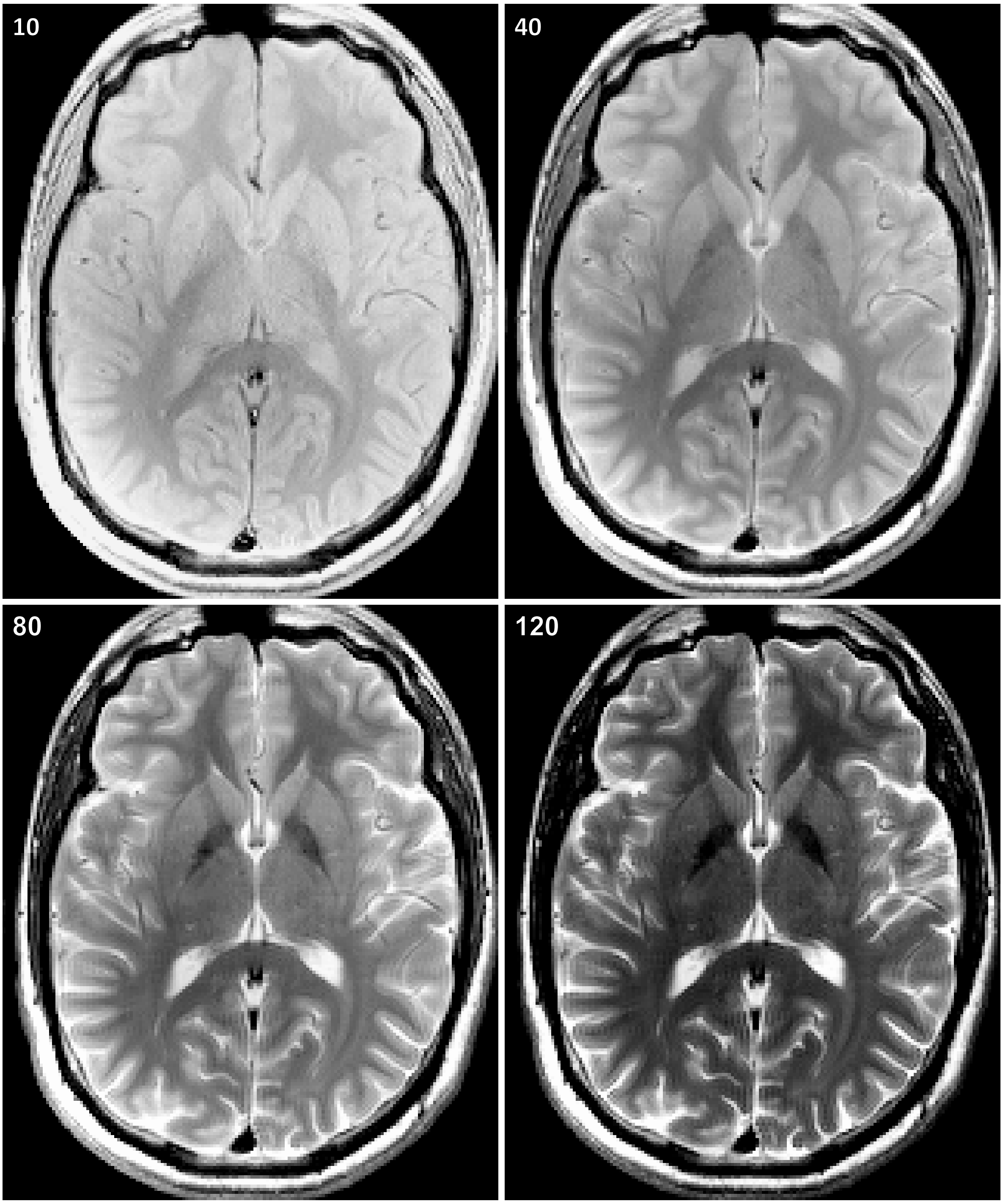

Figure 5.18: *"Synthetic" T_2-weighted images from MARTINI reconstructions of a spin-density and T_2 map of the human brain with an undersampling factor of 5. The echo times TE = 10, 40, 80, and 120 ms correspond to spin-density contrast as well as weak, moderate, and strong T_2 contrast, respectively.*

ROI analysis

Table 5.5 summarizes T_2 estimates for different regions-of-interest in the human brain reconstructions as a function of the degree of undersampling. A visualization of the data is given in Figure 5.19. The T_2 values obtained from the MARTINI reconstruction are in good agreement with those obtained from the fully sampled datasets even for undersampling factors up to 10. For the fully sampled data, the T_2 values of the pixel-based fit are slightly higher than those obtained by model-based reconstruction. This may be due to fitting magnitude images that are contaminated with noise in the late echoes. The discrepancy is removed, if the curve fitting is applied to the real-part

		Undersampling Factor			
	Std. Fitting	1	2	5	10
Anterior Cingulate	100 ± 10	99 ± 10	98 ± 10	98 ± 10	98 ± 10
Insular Cortex	94 ± 5	93 ± 5	93 ± 5	92 ± 5	93 ± 6
Thalamus	81 ± 4	79 ± 4	78 ± 4	78 ± 5	78 ± 8
Lentiform Nucleus	78 ± 4	77 ± 8	77 ± 5	76 ± 5	78 ± 6
Caudate Nucleus	88 ± 5	87 ± 5	86 ± 5	86 ± 5	87 ± 9
Internal Capsule	56 ± 5	54 ± 6	55 ± 6	52 ± 7	54 ± 12
Frontal White Matter	74 ± 2	74 ± 2	73 ± 2	72 ± 2	74 ± 4

Table 5.5: *T_2 relaxation times from MARTINI reconstructions of the human brain. T_2 values (ms) represent mean ± SD. Standard pixel-based fitting refers to a set of fully sampled T_2-weighted magnitude images.*

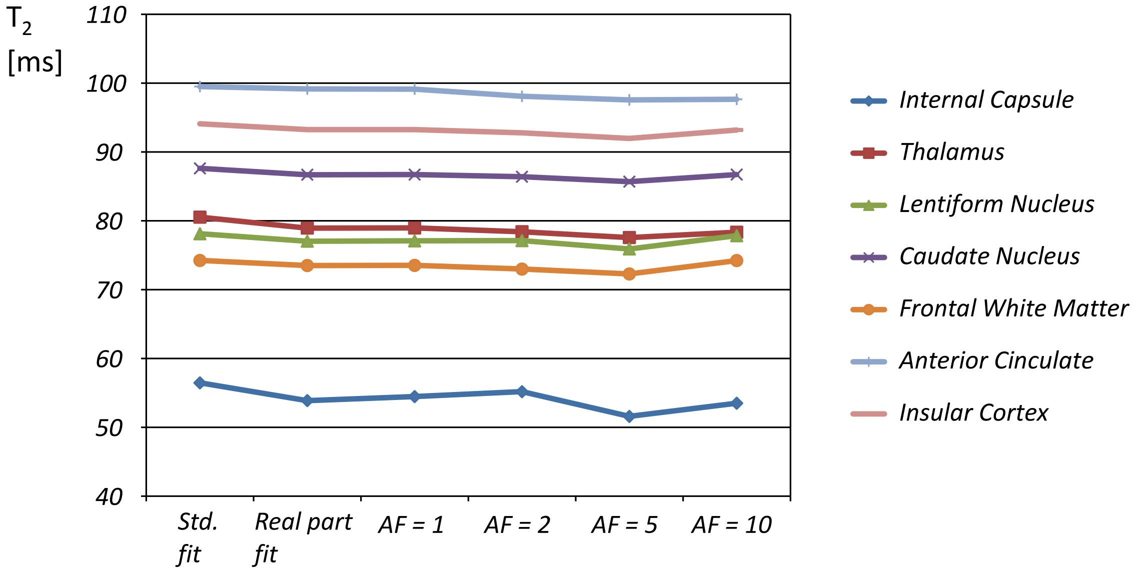

Figure 5.19: *T_2 relaxation times from MARTINI reconstructions of the human brain. Standard and real part pixel-based fitting refers to a set of fully sampled T_2-weighted images created by RSS channel combination as well as real-part images obtained from Equation (2.33).*

of images obtained from Equation (2.33) using the same coil-sensitivities as for the model-based reconstruction (Real part fit).

5.3.7 Parallel imaging

To compare the MARTINI reconstruction technique with parallel imaging, the first-echo images of the 32-channel human brain data have also been reconstructed using the approach from Section 3.2. Undersampling has been performed using conventional comb-shaped pattern with 24 autocalibration lines (ACL). Figure 5.20 depicts the results for undersampling factors of 2, 3, and 5 corresponding to net acceleration factors of 1.7, 2.3 and 3.1 (considering the ACL). Artifacts can already be observed for a net acceleration factor of 2.3 which is far below the possible acceleration using MARTINI.

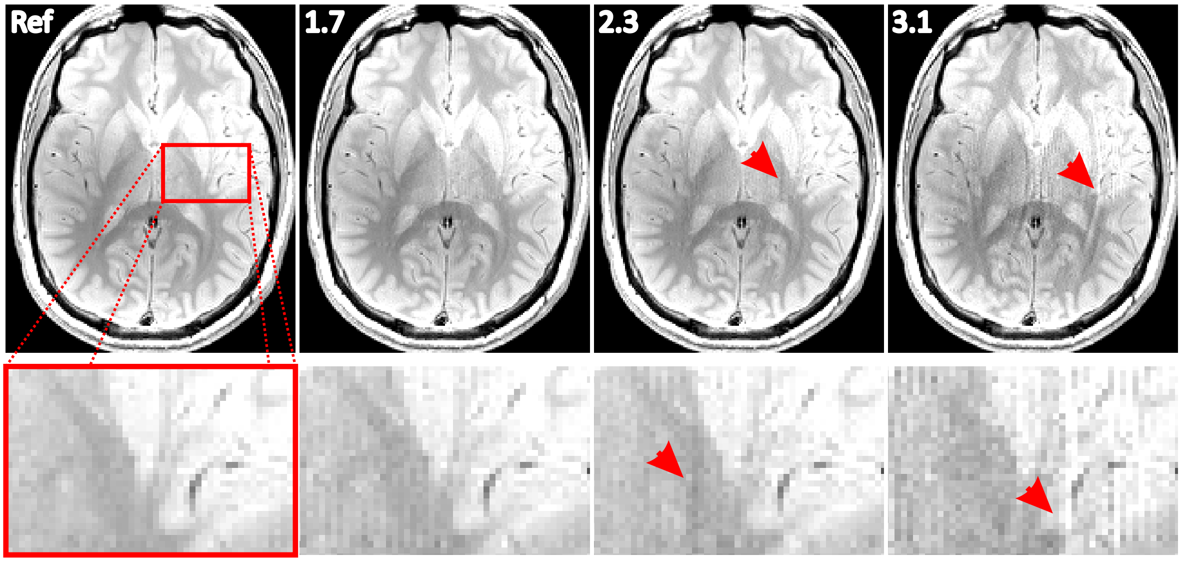

Figure 5.20: *Nonlinear inverse parallel imaging reconstructions. The images correspond to the first echo of a CPMG acquisition* (TE = 12.2 ms) *using a 32-element head coil. The fully sampled reference (Ref) is compared to reconstructions from undersampled data corresponding to net acceleration factors of 1.7, 2.3 and 3.1. At 2.3-fold acceleration, aliasing artifacts become visible in the result (arrows) which increase with higher undersampling.*

6

Model violations

From a linear system perspective, undersampling of k-space can result in an underdetermination of the minimization problem which increases the number of valid solutions for the reconstruction of the unknown image vector. The effect has been described in Section 3.1 for the linear inverse reconstruction of a single and independent image. The consequences for the reconstruction of two-fold undersampled numerical phantom data have been illustrated in Figure 3.2. In this example, the loss of spatial information allows for an arbitrary distribution of the original pixel intensity across two virtual object copies in image space.

The model-based T_2 reconstruction technique of the former section is based on the concept that uniqueness in image space may be restored by incorporating prior knowledge about sequence-specific data dependencies. For the investigated example of CPMG echo trains, the data dependence has been formulated in image space and comprises the assumption of a smooth and constant phase, as well as a mono-exponential decay of the real part of subsequent echo images. However, the experiments in Section 5.3.2 revealed that image regions violating the underlying model assumptions may still provoke reconstruction artifacts that occur most destructively for a regular sampling pattern with comb-shaped PSF. The following section demonstrates, why these artifacts do not necessarily indicate a failure of the optimization process but, in fact, often numerically solve the objective function better than the aspired visually optimal solution.

6.1 Multi-exponential signal decay

One source of model violations stems from partial volume effects that have to be expected in almost every real MRI dataset with finite resolution. A good description of the signal decay in respective regions would require a superimposition of multiple exponential curves, so that the applied mono-exponential model can only yield an approximation. In addition, Gibbs ringing may carry the effect of signal superimposition from structural borders to remote parts of the image. The following experiment demonstrates the isolated effect of signal superimposition in a dedicated phantom experiment and highlights the consequences for model-based reconstructions.

6.1.1 Materials and methods

A numerical pixel-based phantom was defined on a grid of 128 × 128 pixels, offering two compartments (C1 and C2) with different relaxation times. Simulated noiseless single-coil k-space samples were derived from the DFT of the pixels for 4 simulated echoes with an echo spacing of $\Delta t = 20\,\mathrm{ms}$. While the image-space signal of the first compartment follows an ideal mono-exponential decay:

$$S_{C1} = 0.5 \cdot \exp\left\{-t/(200\,\mathrm{ms})\right\},$$

the second compartment is described by two superimposed exponentials:

$$S_{C2} = 0.5 \cdot \exp\left\{-t/(200\,\mathrm{ms})\right\} + 0.5 \cdot \exp\left\{-t/(20\,\mathrm{ms})\right\}.$$

Spin-density and T_2 maps of the data were reconstructed with use of the MARTINI method (Chapter 5) by minimizing the cost function (3.6). The data was undersampled with an acceleration factor of 2 using both the interleaved scheme (depicted in Figure 5.4) and a regular comb-shaped pattern skipping every odd k-space line in every of the 4 echoes. The reconstructions from undersampled data were hereby initialized with the ideal solution from a reference reconstruction with full k-space coverage. The coil profiles were set to the identity for these studies.

6.1.2 Results

Figure 6.1 (left) shows the reconstructed parameter maps from fully sampled data. The results are identical to traditional pixel-wise fitting and exhibit a perfect reproduction of C1. The signal from C2 is “explained” by the mono-exponential least-squares solution:

$$\rho \approx 0.77,\ T_2 \approx 93\,\mathrm{ms}.$$

As this solution can only approximate the true data, the reconstruction terminates with residual energy in the cost function, i.e. $\Phi_{\mathrm{end}} > 0$.

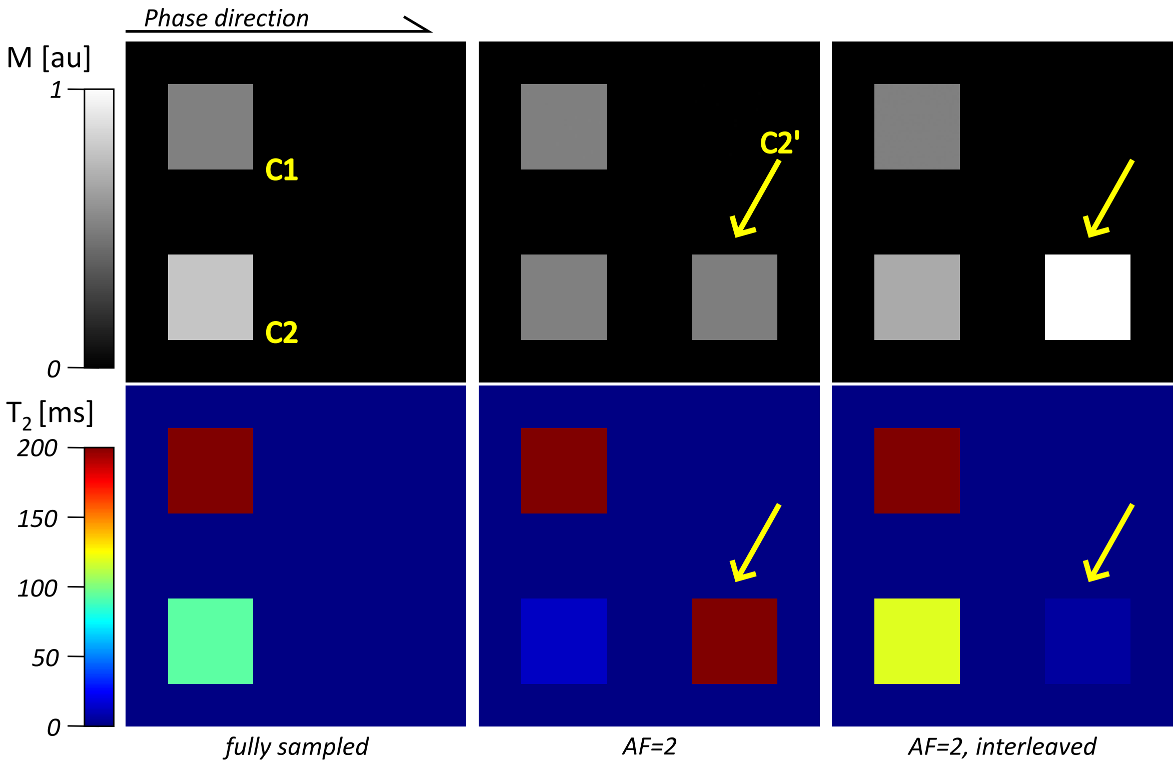

Figure 6.1: *Spin-density and T_2 maps of a pixel-based phantom with multi-exponential signal decay in compartment C2. MARTINI reconstructions have been performed on: Fully sampled data (left), two-fold equally undersampled data (center) and two-fold interleaved undersampled data (right). Undersampling gives rise to a virtual object C2' (arrows) that yields a better numerical model compliance than the visually optimal result (left).*

This situation changes when reconstructing the case, where only every even k-space line is sampled throughout all echoes. The result is illustrated in Figure 6.1 (center). Here, the aliasing effect allows for a perfect separation of C2 into its two exponentials, by creation of the virtual compartment C2' (arrows). The result yields a numerically perfect solution with a final cost-function value of $\Phi_{\text{end}} \approx 0$. Due to the optimal initialization, C1 remains aliasing free in this example, even though the same final cost-function value could also be achieved with an infinite amount of aliased solutions for C1.

The result for an interleaved sampling scheme is shown in Figure 6.1 (right). C1 is again reconstructed perfectly. A separation of C2 in its original components is precluded, as it would conflict with the available samples of the second echo. However, the aliasing effect still allows for the generation of a virtual compartment C2' with $T_2 << 2/5\,\Delta\,\text{TE}$. The reconstructed values after 200 iterations are

$$\text{C2} : \rho = 0.66,\ T_2 = 118\,\text{ms}$$
$$\text{C2'} : \rho = 2.32,\ T_2 = 6\,\text{ms}.$$

The respective time signals are illustrated in Figure 6.2. As can be seen, the superimposition (red curve) fits much better to the acquired echo time points than the

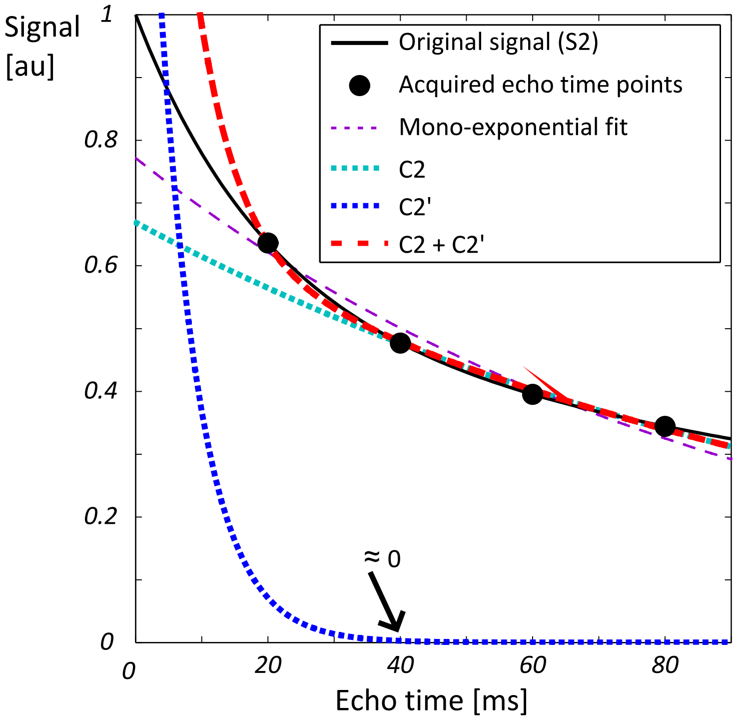

Figure 6.2: *Time-curve illustration of the reconstruction result for C2 for two-fold interleaved undersampling (same as in Figure 6.1, right). The superimposition of the two exponential decays C2 and C2' (red curve) fits better to the echo time points than the mono-exponential solution (purple curve).*

mono-exponential solution (purple curve). Still the signal of C2' does not interfere with the k-space samples of the second echo due to its rapid decay (blue curve).

6.1.3 Discussion

The example highlights an inherent problem of the MARTINI reconstruction and explains the necessity of sampling schemes with less destructive PSFs. Alternatively, more accurate model formulations or additional regularization terms may be used to counter the depicted effects. For example, the artifacts in reconstructions of simplified artificial phantoms as shown in Figure 6.1 could probably be suppressed by a regularization term that penalizes all T_2 values below a suitable threshold. However, in true objects the most destructive artifacts are usually superimposed by regions with other valid T_2 values that would spoil such a simple threshold approach.

Multi-exponential model

To account for the effect of multi-exponential signal behavior, it is conceivable to extend the model-function (6.1) by additional relaxation terms. For example, several model-based reconstruction experiments have been performed using the "bi-exponential" model:

$$M_{\mathrm{TE}}(\rho_1, \rho_1, R_1, R_2) = \rho_1 \cdot e^{-R_1 \cdot \mathrm{TE}} + \rho_2 \cdot e^{-R_2 \cdot \mathrm{TE}}. \tag{6.1}$$

However, without additional constraints, the inversion becomes even more underdetermined. For example, a mono-exponentially decaying image-space signal with

$$M_{\text{ideal}} = \rho \cdot e^{-R \cdot t} \tag{6.2}$$

can be reconstructed with the parameters

$$\begin{aligned} \rho_1 &= \rho - e, \quad & R_1 &= R \\ \rho_2 &= e \quad\quad\;\, , \quad & R_2 &= R \end{aligned}$$

for any arbitrary error e. For fully sampled data, high values of e can be precluded by simple regularization strategies, for example by penalizing the l^2 norm of ρ_2 during reconstruction. When undersampling, however, this can again lead to a situation where the physically correct result is numerically less attractive than an artifact-affected solution.

While in some experiments the reconstruction quality seemed to slightly benefit from the extended model, the approach also enhanced the noise in the reconstructed maps. Because a general preclusion of aliasing artifacts could not be achieved with the bi-exponential extension, the method has been discarded.

6.2 Image phase alternations

Another implicit assumption of the MARTINI reconstruction is that the phase of the complex-valued spin-density map in Equation (3.6) is both smooth and constant throughout the echo train. While this is approximately true for static objects, unavoidable motion in in-vivo experiments can cause periodic phase alternations in the acquired spin echoes [98]. For cooperative subjects in human brain MRI studies, the effect is usually restricted to regions with increased blood flow. On the other hand, for animal MRI studies at high magnetic field strength, phase imperfections have been observed to cause severe artifacts in reconstructions from undersampled data. The origin of these artifacts is analyzed in the following section and their impact demonstrated on reconstructions from undersampled high-field animal MRI data.

6.2.1 Materials and methods

Data simulation

To demonstrate the isolated effect of periodic phase perturbations, a numerical pixel-based phantom has been defined on a discrete grid of 128×128 pixels, offering a single compartment with $\rho = 1$, $T_2 = 100\,\mathrm{ms}$ and an alternating phase of $\varphi = \pm 50°$ for successive echo images. Simulated noiseless single coil k-space samples were derived from the DFT of the pixels. The data comprised 16 echoes with an echo spacing of $\Delta t = 6.72\,\mathrm{ms}$.

High-field animal MRI

A healthy female adult C57BL/6 mouse was anesthetized by isoflurane ($1.75\,\%$ in ambient air) via an endotracheal tube. A 3D dataset was obtained using a standard CPMG sequence (parameters in Table 6.1). An artificial second dataset with constant phase throughout the echo train has been created from the DFT of magnitude images multiplied with the phase image of the first echo. The magnitude representation of the first echo from a selected partition of the data is illustrated in Figure 6.3 (left). Figure 6.3 (right) depicts the image-space phase evolution over time for a selected ROI within the brain tissue (blue region) as well as a pixel within an inferior cerebral vein (arrow). The amplitude of phase perturbations within the vein (red curve) is approximately a factor of 10 higher than in the ROI (blue curve).

Reconstruction

Spin-density and T_2 maps for the phantom and the animal MRI data were reconstructed using the MARTINI method from Section 5.2.3, where the cost function has been extended by an unknown phase map $\boldsymbol{\varphi}$. Interleaved and blocked sampling schemes (Figure 5.4) for different AF were compared by selecting respective k-space lines from

Scanner hardware	
field strength	9.4 T
manufacturer	Bruker BioSpin, Ettlingen, Germany
system	BioSpec 94/30
coil	4-channel phased-array mouse head coil
Sequence	
method	MSME
NE	16
Δt	6.72 ms
resolution	$160 \times 160 \times 160\,\mu\text{m}^3$
matrix	$128 \times 86 \times 64$
TR	1200 ms
scan time	1:50:4 h

Table 6.1: *Experimental parameters used for high-field MRI of mouse brain in-vivo.*

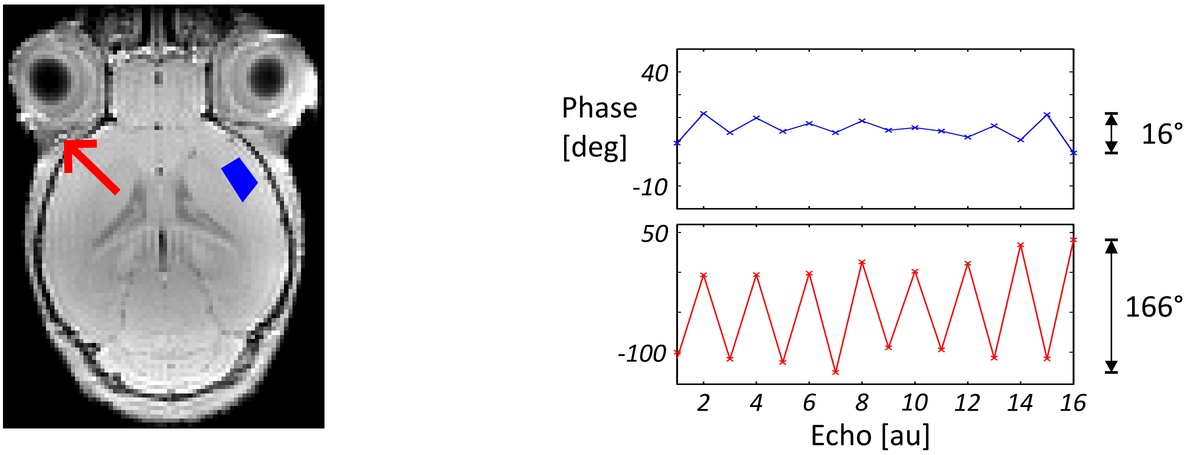

Figure 6.3: *(Left) RSS reconstruction of the first echo from a selected horizontal partition of a 3D high-field animal MRI. (Right) Phase evolution over the echo time in (red arrow) an inferior cerebral vein and (blue ROI) a region within brain tissue.*

the fully sampled data. While the coil profiles for the animal MRI data have been estimated as described in Section 5.2.2, the profiles were set to the identity for the phantom studies.

6.2.2 Results

Figure 6.4 (a) shows the reconstructed spin-density map from fully sampled simulated phantom data. The results are similar to the reconstruction of simulated samples from the DFT of the real part of the original images. As the alternating phase cannot be reproduced by the model, the optimization terminates with residual energy in the cost function, i.e. $\Phi_{end} > 0$.

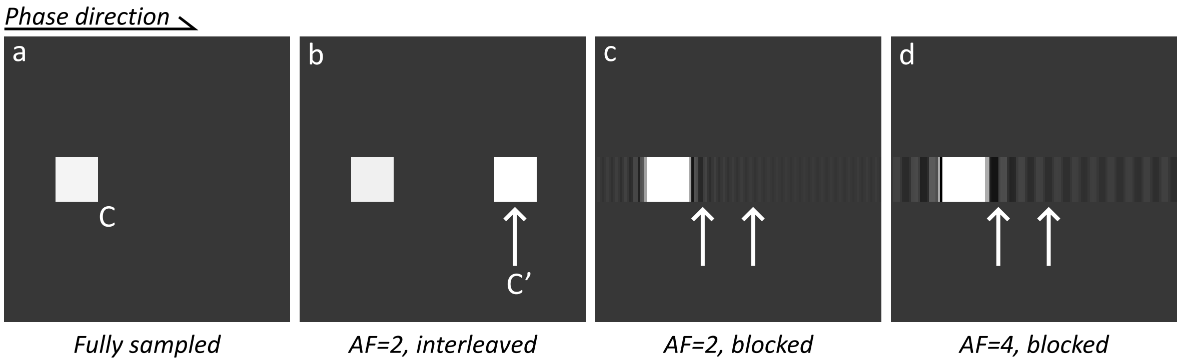

Figure 6.4: *Spin-density maps from a pixel-based phantom with alternating image-space phase. MARTINI reconstruction has been performed for fully sampled data (a) as well as for two-fold interleaved (b), two-fold blocked (c), and four-fold blocked undersampling (d). The artifacts (white arrows) in (b-c) yield better numerical model compliance than the visually optimal result (a).*

Figure 6.4 (b) demonstrates a phantom reconstruction for interleaved undersampling with an acceleration factor of 2. Here, the even AF causes all odd k-space lines to be sampled from echoes with negative compartment phase and all even lines from echoes with positive compartment phase. As a consequence, all available samples can be perfectly modeled by the DFT of a mono-exponentially decaying object ($\rho = 1$, $T_2 = 100\,\text{ms}$) with the odd and even k-space lines multiplied by the respective phase values. The according image-space representation yields the original object convolved with the inverse FT of the multiplicative k-space phase pattern which causes the appearance of C' in Figure 6.4 (b). As C' does not interfere with other image content, the result again poses a numerically perfect solution with a final cost-function value of $\Phi_{end} \approx 0$.

The ideal agreement of an artifact-affected result with the samples can be precluded with an odd AF. However, for strong phase deviations ($\Delta\varphi >> 20°$), the optimization still tends to yield artifacts in the solutions that support the minimization of the residual energy from the first echoes. Similar observations can be made with the blocked sampling scheme, even though the impact of the artifacts is considerably reduced due to the sinc-shaped PSF of the pattern (Figure 6.4, c and d).

The simulations highlight the general effect of phase alternations on the reconstruction approach and explain how artifacts, shaped by the PSF of the sampling pattern, can support the minimization of the cost function. Objects in true MR images are often embedded in a non-void surrounding and the multiplicative phase in k-space is neither scalar nor alternating with constant amplitude. Still, for undersampled data, regions with strong phase alternation as in Figure 6.3 (red arrow) can cause artifacts in the reconstruction (Figure 6.5, center) that usually solve the cost function better than the visual optimum from fully sampled data (Figure 6.5, left). The artifacts disappear when reconstructing from artificial samples with constant image-space phase throughout the echo train (Figure 6.5, right).

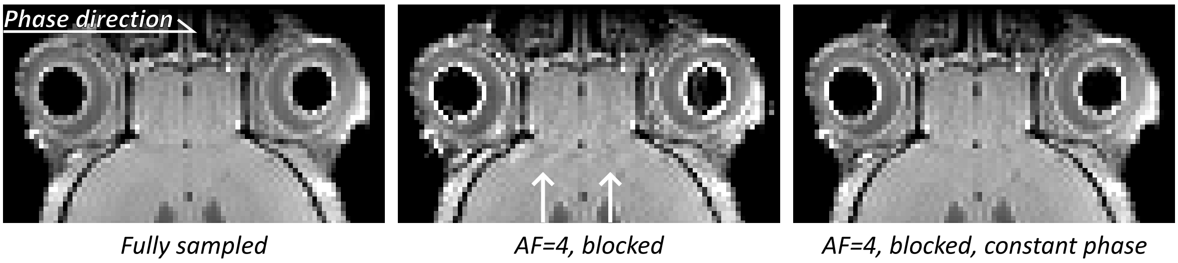

Figure 6.5: *Spin-density maps from a horizontal partition of a 3D animal MRI. Model-based reconstruction has been performed for fully sampled data (left) as well as for 4-fold blocked undersampling (center and right). The reconstruction in (center) exhibits artifacts (white arrows) originating from the phase perturbations in the inferior cerebral veins (see Figure 6.3). In (right) the originally alternating image-space phase of the data has been artificially substituted by the phase map of the first echo, and kept constant throughout the echo train.*

6.2.3 Discussion

The effect of phase estimation on the reconstruction

In principle, accounting for the phase map $\boldsymbol{\varphi}$ allows for the reconstruction of the correct magnitude values of objects that are not perfectly real, but have a constant phase value that differs from zero. On the other hand, not accounting for $\boldsymbol{\varphi}$ is equivalent to reconstructing only the real part of all objects in $\boldsymbol{\rho}$. For the simulations in the former section, the image-space phase of the phantom was designed to be alternating with equal positive and negative distance to the mean value of zero. The PSF of this pattern yields two weighted Kronecker δ spikes with phase values of 0° and 90°. Accordingly, the reconstructed object C in Figure 6.4 (b) is pure real, while C' is pure imaginary. For this specific phantom, the virtual compartment C' therefore does not show up on a reconstruction that does not account for an image phase map $\boldsymbol{\varphi}$ at all. However, the situation changes when using other sampling strategies or if the phase alternates around mean values other than zero. Also the phase modulation would usually show up in the coil profiles, when estimating the $\mathbf{C}_c$ from a composite k-space instead of assuming them to be 1 as in this artificial example.

In general, optimization of a single phase map $\boldsymbol{\varphi}$ during the reconstruction is expected to mainly yield advantages for small objects with constant local nonzero phase that is not accounted for in the smooth coil profiles. However, these theoretical advantages seem to be of limited use in practice.

For phase modulations that vary over the echo train, the optimization of $\boldsymbol{\varphi}$ has admittedly been observed to support the numerical minimization of the residuum. However, a distinct gain of image quality in practical experiments could not be found.

Extended phase model

During this thesis, several model extensions have been tested to better account for image-space phase variations throughout the echo train. For example, in many image-space regions the phase has been observed to be of a harmonically oscillating nature. Phantom simulations revealed that such phase can be reconstructed with the model-function:

$$M_n(\rho, \hat{R}, \phi_{mean}, \phi_{osc}) = \rho \cdot \hat{R}^n \cdot \exp\left\{i \cdot (\phi_{mean} + \phi_{osc} \cdot (-1)^n)\right\} \tag{6.3}$$

with the parameter maps $\phi_{mean}(\vec{r})$ and $\phi_{osc}(\vec{r})$ being treated as additional unknowns during reconstruction. However, even for simulated data and blocked sampling, the approach only works with odd acceleration factors. The finding indicates the essence of central k-space samples for correct phase estimations, which are only available from both oscillation periods when using odd AF. However, further examinations revealed that too many regions of true MRI scans cannot be approximated with this simple approach. An example is already given in Figure 6.3 (blue curve), where the periodicity of the phase evolution is swapped in echo number 12.

According to the results in [98], a correct image-space phase modeling for moving objects might require estimation of the actual acceleration and velocity of the entities. This is, however, beyond the scope of this work.

A more practical approach might also be the estimation of individual phase maps for every echo and penalization of the individual map's difference to a mean-phase map from composite k-space data. However, preliminary experiments with respective model implementations did not show a considerable improvement when using the blocked sampling scheme. Still, the approach might be more successful for radial sampling strategies, as those offer central k-space coverage in every echo.

6.3 A note on accelerated high-field animal MRI

In comparison to most human MRI applications, a major limitation in MRI of rodents is the usually much lower SNR. At the beginning of this thesis, several parallel imaging methods have been evaluated on a Bruker BioSpec 94/30 system at 9.4 T to accelerate ongoing studies on rodents. The experiments revealed that the limitations for the experimental setup were usually not given by under-determination of the reconstruction but simply by the unbearable reduction of SNR when undersampling. In fact, for high-resolution scans, it is even common practice to increase the scan time above the classical limits to gain additional SNR from data averaging. The first step to accelerate respective scans would therefore be to simply dispense with averaging. Accordingly, high undersampling factors in animal studies are only reasonable for sequences with a substantial surplus in SNR. This surplus is commonly found in 3D acquisitions, where the same spins are excited much more often than during multislice 2D imaging. On the other hand, coil arrays with more than four elements are far less common in animal MRI than in state-of-the-art human MRI systems. The previously introduced model-based reconstruction method for T_2 mapping therefore seems to be the perfect solution to overcome scan-time limitations in 3D spin-echo acquisitions of experimental animals.

During this work, a lot of effort has been put into the idea of transferring model-based T_2 reconstructions of human brain to rodents, in order to achieve otherwise infeasible 3D in-vivo acquisitions with full brain coverage and isotropic resolution below 100 μm. However, especially the aforementioned effects of alternating image-space phase have been found to cause severe problems in the practical adaption. In general, the effect of phase perturbations due to motion along magnetic field gradients increases with field strength, which might be a predominant difficulty at 9.4 T (or even higher fields). On the other hand, random magnifications of phase alternations have also been observed in scans of static objects, which might be due to an unresolved hardware issue of the specific system.

In some reconstructions of rodent brain, the origin of artifacts seemed restricted to regions with a high blood flow. An example has been shown in the previous section. However, several other scans also exhibited wave-shaped artifacts that globally modulated the intensity in all image regions. Due to the poor reproducibility, publication of the data has been postponed until further evaluations are finished.

7

Truncation and convolution errors

The results of the previous chapters highlight some general limitations of the model-based T_2-reconstruction technique at regions that do not comply with the underlying model assumptions. Especially, reconstructions from numerical phantoms in Section 5.3.2 revealed that even images with theoretically ideal model compliance cannot be recovered without artifacts when data is taken at sub-Nyquist rate from analytical k-space samples. In image space, all model violations for this idealized data can be explained with the limited resolution and the resulting partial-volume and Gibbs-ringing effects. In k-space, both effects are related to the truncation of high-frequency information when evaluating a limited number of discrete samples from an originally continuous function. Due to these effects, the visually optimal reconstruction result leaves residual energy in the implemented cost function, even for noiseless fully sampled data. This situation would be acceptable, if the corresponding results would at least minimize the numerical objective. However, the analysis in Chapter 6 demonstrates that this requirement is not necessarily met when reconstructing from undersampled data.

Some of the inherent errors in modeling k-space samples from a mono-exponential image-space model can be better understood when examining the model operations from a k-space perspective. A respective approach is demonstrated in the following section. Based on the findings, an alternative model formulation is proposed and evaluated, to counterbalance the effects of circular signal convolutions. Due to a temporary increase of elements in the vector of unknowns in k-space, the method is related to the framework of *super-resolution imaging* [99] [100]. However, the approach does not aim for an actual increase of resolution in the final result.

7.1 The effects of circular convolutions

7.1.1 Theory

As has already been highlighted in Section 5.2.4, the classical signal model for multiple spin-echo sequences is given by a mono-exponential relation, which can be simplified for equidistant echo spacing:

$$M_n(\rho, R) = \rho \cdot \underbrace{e^{-R \cdot \Delta t}}_{\hat{R}}{}^{\cdot n} \tag{7.1}$$

$$= \rho \cdot \hat{R}^n. \tag{7.2}$$

Hence, the image M_n at arbitrary echo number n can be calculated from the previous echo using the "inter-echo" relation:

$$M_n = M_{n-1} \cdot \hat{R}. \tag{7.3}$$

The convolution theorem allows for a transformation of this relation into k-space:

$$s_n(k) = s_{n-1}(k) * \hat{r}(k) \tag{7.4}$$

$$= \int_{-\infty}^{\infty} s_{n-1}(k)\ \hat{r}(k-\tau)\ d\tau, \tag{7.5}$$

where s_n is again the k-space signal at echo number n and $\hat{r}$ represents the Fourier transform of $\hat{R}$. The signal of the nth echo is therefore given by n successive convolutions of an initial signal s_0 with the k-space representation $\hat{r}$ of the unknown parameter map $\hat{R}$, which will be called *relaxivity kernel* in the following.

However, performing the multiplication of ρ and $\hat{R}$ on a discrete grid in image space and, thereon, applying the DFT on the result is equivalent to a *circular convolution* of the available N_s samples from the original signal and the kernel:

$$\tilde{s}_n[k] = [\Pi\ \mathrm{III}_{\Delta k}\ s_{n-1}(k)] * [\Pi\ \mathrm{III}_{\Delta k}\ \hat{r}(k)] \tag{7.6}$$

$$= \sum_{m=0}^{N_s-1} s_{n-1}[m] \cdot \hat{r}[k-m]. \tag{7.7}$$

Here, Π and $\mathrm{III}_{\Delta k}$ again represent the data acquisition window and the sampling comb as introduced in Section 4.1. As the original functions cannot be assumed to be periodic, Equation (7.7) inevitably differs from Equation (7.5). As the support of s and $\hat{r}$ is a priori unbounded, one source of errors results from truncated high-frequency information which cannot be accounted for. Another source of error can be expected from the energy in the sampled k-space regions which would usually be shifted into the truncated part during an unbounded convolution. This is because those regions get wrapped back into the sampled region when performing the respective circular operation. The procedure is illustrated in Figure 7.1 for the periodic self-convolution of a boxcar function.

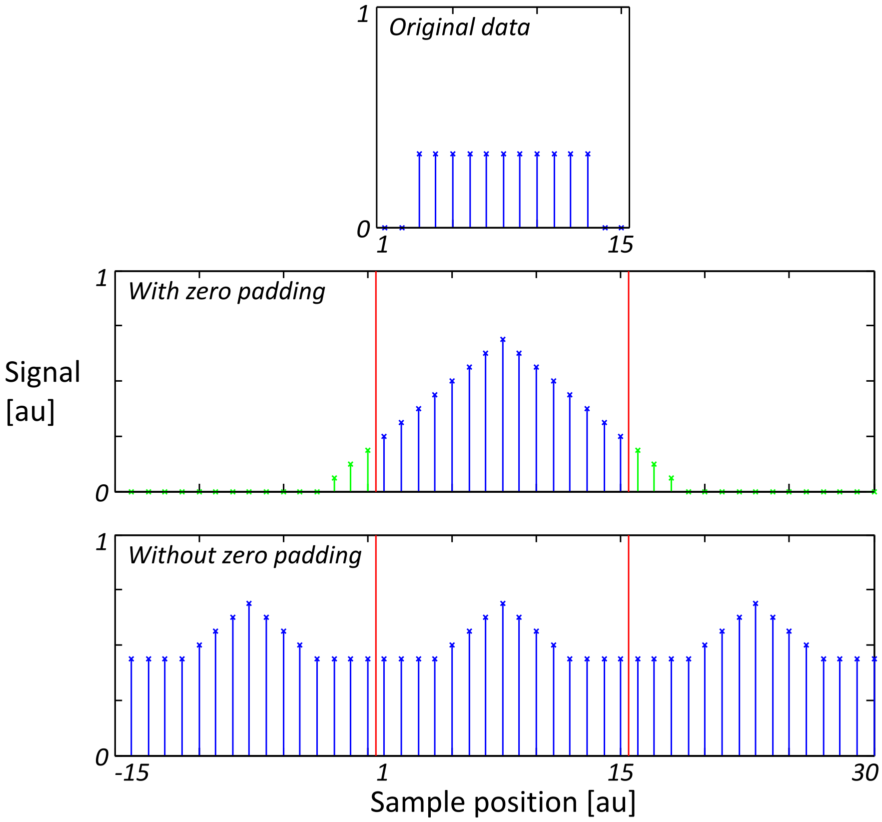

Figure 7.1: 15 samples of a boxcar function (top) are convolved with themselves using discrete circular self-convolution with (center) and without (bottom) two-fold zero padding of the initial vector prior convolution. The result at the borders of the original data support (samples 1 to 3 and 13 to 15) significantly differs between the two convolution strategies.

However, at least the wrapping effect can be avoided by zero padding both input functions prior to convolution.

It may be noted that the same systematic error is also inherent to most image-space based parallel imaging methods. The effect has been pointed out in [101]. However, the energy of true k-space data usually decreases with distance to the center. In practice, the data perturbation from a single convolution is therefore usually less pronounced than the one from the illustrated self-convolution in Figure 7.1. in particular, this is true for convolutions with the k-space representations of receiver coil sensitivities, as those have only few high-frequency components.

However, by repetitively evaluating Equation (7.7) for a series of subsequent spin echoes, the errors of every single convolution are carried forward to all following ones. Furthermore, the smoothness assumption from parallel imaging methods does not necessarily apply for the relaxivity kernel $\hat{r}$. The impact of respective convolution errors on model-based T_2 relaxometry will therefore be analyzed in more detail within the following section.

7.1.2 Materials and methods

Phantom extensions

As demonstrated in Section 4.3, analytical k-space samples of a numerical phantom can be created by superimposed primitives as sinc- or Bessel functions. For the following simulations, the phantom routines have been extended by analytical expressions for the relaxivity kernel $\hat{r}$. As a "neutral" image-space representation $\hat{R}$ of the relaxivity kernel $\hat{r}$ would be the identity, the respective simulated sample vector $\hat{\mathbf{r}}$ has hereby been initialized with a central Kronecker δ peak with amplitude N_s. The relaxivity of different compartments has then been accounted for by superimposed primitives of amplitudes $(\exp\{-\Delta t/T_{2,i}\} - 1)$, with $T_{2,i}$ being the T_2 value of the ith compartment.

Simulations

To simulate the influence of different convolution strategies, a one-dimensional analytical phantom with different relaxation values has been designed in k-space. Simulated k-space samples have been evaluated for different echo times TE. The most relevant parameters of the phantom are summarized in Table 7.1. An image-space representation, calculated by inverse DFT of the samples, is illustrated in Figure 7.2 for a subset of five different echo times.

NE	16	
Δt	10 ms	
samples	128	
	compartment	surrounding
ρ [au]	0.9	0.9
T_2 [ms]	80	200

Table 7.1: *Parameter of the one-dimensional analytical phantom used in Section 7.1.*

Samples and image-space representations of the original phantom data have been compared with respective model estimations by initializing Equation (7.7) with samples of the ideal $\hat{r}$ and s_0 and then successively evaluating the convolution operation for every echo. The simulations have been performed employing:

- Standard circular convolution
- Circular convolution using repetitive two-fold zero padding and subsequent zero-pad removal for every individual convolution (individual ZP).
- Circular convolution using initially two-fold zero-padded representations of $\mathbf{s}_0$ and $\hat{\mathbf{r}}$ without removal of the outer data between subsequent operations (global ZP).

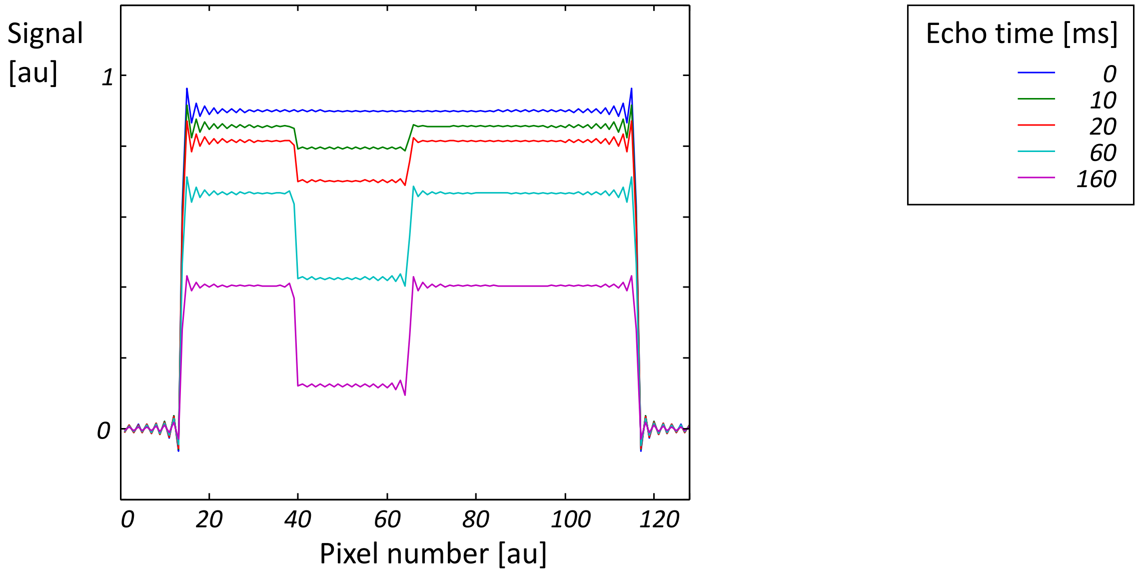

Figure 7.2: *Inverse DFT reconstruction of the signal intensity of the one-dimensional analytical relaxation phantom at different echo times.*

7.1.3 Results

Figure 7.3 depicts exemplary simulation results for the sixteenth echo in both k-space and image-space domain. The differences between original phantom samples and estimations derived from Equation (7.7) are plotted in the lowermost diagrams. The error in k-space accumulates at the outer k-space regions, i.e. in the high frequency components. In image space the strongest differences can be seen at object discontinuities, accordingly.

The l^2 norm of the error, which is identical in both domains, is plotted in Figure 7.4 (left) towards the different echo numbers. The plots represent the absolute errors with arbitrary units (top) as well as the error relative to the overall signal energy in the respective echo (bottom). As expected, the error increases with the number of convolutions involved.

The overall error in the selected central sampling window can significantly be decreased when evaluating phantom samples $\mathbf{s}$ and $\hat{\mathbf{r}}$ at higher resolution, i.e. by performing the convolutions on larger data vectors with an increased number of valid high-frequency samples. For example, when using 256 instead of 128 samples, the l^2 model deviation in the central 128 samples is decreased by about a factor of 5.

The effect of zero padding

Figure 7.4 (center) demonstrates the l^2 error evolution when performing two-fold zero padding of the data vectors prior to every convolution and again removing the outer samples afterwards. As can be seen, the accuracy of this strategy seems slightly superior for the chosen experimental conditions. However, the opposite is observed when evaluating the experiment with slightly altered sizes of the data vector. This rather

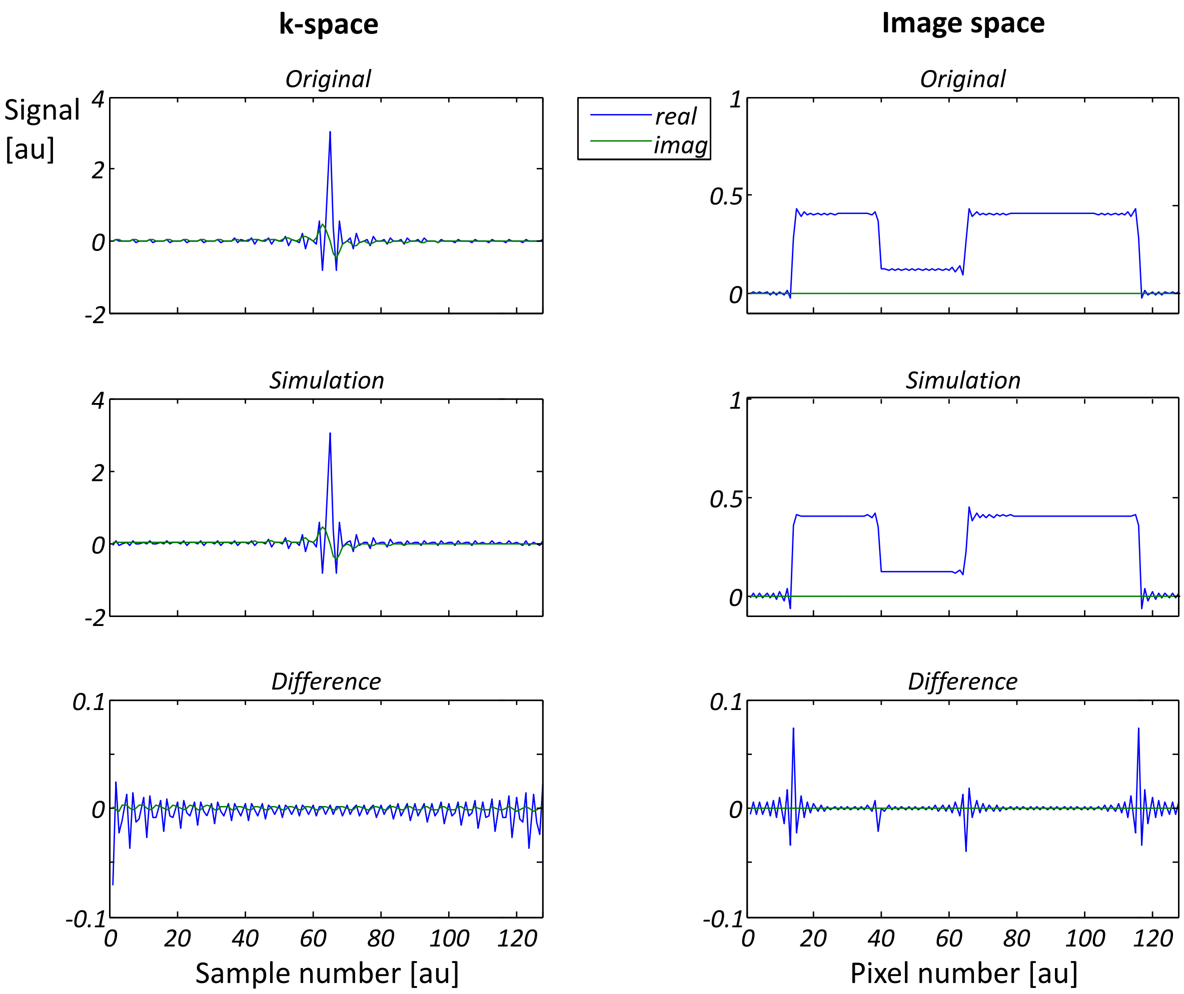

Figure 7.3: *(Left) k-space and (right) image-space representations of (top) the original samples of the simulated phantom at the 16th echo number and (center) emulation of the data by 15 subsequent convolutions of the spin-density signal with the ideal relaxivity kernel. The difference, i.e. the model error, is illustrated in (bottom).*

unexpected effect can be explained by inspecting the transitions between the repetitions of the involved sample vectors. An example is illustrated in Figure 7.5 for the threefold replicated data of a simple boxcar phantom, i.e. a single sinc function. In (top) the number of data samples approximately covers an even number of signal oscillation periods. As a consequence, the envelope of the data is smoothly continued between the repetitions. This smoothness is distinctively broken when changing the number of elements in the data vector by several samples as in Figure 7.5 (bottom).

The same effect can be observed for the k-space data of the phantom in Figure 7.2. Even though this data contains more versatile harmonics in k-space, it is still possible to recognize an oscillation of the envelope, which is more or less smoothly continued between repetitions when changing the vector size. The effect is directly related to either an accuracy gain or loss when performing zero-padded convolutions, as accumulated data repetitions with smooth transitions seem to yield a more accurate approximation of the original un-truncated data than the zero-filled alternative.

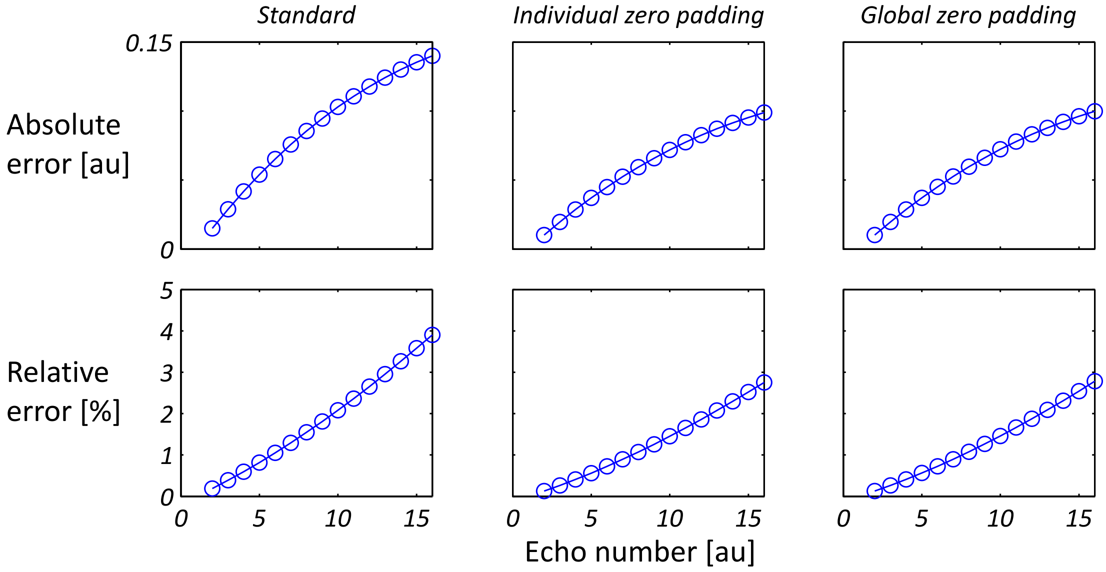

Figure 7.4: *(Top) l^2 norm of the overall deviation between original phantom data and the result from successive convolutions over the echo number. In (bottom) the error is standardized with the overall l^2 norm of the original data at the respective echo number.*

The effect becomes less pronounced with increasing complexity of the phantom. Especially for two-dimensional simulations, data modeling with zero-padded convolution usually performed slightly better than working on the original vector size. However, in general, the discrepancy between the accuracy of different convolution strategies depends on the phantom design and the number of samples in all performed simulations. Accordingly, a general advantage of zero-filled convolutions could not be confirmed.

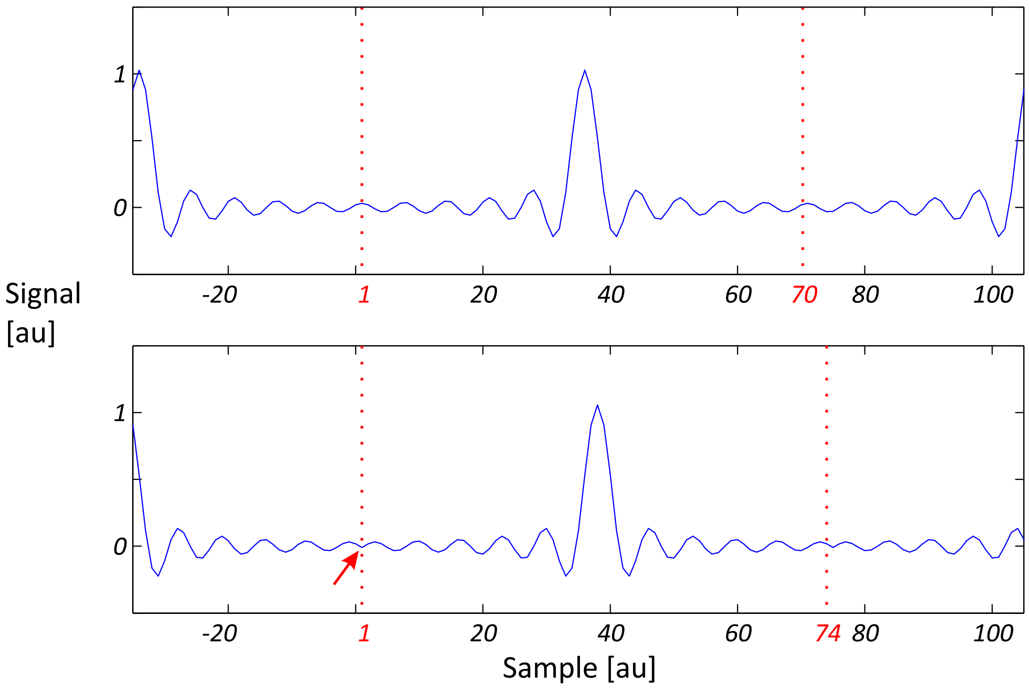

Figure 7.5: *Replication of the k-space samples from a* boxcar*-phantom for different numbers of available samples. In (top), replication of 70 samples yields a smooth transition. Due to the slight increase of the data-vector size from 70 to 74 samples, the smoothness is distinctively broken in (bottom).*

7.2 Model adaption

To achieve lower l^2 errors for ideal solutions from simulated data, the forward model for nonlinear inverse T_2 relaxometry has been reformulated. The theory of the new approach will be introduced in the following section. As the resulting method is formulated in k-space, it will be abbreviated k-MARTINI in the following.

7.2.1 Theory

As has been shown in Section 7.1.1, the k-space signal of the nth CPMG echo can be derived from the previous one by convolution with a relaxivity kernel $\hat{r}$. The data reconstruction problem can therefore be formulated as:

Find an unknown collection of data vector estimations $\hat{\mathbf{s}}_n$ *as well as a convolution kernel* $\hat{\mathbf{r}}$ *that comply with Equation (7.5) and have minimal difference to a set of given true data samples* $\mathbf{s}_n$ *selected by a an independent k-space trajectory* P_n *for every echo number* n.

Accordingly, a suitable solution can be found by minimizing the cost function

$$\begin{aligned}\Phi(x) &= \Phi_d(\hat{\mathbf{s}}_n) + \Phi_m(\hat{\mathbf{s}}_n, \hat{\mathbf{r}}) \qquad (7.8)\\ &= \underbrace{\frac{1}{2}\sum_{n=1}^{\mathrm{NE}} \|P_n\hat{\mathbf{s}}_n - \mathbf{s}_n\|_2^2}_{\text{Data-consistency term}} + \underbrace{\frac{\lambda_m}{2}\sum_{n=2}^{\mathrm{NE}} \|\hat{\mathbf{s}}_{n-1} * \hat{\mathbf{r}} - \hat{\mathbf{s}}_n\|_2^2}_{\text{Model-consistency term}}\end{aligned}$$

for the unknown parameters in

$$\mathbf{x} = \begin{pmatrix} \hat{\mathbf{s}}_1 \\ \vdots \\ \hat{\mathbf{s}}_N \\ \hat{\mathbf{r}} \end{pmatrix} . \tag{7.9}$$

The tuning factor λ_m allows for balancing the contributions of the data and the model-consistency components. The asterisk operation ($*$) can hereby be implemented as either a conventional or a zero-padded discrete convolution. More importantly, in contrast to the image-space based MARTINI formulation in Chapter 5, the vectors of unknowns $\hat{\mathbf{s}}_n$ and $\hat{\mathbf{r}}$ do not necessarily need to have the same size as the original data vectors $\mathbf{s}_n$ in this context. In fact, it is even possible to asymmetrically change the size and thus the degrees of freedom in the components of the vectors of unknowns, which allows for reconstructions of data and relaxivity estimates with unequal resolution. As will be demonstrated in the following, such an oversampling in parameter space can be beneficial to reduce artifacts when reconstructing from undersampled data.

7.2.2 Error distribution at the ideal estimate

Analogous to the simulations in Figure 7.4 it is possible to calculate the l^2 model-error distribution over subsequent echoes when evaluating Equation (7.8) for ideal estimates from simulated phantom data. The results for the one-dimensional phantom from Section 7.1 are depicted in Figure 7.6 for conventional and two-fold zero-padded circular convolution. The tuning factor λ has been set to 2 during the simulations, making the results comparable to the simulations in Figure 7.4. Because of the ideal initialization of the sample estimates $\hat{\mathbf{s}}$, all error components are contributed by the model-consistency term.

The preclusion of consecutive circular convolutions yields a considerably smaller error at the ideal solution, which does not accumulate with the echo number. While these simulations do not necessarily represent the error distribution for an actual reconstruction result, they demonstrate an improved compliance of the reformulated model with the analytically optimal result. The practical consequences on actual parameter reconstructions with the k-MARTINI approach are presented in the following.

7.2.3 Reconstruction algorithm

To evaluate the performance of the reformulated data model for reconstructions from undersampled data, the cost-function 7.8 and respective analytical gradients have been implemented in MATLAB. The required convolutions in Φ_m have been realized using the FFT algorithm, such that:

$$\hat{\mathbf{s}}_n * \hat{\mathbf{r}} = \mathrm{F}_{\mathrm{xy}}^{-1} \left[\mathrm{F}_{\mathrm{xy}}(\hat{\mathbf{s}}_n) \cdot \mathrm{F}_{\mathrm{xy}}(\hat{\mathbf{r}}) \right] , \tag{7.10}$$

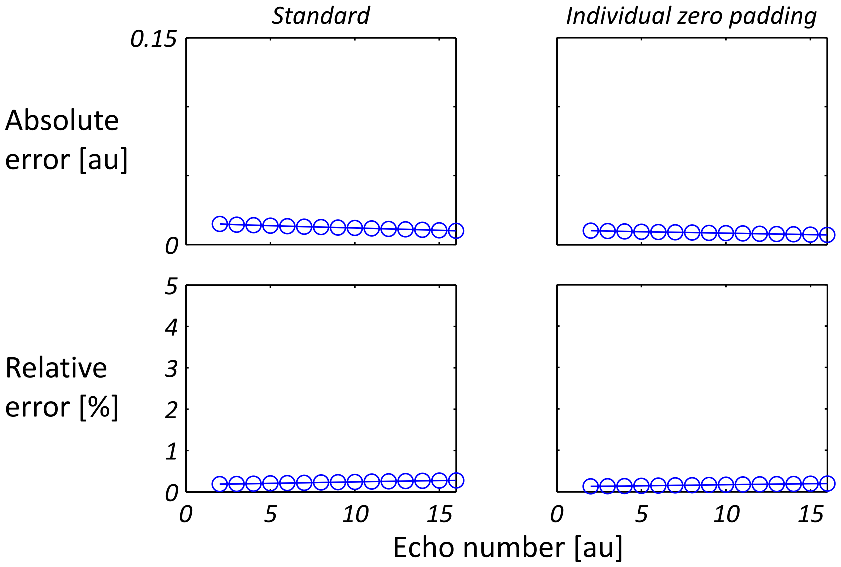

Figure 7.6: *Absolute and relative deviation between original phantom data and the result from convolution of the respective ideal previous echo with ideal relaxivity kernel. In (left), convolutions have been performed on the original grid. In (right) the involved vectors have been zero padded prior to each convolution. For comparability, the scaling of the axes is kept as in Figure 7.4.*

with $\mathrm{F_{xy}}$ and $\mathrm{F^{-1}_{xy}}$ being the 2D forward and inverse FFT. Again, for an aspired CG-Descent minimization to succeed, the partial derivatives of the model-consistency term have to be balanced by additional scaling variables $\mathbf{L}_s$ and $\mathbf{L}_r$. Optimization has then been performed on the transformed vector of unknowns

$$\tilde{\mathbf{x}} = \begin{pmatrix} \tilde{\mathbf{s}}_1 \\ \vdots \\ \tilde{\mathbf{s}}_N \\ \tilde{\mathbf{r}} \end{pmatrix}, \tag{7.11}$$

with

$$\hat{\mathbf{s}}_n = \mathbf{L}_s\ \tilde{\mathbf{s}}_n \tag{7.12}$$

$$\hat{\mathbf{r}} = \mathbf{L}_r\ \tilde{\mathbf{r}}. \tag{7.13}$$

For possible unequal dimensions of $\tilde{\mathbf{s}}_n$ and $\tilde{\mathbf{r}}$, the respective smaller vector is zero padded to the larger dimension by the operators E_s and E_r. Furthermore, for $\dim\{\tilde{\mathbf{r}}\} > \dim\{\tilde{\mathbf{s}}_n\}$ the zero padding is removed by the operator S_r after convolution. The full model-consistency term is therefore given by:

$$\Phi_m = \frac{\lambda_m}{2} \sum_{n=1}^{\mathrm{NE}-1} \| S_r\, \mathrm{F^{-1}_{xy}} \left[\mathrm{F_{xy}}(E_s\ \mathbf{L}_s\ \tilde{\mathbf{s}}_n) \cdot \mathrm{F_{xy}}(E_r\ \mathbf{L}_r\ \tilde{\mathbf{r}}) \right] - \mathbf{L}_s\ \tilde{\mathbf{s}}_{n+1} \|_2^2. \tag{7.14}$$

As the possible removal of zero padding in the data-consistency term is performed by the operator P, the formulation of Φ_d remains unchanged.

7.2.4 Gradient scaling

The cost function (7.8) is build up by a sum of two components. Accordingly, the gradient can be described as the sum:

$$\nabla\Phi = \nabla\Phi_d + \nabla\Phi_m. \tag{7.15}$$

Accounting for pre-scaling and oversampling operators, the implemented gradient for the data-consistency term is given by:

$$\nabla\Phi_d = \begin{pmatrix} \nabla_{\tilde{\mathbf{s}}_1} \\ \vdots \\ \nabla_{\tilde{\mathbf{s}}_N} \\ \nabla_{\tilde{\mathbf{r}}} \end{pmatrix} \Phi_d = \begin{pmatrix} \nabla_{\tilde{\mathbf{s}}_1} \\ \vdots \\ \nabla_{\tilde{\mathbf{s}}_N} \\ \mathbf{0} \end{pmatrix} \Phi_d, \tag{7.16}$$

where $\mathbf{0} = (0, 0, \ \dots\ , 0)$ represents a null vector with $\dim\{\mathbf{0}\} = \dim\{\tilde{\mathbf{r}}_n\}$. The gradient components with respect to the $\tilde{\mathbf{s}}_n$:

$$\nabla_{\tilde{\mathbf{s}}_n}\Phi_d = E_s\bar{\mathbf{L}}_s(P\mathbf{L}_s\tilde{\mathbf{s}}_n - \mathbf{s}_n) \tag{7.17}$$

are independent of the $\tilde{\mathbf{r}}$ and already uniformly scaled for arbitrary $\mathbf{L}_s$. However, in the gradient of the model consistency term

$$\nabla\Phi_m = \begin{pmatrix} \nabla_{\tilde{\mathbf{s}}_1} \\ \vdots \\ \nabla_{\tilde{\mathbf{s}}_N} \\ \nabla_{\tilde{\mathbf{r}}} \end{pmatrix} \Phi_m \tag{7.18}$$

the derivatives with respect to $\tilde{\mathbf{r}}$ and $\tilde{\mathbf{s}}_n$ again need to be balanced. This can be done using the previously introduced scaling matrices, which have been dimensioned according to the calculations in Appendix A.1. In the final implementation, the diagonal matrices $\mathbf{L}_s$ and $\mathbf{L}_r$ have again been reduced to scalar values.

7.2.5 Initial guess

Similar to the implementation in Section 5.2.5, an initial guess of the image-space vectors $\boldsymbol{\rho}$ and $\hat{\mathbf{R}}$ has been created from pixel-wise fitting of images from a composite k-space prior to the reconstruction process. The maps have been retrospectively filtered by a validity mask, removing all pixels ρ_i with $\rho_i < 0.1 \cdot \mathrm{mean}(\boldsymbol{\rho})$.

To dimension the scalar scaling, Equation (7.1) can again be used to create initial guesses for the $\mathbf{M}_n$ from the (artifact-affected) maps. Retrospectively, the mean of all the resulting (non-masked) pixels has been derived for $\hat{\mathbf{R}}$ as well as for each echo image in $\mathbf{M}_n$. The remaining NE +1 scalar values have then been used to derive the scalar scaling variables from Equations (A.30) and (A.31).

Coil profiles

To test the re-formulated relaxation model on true MRI data, it is again necessary to account for the complex-valued coil sensitivities of the different receiver-coil channels. Given the k-space coil-sensitivity representations $\hat{\mathbf{c}}_c$ of the coil elements c, the data-consistency term is extended to:

$$\Phi_d = \sum_{n=1}^{NE} \sum_{c=1}^{NC} \| P_n(\hat{\mathbf{c}}_c * \hat{\mathbf{s}}_n) - \mathbf{s}_{n,c} \|_2^2. \tag{7.19}$$

Similar to the approach in Section 5.2.2, the $\hat{\mathbf{c}}_c$ can be calculated in a pre-processing step from the combination of data from multiple echoes and zero padded to the dimensions of $\hat{\mathbf{s}}$.

7.2.6 Initialization

Similar to the implementation in Section 5.2.5, the unknown parameter map for the relaxivity kernel was initialized with the DFT of a uniform map of mean $\hat{\mathbf{r}}$-values from the initial guess. A good initialization for the $\hat{\mathbf{s}}_n$ appears to simply be the available samples in $\mathbf{s}_n$. However, this approach is only feasible for single-coil experiments, where $\hat{\mathbf{s}}_n$ and the (zero-padded) $\mathbf{s}_n$ have the same dimensions. To overcome respective limitations for multi-coil experiments, the initial guess was again exploited to estimate coil-combined images at different echo times. Even though those estimates are strongly affected by aliasing artifacts, initialization of the $\hat{\mathbf{s}}_n$ with the DFT of these images seems advantageous compared to initializing of the $\hat{\mathbf{s}}_n$ with zeros.

Even though all data samples were initially standardized by their overall l^2 norm, the success of the reconstruction remained dependent on a suitable choice of the tuning factor λ_m. For routine use, an automatic scaling of this variable would be essential. However, for the following proof-of-principle experiments we used heuristically chosen values instead. For the phantom studies, this resulted in $\lambda_m = 1$, for the later human brain MRI experiments, λ_m was set to 100.

7.2.7 Results

Comparison between k-MARTINI and (image-space) MARTINI

Figure 7.7 (ref) shows a reconstruction of the analytical T_2 map as well as T_2-weighted images at echo numbers 1 and 3 from a numerical phantom with the same design as in Section 5.3.2. The images have been derived from the inverse DFT of fully sampled simulated data. Respective results created with the MARTINI approach from Chapter 5 are illustrated in (a) for an undersampling factor of two. In order to visualize possible model improvements, sampling has been deliberately performed using the inferior interleaved sampling scheme (Figure 5.4), rather than the blocked sampling scheme. Also, for comparison to the k-MARTINI approach, the reconstructed spin-density map is not included in the illustration. Instead, snapshots for selected echo numbers have been calculated retrospectively from the reconstructed maps.

A corresponding reconstruction using the k-MARTINI without zero padding is depicted in Figure 7.7 (b). It can be seen that the method yields almost identical solutions for the T_2 map, exhibiting distinct aliasing artifacts from the compartment borders. However, a slight difference can be noticed in the calculated snapshots: While for MARTINI (a) artifacts are clearly visible for both illustrated echo images, the artifacts for k-MARTINI become almost invisible for the image of the third echo. In fact, artifacts for k-MARTINI could only be found in the four outermost echo numbers at $n = \{1, 2, 15, 16\}$. The MARTINI reconstruction, on the other hand, exhibits visible artifacts for all but the central echo image.

Figure 7.7 (c) shows respective results when using zero-padded convolutions. Apparently, the approach does not yield any visual improvements, despite the final cost-

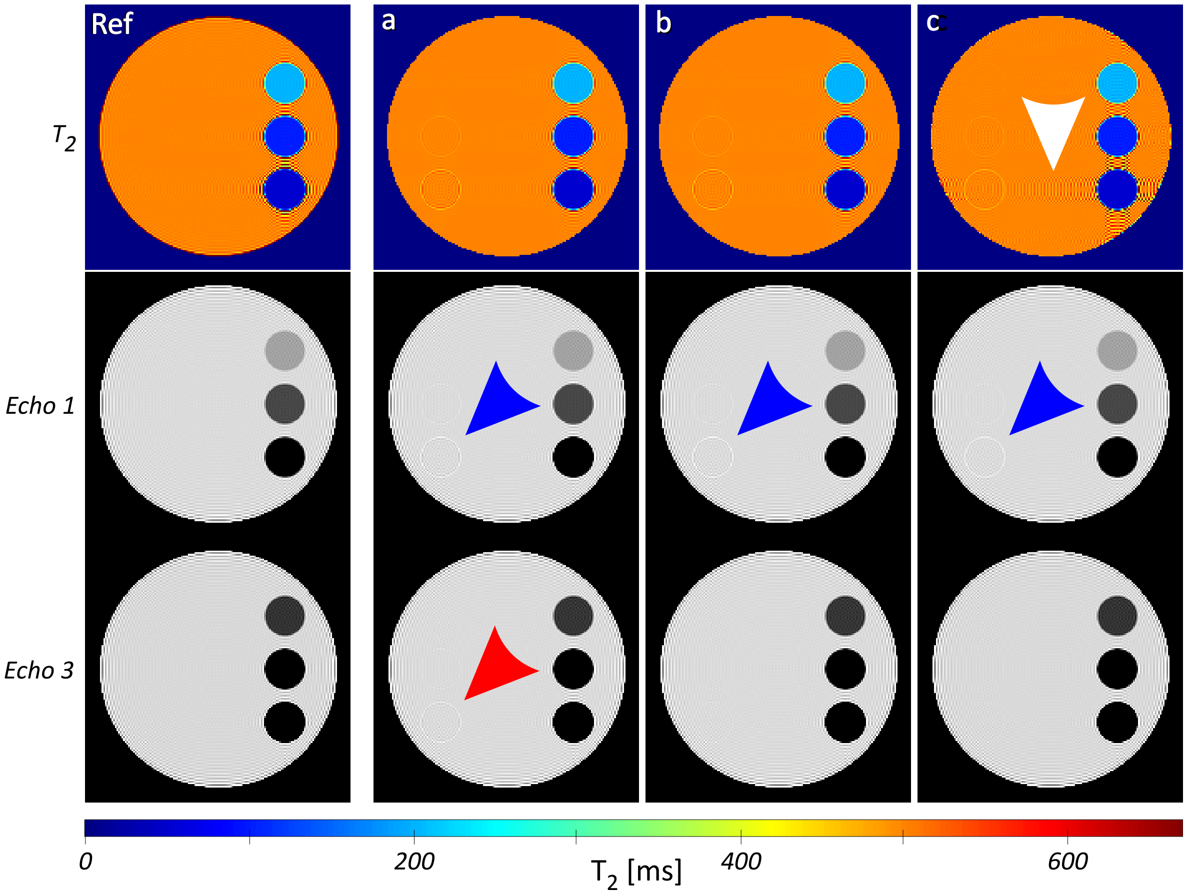

Figure 7.7: *T_2 maps as well as images of echoes 1 and 3 of an analytical phantom. The images in (Ref) represent the inverse DFT of the ideal analytical solution. (a - c) are reconstructions from 2-fold undersampled data using (a) the MARTINI method from Chapter 5, (b) the k-MARTINI approach on the original data-vector size and (c) k-MARTINI with zero padding prior to each convolution. While all reconstruction methods produce artifacts in the first echo (blue arrows), artifacts in echo 3 are only visible for the (standard) MARTINI method (red arrow).*

function value has decreased by a factor of approximately 0.5 compared to reconstructions with circular convolutions on the original vector size. In fact, the appearance of ringing artifacts is even more pronounced in the reconstructed T_2 map (white arrow). However, as will be demonstrated in the following, the qualitative reconstruction results do significantly change when increasing the number of elements in the vectors of unknowns.

Oversampling

The image in Figure 7.8 (a) shows the k-space representations for the reconstructed $\tilde{\mathbf{r}}$ when using k-MARTINI on the original data-vector size of 160 × 160 samples (200 CG iterations). For convenience, the final result has been retrospectively zero padded to a matrix of 2 × 2-fold the original size in this illustration. The actual analytical solution for $\hat{\mathbf{r}}$ on a 320 × 320 grid is shown in Figure 7.8 (d) for comparison. As highlighted by the red arrows, the most pronounced differences between both maps are located at the outer k-space regions as well as on the central horizontal and vertical axis.

The reconstruction result for a 2 × 2-fold increased size of $\tilde{\mathbf{r}}$ is demonstrated in Figure 7.8 (b). As can be seen, the algorithm excessively extrapolates the k-space data beyond the boundaries of the original central sampling window. Even though the overall result distinctively differs from the ideal solution, the center part complies better with the reference than the standard reconstruction in (a).

However, the best reconstruction results could be achieved by increasing the parameter space for all components in $\tilde{\mathbf{x}}$, i.e. for $\tilde{\mathbf{r}}$ as well as all components $\tilde{\mathbf{s}}_n$. The according reconstruction result for $\tilde{\mathbf{r}}$ is depicted in Figure 7.8 (c). Even though the original sampling window can still be distinguished from the extrapolated outer region, the l^2 difference in this window to the reference in (d) is again decreased.

Inverse discrete Fourier-transformation of the central k-space regions into image-space confirms these observations. Respective T_2 map and first-echo image reconstruc-

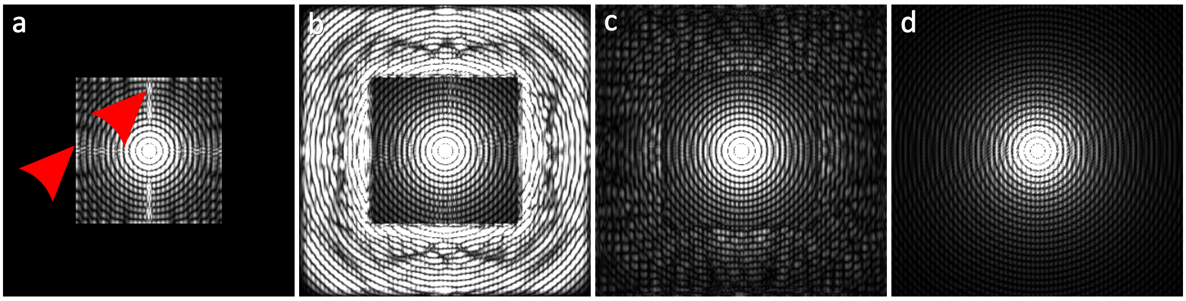

Figure 7.8: *(a-c) k-MARTINI reconstructions (magnitude representation) of the relaxivity kernel* $\hat{\mathbf{r}}$ *from two-fold undersampled data working on (a) the original sample-vector size, (b)* 2 × 2*-fold increased size of* $\tilde{\mathbf{r}}$*, (c)* 2 × 2*-fold increased size of both* $\tilde{\mathbf{r}}$ *and* $\tilde{\mathbf{s}}_n$*. The analytical ideal solution is illustrated in (d). The reconstruction in (a) has been retrospectively zero padded for convenience.*

tions are depicted in Figure 7.9. Compared to all previous reconstructions in Figure 7.7 (a - c), the appearance of aliasing artifacts (white arrows) is already less pronounced for an increased size of $\tilde{\mathbf{r}}$. However, as demonstrated in Figure 7.9 (b), the best reconstruction results for the phantom studies could be achieved by increasing the parameter space for both $\tilde{\mathbf{r}}$ as well as $\hat{\mathbf{s}}_n$. In this case, all visible aliasing artifacts completely vanished.

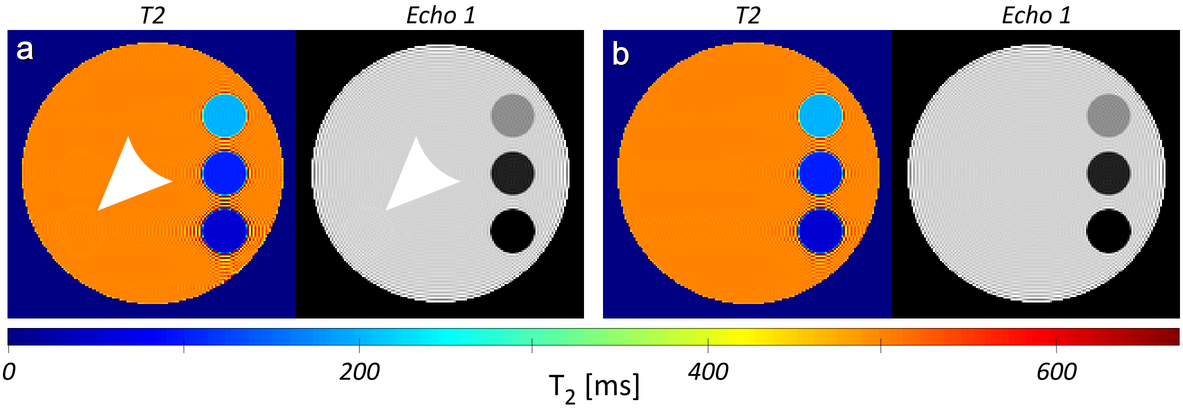

Figure 7.9: *k-MARTINI reconstructions of the T_2 map and first-echo image from two-fold undersampled analytical phantom data. Calculations have been performed on a 2×2-fold increased size of $\tilde{\mathbf{r}}$ (a) and 2×2-fold increased size of both $\tilde{\mathbf{r}}$ and $\tilde{\mathbf{s}}_n$ (b). The T_2 maps in (a, b) correspond to the inverse DFT of the central part of the images in Figure 7.8 (b, c).*

Different acceleration factors and sampling pattern

The reconstruction procedure has been evaluated for different acceleration factors and sampling patterns. For the given phantom and using interleaved sampling, the oversampled reconstruction produces excellent results up to an undersampling factor of 7 (Figure 7.10). While an AF of 8 is still possible when accepting small visible artifacts (arrow), the distortions become severe when increasing the AF even further.

Human brain MRI

The application of the k-MARTINI approach on human brain MRI is demonstrated in Figure 7.11. The data has been taken from echoes 2 to 17 of the scan in Section 5.3.6 and a single-channel receiver coil. The illustrated T_2 maps have been derived by minimizing the cost function (7.8) using the coil-profile extension (7.19), 200 CG iterations and 2×2-fold oversampling of the vectors of unknowns $\tilde{\mathbf{r}}$ and $\tilde{\mathbf{s}}_n$. The fully sampled reference (left) is compared to reconstructions from two-fold undersampled data using (top) the interleaved sampling scheme. The difference between both reconstructions is illustrated in (right). Unfortunately, the oversampling does not preclude the occurrence of undersampling artifacts in the reconstructed maps, even though the destructiveness of the effect can again be reduced with the use of a blocked sampling scheme (bottom).

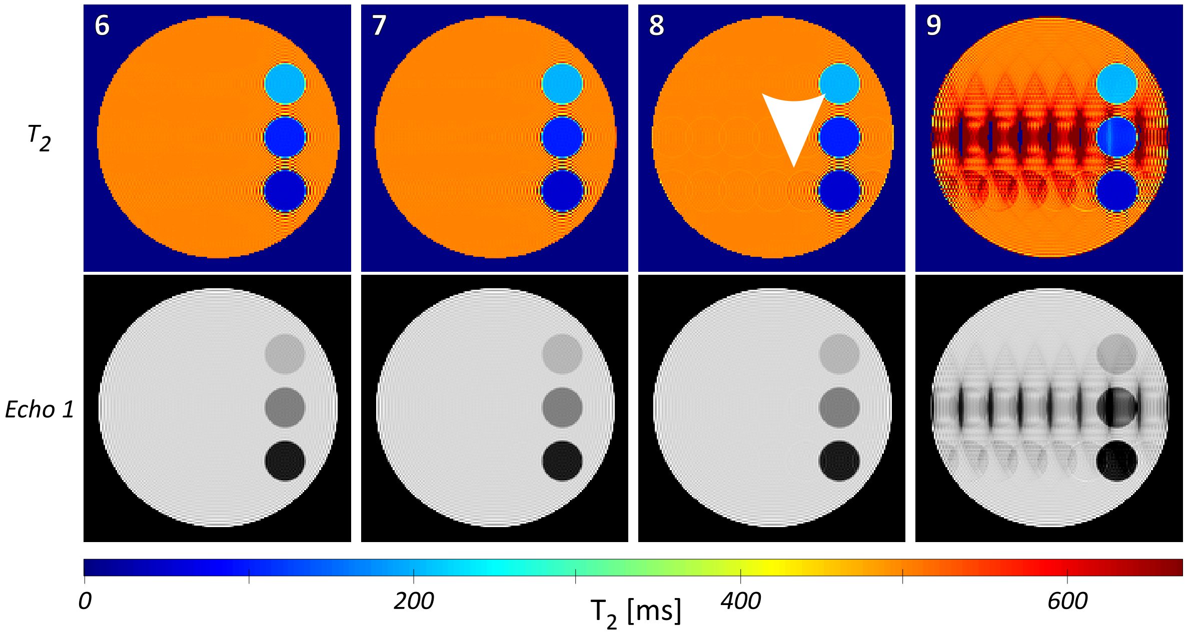

Figure 7.10: *k-MARTINI reconstructions of the T_2 map and first-echo image from 6-, 7-, 8-, and 9-fold undersampled analytical phantom data (interleaved scheme). Calculations have been performed on 2×2-fold increased size of both $\tilde{\mathbf{r}}$ and $\tilde{\mathbf{s}}_n$. At 8-fold undersampling, residual artifacts become visible in the T_2 map (arrow). The artifacts become severe for even higher undersampling factors.*

7.2.8 Discussion

In conclusion, the observations from phantom studies indicate that the wrap-around effect of circular convolutions in MARTINI reconstructions is less problematic than the general effect of missing high frequency information. The latter problem can be reduced by reconstructing oversampled data vectors. However, the increased degree of model freedom does not assure physically correct reconstruction of the missing high-frequency components and despite excellent reconstruction results in phantom studies, an improvement for reconstructions of human brain data could not be found. This may be due to the fact that signal deviations in true MRI data are not restricted to truncation errors. However, the excessive energy accumulation in the oversampled regions in Figure 7.8 (b) also indicates the necessity of additional constraints for the implicit data extrapolation. It is conceivable to create those constraints by incorporating prior knowledge about image properties in additional regularization terms. A promising example is the minimization of the total variation in image space [102]. However, as there is no generally accepted method for objectively choosing the inherent regularization parameters, this option is left for future extensions.

Parallel to this work, another interesting approach to exploit the multi-echo k-space-data relation (7.4) has been published by Senegas et al. [103]. Hereby, the relaxivity kernel is approximated from interleaved undersampled data in a pre-processing step. Similar to the SMASH approach in parallel imaging, the kernel is then kept constant

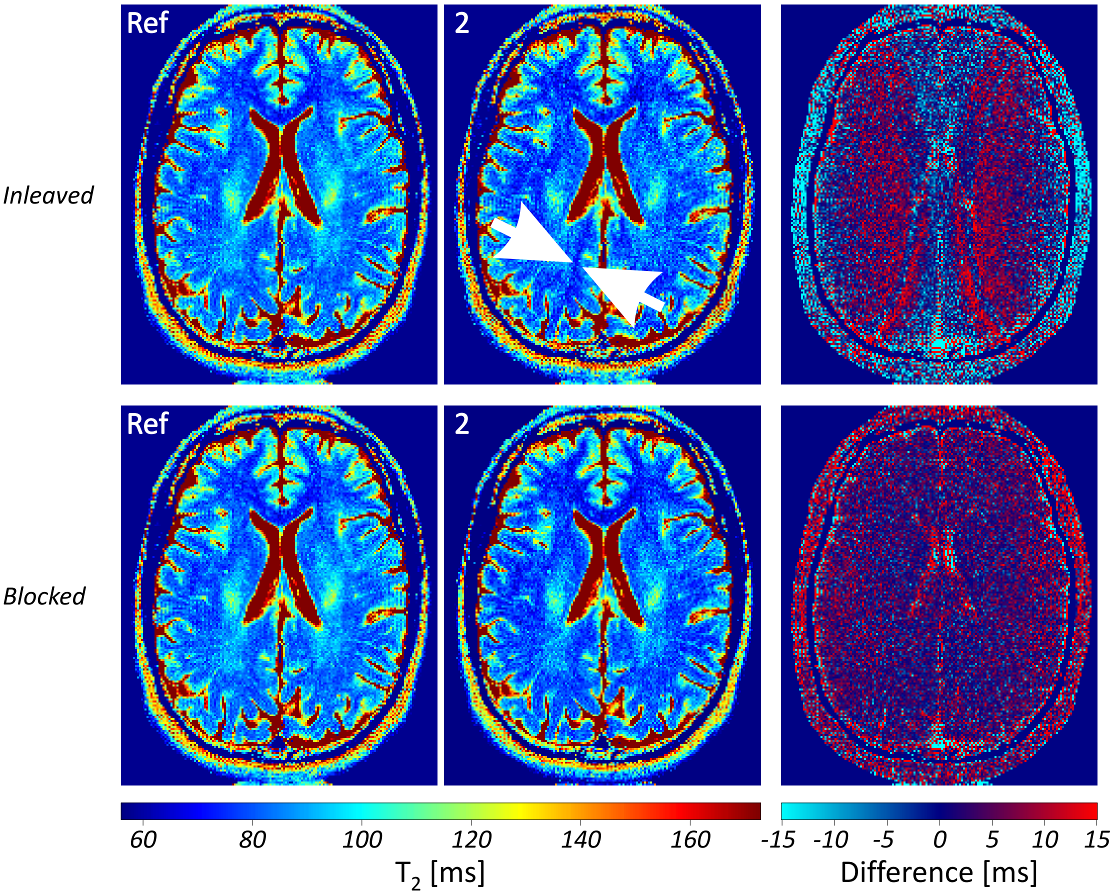

Figure 7.11: *k-MARTINI reconstructions of* T_2 *maps of the human brain with* 2×2*-fold oversampling of the vectors of unknowns* $\tilde{\mathbf{r}}$ *and* $\tilde{\mathbf{s}}_n$*. The fully sampled reference (left) is compared to reconstructions from two-fold undersampled data using (top) the interleaved and (bottom) the blocked sampling scheme. The difference maps (right) illustrate the remaining artifacts from undersampling.*

and used to fill the undersampled data lines in a second step. This linear method has the charm of being much faster than iterative nonlinear inversion approaches. However, as for the reconstructions in Chapter 5, model violations due to sequence imperfections or data truncation are ignored in the method.

8

Model-based T_2 relaxometry using the generating function formalism

In Section 5.1.1 the CPMG sequence has been introduced, which allows for the acquisition of a train of successively refocused echoes after a single excitation pulse. Most T_2 reconstruction methods in clinical practice rely on the assumption that samples from this echo train approximate the signal from multiple (single-) echo acquisitions at different echo times. However, as has already been outlined in Section 5.3.5, this assumption is violated due to various reasons. The most notable consequence is a hypointense first echo which disrupts the roughly mono-exponential signal decay of subsequent echo images. Due to this reason, several approaches have discarded the first echo, favoring improved fits [96, 97]. In fact, while often ignored in practice, most of the underlying physical reasons have already been studied in 1988 by Henning et al. [104, 105]. The primary cause has been found in the formation of stimulated and indirect echoes. By considering different magnetization pathways from pulse trains, a recursive method is introduced in [104] to reproduce the echo amplitudes in multiecho sequences for different refocusing flip angles. The method complements pioneering work by Woessner [92] and is sometimes referred to as the extended phase graph (EPG) algorithm. Complementary methods were elaborated in [106, 107]. However, all these approaches are recursive in origin and rather tedious to use as objective functions for signal fitting. In 2007 Lukzen et al. [108] managed to obtain an explicit analytical expression for modeling the CPMG signal decay by employing a mathematical tool known as the generating function formalism (GF) [109, 110]. The model has recently been further extended by Petrovic et al. to account for non-ideal slice profiles [111].

The following section deals with the application of the final signal model in [111] for accurate spin-density and T_2 reconstructions from undersampled Cartesian data. Its accuracy and susceptibility to noise is compared to reconstructions based on the previous mono-exponential attempts.

8.1 Theory

The GF for CPMG signal amplitudes has been found in the z-transform domain [108]:

$$G(z) = \frac{\rho}{2}\left(1 + \sqrt{\frac{(1+zk_2)[1-z(k_1+k_2)\cos\alpha + z^2 k_1 k_2]}{(-1+zk_2)[-1+z(k_1-k_2)\cos\alpha + z^2 k_1 k_2]}}\right), \tag{8.1}$$

where ρ is the spin density, $k_1 = \exp\{-\Delta t/T_1\}$ and $k_2 = \exp\{-\Delta t/T_2\}$ are the relaxation terms, α is the refocusing flip angle, Δt the inter-echo spacing and T_1 and T_2 the relaxation times. z denotes a complex variable in the z-domain. The nonuniform flip-angle distribution of non-ideal slice profiles can be accounted for by superimposing evaluations of Equation (8.1) for different values of α [111]. The final model formulation in z-domain is therefore given by:

$$G_{\mathrm{SP}}(z) = \frac{1}{Q}\sum_{i=1}^{Q} G(z, \alpha_i), \tag{8.2}$$

with α_i being a finite number of Q supporting points, characterizing the profile of the refocusing pulse in slice direction.

Evaluation of Equation (8.2) on the unit circle, i.e. for $z = \exp\{i\phi\}$, $\phi = 0 \ldots \pi$ and, thereon, applying a DFT in z-direction yields a discrete time signal corresponding to the echo amplitudes at echo times TE.

$$M_{\mathrm{TE}} = M_{n\cdot\Delta t} = \mathrm{F_z}\left[G_{\mathrm{SP}}(z)\right]. \tag{8.3}$$

Given a series of magnitude images from a CPMG echo-train, Equation (8.1) can be used as a model for pixel-wise fitting to estimate accurate T_2 values at different spatial image positions. The method has been evaluated in [111, 112] and its quantitative results compared with the gold standard, i.e. fitting exponential curves to a series of magnitude images acquired with the very time consuming (single-) spin-echo sequence. Hereby, the GF-fitting approach has proven to yield much more accurate and reproducible estimations when applied to CPMG data than respective mono-exponential fitting. Figure 8.1 demonstrates the performance of the GF fit on an exemplary pixel of a human brain CPMG scan (scan parameters in Table 8.3).

As a drawback relative to traditional fitting, evaluation of Equation (8.1) requires a valid T_1 and flip-angle map prior to T_2 reconstruction as well as an estimation of the pulse profile in slice direction.

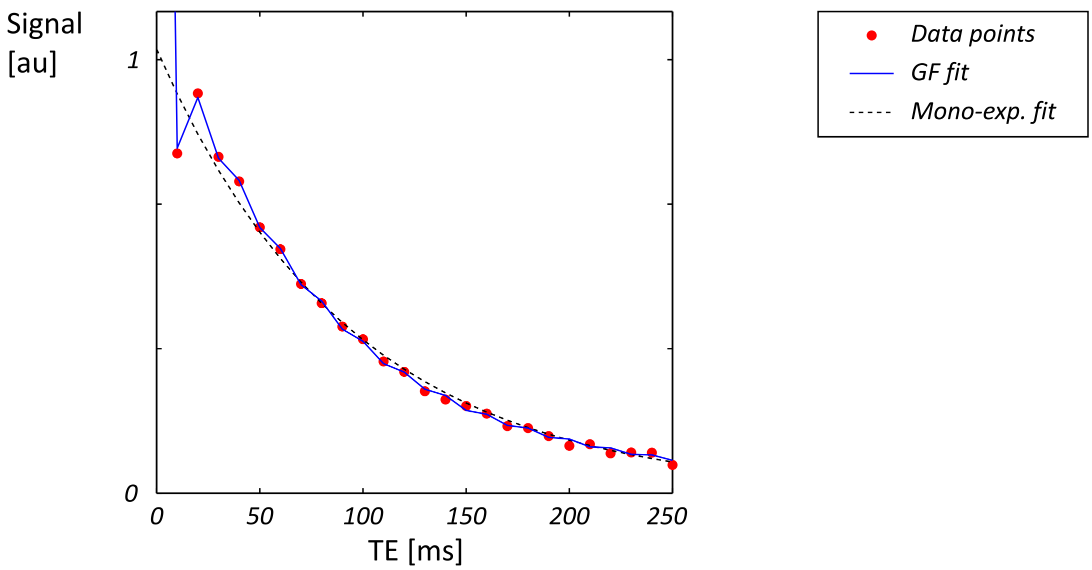

Figure 8.1: *Curve-fitting of the magnitude signal decay of a single pixel from a CPMG scan with 25 echoes (dots). Mono-exponential signal modeling (broken line) is compared to the GF model (solid line). As the GF function is only valid at the actual echo time points, the solid curve represents linear interpolations without physical validity.*

8.1.1 Aliasing in z-direction

As stated in Equation (8.3), evaluation of the GF on the unit circle in z-domain allows for the calculation of MSE amplitudes by application of a DFT. The range of echo times is inversely proportional to the frequency resolution, so that for N_z frequency samples the longest modeled echo time yields $\mathrm{TE}_{\mathrm{max}} = N_z \Delta t$. As a rule of thumb, $\mathrm{TE}_{\mathrm{max}}$ should be at least 5 times the longest T_2 within the measured object to ensure a proper coverage of the T_2 signal decay. If this requirement is violated, the modeled echo amplitudes (i.e., the DFT of the GF) become distorted due to aliasing in time direction. The effect is demonstrated in Figure 8.2 for the simulated signal of 16 echoes with $\Delta t = 12\,\mathrm{ms}$ under ideal experimental conditions, i.e. a homogeneous slice profile and a refocusing flip-angle of 180°. According to the model assumptions, evaluation of Equation (8.1) should yield the same result as simple mono-exponential modeling for this case. However, while this is approximately true for values of $T_2 < 40\,\mathrm{ms}$, strong deviations can be observed for larger T_2 values. The resulting signal overestimation is illustrated in Figure 8.2 (left) for an exemplary $T_2 = 120\,\mathrm{ms}$. The effect can be avoided by oversampling in z-direction, i.e. by evaluating Equation (8.1) at substantially more than NE z-points. For example, the curve in Figure 8.2 (right) demonstrates the result of the GF model for the same parameters as in (left) when oversampling by a factor of $\mathrm{OS} = 4$, i.e. evaluating Equation (8.2) at 64 points in z-domain. The result for the higher number of z-points is again in excellent compliance with the result of the respective mono-exponential curve. However, larger T_2 values may require even more aggressive oversampling to be accurately modeled by this approach.

Unfortunately, excessive data oversampling can yield unpleasantly high computational costs. This becomes particularly problematic for iterative reconstruction methods that require repetitive evaluations of the underlying model functions. On the other hand, the precise determination of tissue T_2 values with more than 100 ms has only limited relevance in clinical practice. For traditional pixel-wise fitting it may therefore be reasonable to choose an oversampling of $\mathrm{OS} = 4$ to 8 and limit implausibly large T_2 values by a validity mask.

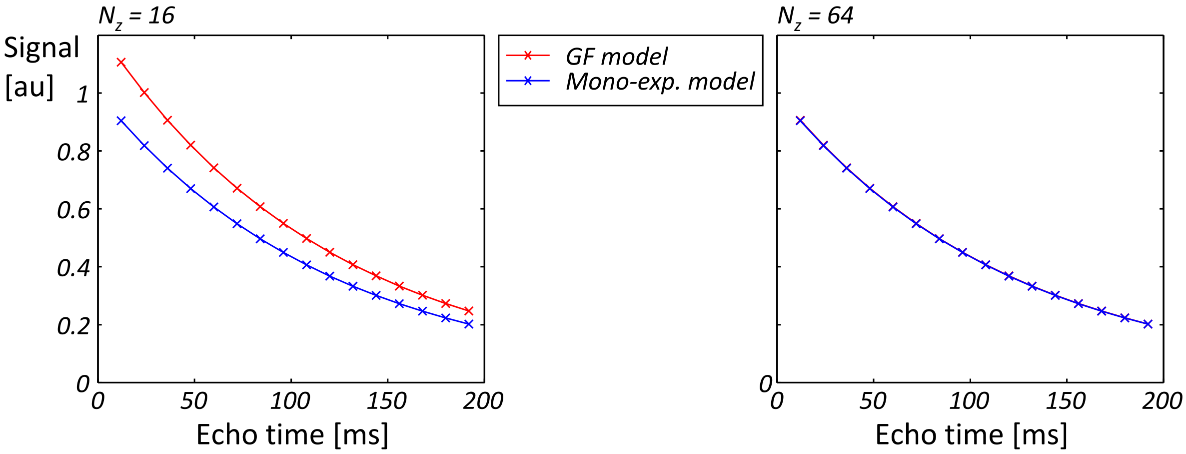

Figure 8.2: *Simulated CPMG signal amplitude decay of an object with* $T_2 = 120\,\mathrm{ms}$ *and assuming an ideal refocusing pulse. The correct mono-exponential curve is compared to the result from GF modeling without (left) and with 4-fold oversampling in* z*-domain (right).*

8.1.2 Reconstruction from undersampled data

Analogous to Equation (5.4), the GF model can be extended by additional DFT operators to create estimated k-space samples from a set of parameters combined in a vector of unknowns $\mathbf{x}$:

$$\hat{\mathbf{s}}_{\mathrm{TE}} = \mathbf{P}\,\mathrm{F}_{\mathrm{xy}}\left\{\mathbf{C}_c\,\mathrm{F}_{\mathrm{z}}\left[G_{\mathrm{SP}}(\mathbf{x})\right]\right\} \tag{8.4}$$

$$\mathbf{x} = \begin{pmatrix} \boldsymbol{\rho} \\ \mathbf{k}_2 \end{pmatrix}. \tag{8.5}$$

As in the former sections, $\mathbf{P}$ denotes the sampling pattern, F_{z} is a one-dimensional DFT in z-direction, F_{xy} the DFT in the two spatial directions and $\mathbf{C}_c$ the complex coil sensitivities of the coil elements c. Aiming for the reconstruction of parameter maps from undersampled data, the model is again embedded in a cost function which measures the difference between the modeled samples $\hat{\mathbf{s}}$ and the actually acquired samples $\mathbf{s}$ for all echo times TE:

$$\Phi(\mathbf{x}) = \frac{1}{2}\sum_{\mathrm{TE}}\sum_{c}\|\hat{\mathbf{s}}_{\mathrm{TE},c}(\mathbf{x}) - \mathbf{s}_{\mathrm{TE},c}\|_2^2. \tag{8.6}$$

Reconstruction of the parameter maps $\mathbf{T_2} = -\Delta t\,(\ln(\mathbf{k}_2))^{-1}$ and $\boldsymbol{\rho}$ by minimization of Equation (8.6) will be subject of the following sections. To distinguish the method from previous approaches, it will be abbreviated as gf-MARTINI.

8.1.3 Optimization and gradient scaling

The minimization of Equation (8.6) by means of the CG-Descent algorithm again requires the gradient of the objective function to be balanced with respect to its partial derivatives. Therefore, the vectors $\mathbf{k}_2$ and $\boldsymbol{\rho}$ in the GF model (8.1) have been substituted by scaled variants:

$$\tilde{\boldsymbol{\rho}} = \mathbf{L}_\rho^{-1}\, \boldsymbol{\rho} \tag{8.7}$$

$$\tilde{\mathbf{k}}_2 = \mathbf{L}_k^{-1}\, \mathbf{k}_2, \tag{8.8}$$

with $\mathbf{L}_\rho$ and $\mathbf{L}_k$ being diagonal scaling matrices. However, in contrast to former approaches in Sections 5.2.4 and 7.2.4, a robust method for an automatic dimensioning of the scaling has not yet been identified and involves several challenges. For example, we observed large T_2 values ($T_2 >> \mathrm{TE}_{\mathrm{max}}/5$) to provoke very strong gradient amplifications in few discrete regions. In contrast to traditional pixel-wise fitting, pixels with implausible signal behavior or long T_2 cannot simply be excluded from the reconstruction. As a consequence, respective regions sometimes lead to a global failure of the reconstruction process when using simple scalar values for the scaling. To prevent this effect, a dynamic validity mask has been implemented to detect potentially destructive pixels during the reconstruction and to reduce the gradient scaling at respective regions. As those regions are initially unknown for undersampled data, most of the following reconstructions were performed in a three-step approach with a fixed number of 3×200 CG-iterations. After each of the three optimization blocks, the validity mask was updated, dampening the gradient scaling by a factor of 10^{-5} at regions with an intermediate T_2 of either more than $\mathrm{TE}_{\mathrm{max}}/5$ or less than 0 ms. All negative intermediate T_2 values were also replaced by a selected maximum value of 1000 ms in the initial guess of the subsequent optimization block. For the following proof-of-principle study, the scaling was initialized with heuristically chosen scalar values of $L_\rho = 0.1$ and $L_k = 1$ and all data initially standardized by their overall l^2 norm.

As in Section 5.2.5, an additional pixel-wise fitting routine has been programmed employing the Matlab `nlinfit` program to fit the real part of the model (8.3) to the magnitude intensity decay in image space. In contrast to the CG-Descent optimization approach, the gradient has hereby been approximated using the internal finite-difference method rather than the explicit analytical expression.

8.2 Simulations

Using Equation (8.2) as a forward model, the GF approach can be exploited to simulate the effect of T_1, the slice profile and B_1 inhomogeneities on the estimated signal behavior. Respective analytical phantoms have been designed using the methods described in Section 4.3. The reconstruction performance of the nonlinear GF inversion will be demonstrated on a numerical phantom with the same spatial layout as in the sections 5.3.2 and 7.2.7. However, with respect to previously discovered limitations, the T_2 in the surrounding has been reduced to a more moderate value but also substantially increased within the topmost compartment. The pulse profile for the simulations was derived from a Gaussian using 16 support points. The T_1 values as well as the B_1 field were simulated to be constant throughout the FOV. The design specifications are summarized in Table 8.1.

To avoid aliasing effects in z-direction, the forward simulation of the data was evaluated at 1024 z-domain data points. Only the first 17 points were further used in time domain.

NE	17			
N_z	1024			
Δt	10 ms			
matrix	160 × 160			
T_1	1000 ms			
α	180 °			
slice profile	Gaussian, Q = 16			
compartment	bottom	center	top	surrounding
ρ [au]	1	1	1	1
T_2 [ms]	50	100	800	75

Table 8.1: *Parameter of the numerical phantom used in Chapter 8.*

8.3 Results

8.3.1 Adaptive scaling

To demonstrate the performance of the gf-MARTINI approach, reconstructions of the simulated numerical phantom were performed by both model-based nonlinear inverse reconstruction as well as pixel-wise fitting of magnitude images derived from the inverse DFT of fully sampled data. The images in Figure 8.3 demonstrate respective results for different configurations and z-domain oversampling.

The left block in Figure 8.3 demonstrates the result from pixel-wise GF fitting. The 17 time-domain points per pixel were hereby derived from either 64 or 512 data points in the z-domain. As most noticeable in the spin-density map (64, top), the fitting of the topmost compartment with the longest T_2 of 800 ms is very inaccurate for the 64 z-points and even produces negative values in some pixels of the reconstructed T_2 map. However, except few pixels within strong ringing, the T_2 values of the remaining regions were reconstructed with less than 2 ms deviation from the true value.

The accuracy for large T_2 values increases when oversampling with 512 z-domain points. For example, a ROI analysis of the topmost compartment in Figure 8.3 (512)

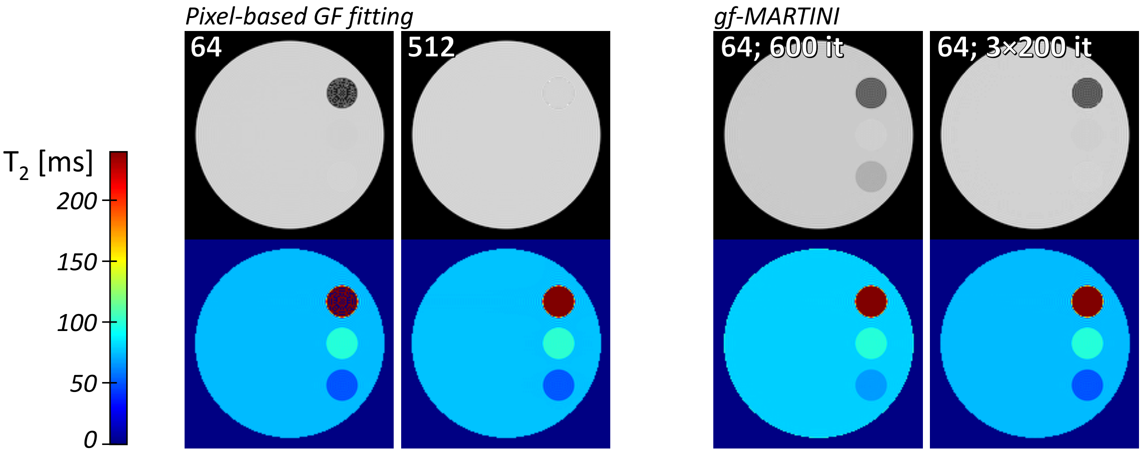

Figure 8.3: *Spin-density and T_2 maps of a numerical phantom using the GF approach with different numbers of z-domain points N_z. Pixel-based fitting (left block) is compared to gf-MARTINI reconstructions from fully sampled data (right block). For 64 z points, aliasing in z-direction causes strong model errors in the topmost compartment (64) which results in global T_2 deviations in the gf-MARTINI reconstructions (64; 600 it). The global deviations are precluded with an adaptive validity mask (64; 3×200 it).*

reveals a mean value of 823 ms, which is less than 3 % deviation from the true value. However, there are still few pixels at the compartment borders that exhibit negative T_2 values. These regions potentially lead to very high values in the respective gradient entries, when minimizing the cost function (8.6). This can cause the reconstruction algorithm to be "stuck" in vainly altering the parameter estimation in few pixels while neglecting the remote parts. Respective consequences on the global result are shown in Figure 8.3 (64; 600 it) for gf-MARTINI reconstruction of yet fully sampled data using 64 z-domain points and a fixed number of 600 CG iterations. Besides the expected deviations in the topmost compartment, also the T_2 in other regions of the phantom are notably overestimated. The deviations are most pronounced in the bottommost compartment, where the reconstructed T_2 is more than 30 % higher than the true value.

Figure 8.3 (64; 3×200 it) demonstrates that the global effect of local reconstruction obstacles can be minimized when applying the dynamic validity mask. Here the result is in good compliance with the pixel-based fit in (64). Due to the lack of negative values, the visual result in the topmost compartment even seems smoother, though the actual values are still highly overestimated.

8.3.2 SNR comparison

As has been demonstrated in Section 5.3.5, the use of a mono-exponential model on true CPMG data acquisitions may require the discard of the first echo, especially when reconstructing from undersampled data. As the data of the initial echoes usually comprise the highest overall signal strength, the discard can be expected to yield a loss of SNR in the reconstruction. This limitation is resolved when applying the GF fit. Respectively, a gain in SNR may be expected when comparing reconstructions of gf-MARTINI with the previous mono-exponential MARTINI approaches. On the other hand, errors and noise in the additionally required parameter maps for T_1 and B_1 or bad conditioning of the reconstruction model may again spoil the designated benefits. An analytical derivation of the influence from different sources of noise is beyond the scope of this work. Nevertheless, a practical impression of the SNR performance may be gained from the results in the following section.

Methods

Samples from the previously introduced noiseless GF phantom were tampered by Gaussian noise with 1 % SD of the initial spin-density signal for all echoes. The simulated homogeneous T_1 and B_1 maps, necessary for the reconstruction procedure, were also distorted such as to yield the parameters:

$$T_1 = 1000 \pm 30\,\mathrm{ms}$$
$$B_1 = 180^\circ \pm 1.8^\circ.$$

Reconstructions of the data were performed by the previously introduced model-based nonlinear inversion methods using both the standard mono-exponential model (MARTINI) and the GF approach (gf-MARTINI). Undersampling was simulated using the blocked pattern at an acceleration factor of 5. For the mono-exponential model, the first echo was discarded from the reconstruction.

Results

Figure 8.4 shows the reconstructed spin-density and T_2 parameter maps for acceleration factors of 1 and 5 using both gf-MARTINI as well as mono-exponential MARTINI. Again, the GF model allows for an accurate reconstruction of the T_2 values for all but the compartment with the highest T_2. The critical region is hereby successfully marked as invalid by the implemented mask and does not distort the remote regions in the case of undersampling. On the other hand, the mono-exponential model yields a systematic overestimation of all T_2 values.

The observations are confirmed by a ROI analysis as summarized in Table 8.2 and Figure 8.5. The (invalid) results for the topmost compartment have hereby been discarded. In fact, the T_2 overestimation of the mono-exponential model seems to be quantifiable by an approximately constant factor of 1.3. However, studies in [112] reveal that the systematic errors of mono-exponential fitting are strongly dependent on B_1 inhomogeneities. Accordingly, the relatively constant deviations in the simulations have to be ascribed to the utilization of simplified homogeneous field maps and cannot be assumed to apply for true MRI data.

Though gf-MARTINI yields a notably increased quantitative accuracy when reconstructing model-compliant data, an additional gain in SNR cannot be found in the

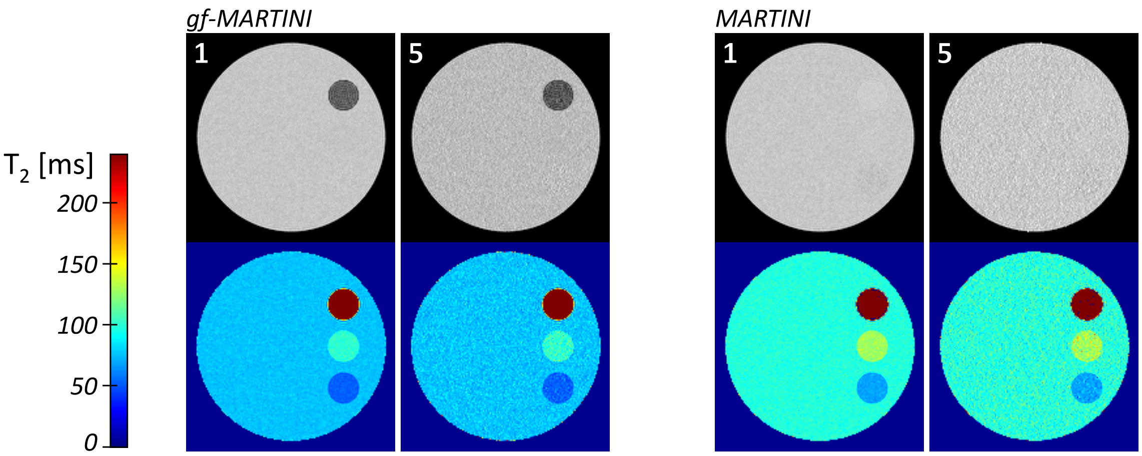

Figure 8.4: *Spin-density and T_2 maps of a noisy numerical phantom using gf-MARTINI (left block) as well as mono-exponential MARTINI (right block). Spin-density maps from the different models are individually windowed.*

Compartment	bottom	center	surrounding
True value	50	100	75
GF, AF = 1	50 ± 3	98 ± 4	74 ± 3
GF, AF = 5	50 ± 7	99 ± 11	74 ± 8
Mono, AF = 1	66 ± 3	126 ± 5	96 ± 4
Mono, AF = 5	67 ± 8	126 ± 13	97 ± 11

Table 8.2: *ROI-based analysis of T_2 relaxation times from model-based reconstructions of the numerical phantom. The results from gf-MARTINI and mono-exponential MARTINI are compared for different acceleration factors. T_2 values (ms) represent mean ± SD.*

results. Even though the absolute SD values for the GF are slightly smaller than for mono-exponential MARTINI, this difference no longer applies when setting the standard deviation in relation to the respective means.

8.3.3 Human brain MRI

Methods

A young healthy volunteer with no known abnormalities participated in this study and gave written informed consent before each MRI examination. Field map, T_1 values and CPMG data samples were acquired for the same anatomical region using the methods and parameters summarized in Table 8.3. Spin-density and T_2 maps were reconstructed from the CPMG data using the mono-exponential and GF-based MARTINI methods. Again, undersampling of the data was performed by selecting respective lines from the fully sampled data using the blocked sampling scheme for different acceleration factors. Reference reconstructions from fully sampled data were created for both models using the Levenberg-Marquard algorithm on magnitude images from the sum-of-squares of

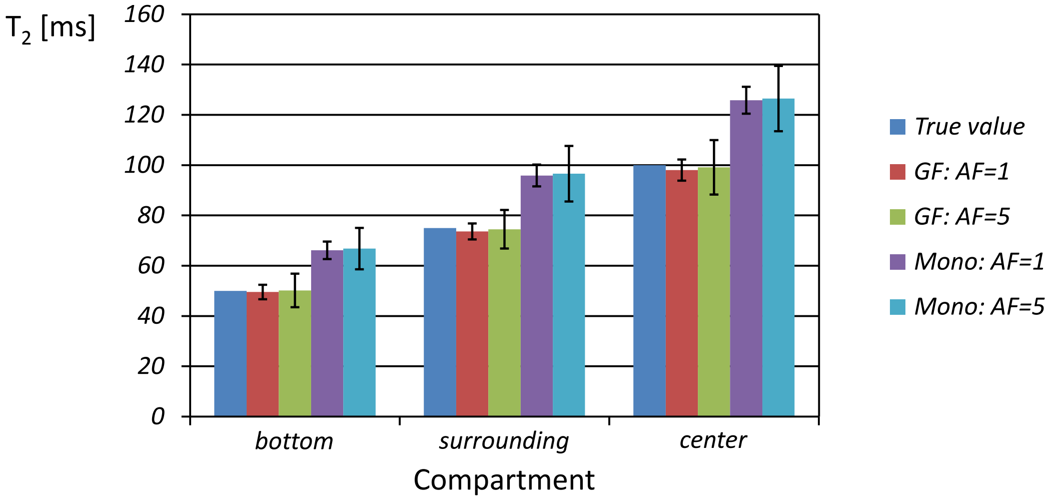

Figure 8.5: *Mean values from a ROI-based analysis of the T_2 maps in Figure 8.4. Error bars correspond to the standard deviation in the respective ROIs.*

all receiver channels. The signal in z-domain was calculated for 64 points while only the first 25 points were further used in time domain. Other reconstruction parameters as well as the dynamic validity mask were configured as described in Section 8.1.3, while coil sensitivities were again estimated in a pre-processing step as introduced in Section 5.2.2.

Results

Figure 8.6 (top) shows spin-density and T_2 maps of the human brain, reconstructed using the GF approach. Pixel-based fitting is compared to gf-MARTINI reconstructions from undersampled data using the blocked sampling scheme at undersampling factors of 4, 6, and 10. The originally squared 192×192 point image-matrix has retrospectively been cropped in read direction for convenience.

The spin-density maps reveal several dark regions within the CSF and indicate the expected model limitations at prolonged T_2 values. However, the regions are reliably marked by the applied dynamic mask. For higher acceleration factors the quality of the spin-density maps clearly degrades and exhibits blurring as well as edge enhancement. The reconstructed T_2 maps on the other hand are in remarkably good agreement with the fully sampled reference up to the highest AF of 10.

Figure 8.6 (bottom) shows respective reconstructions from the same dataset using mono-exponential MARTINI. The equally windowed T_2 maps highlight the quantitative difference to the GF approach. A qualitative degradation with increasing AF is again most noticeable in the spin-density maps. However, the general reconstruction quality seems rather less prone to blurring than in the GF approach.

A ROI analysis of the reconstructions is summarized in Table 8.4. Again, the T_2 values from mono-exponential MARTINI are systematically over-estimated. Apart from that, a noticeable reduction of noise due to the more advanced data modeling could not

Scanner hardware	
field strength	3T
manufacturer	Siemens Healthcare, Erlangen, Germany
system	Tim Trio
MSE Sequence	
Δt	10 ms
FOV	$250 \times 250\,\mathrm{mm}^2$
slice thickness	4 mm
matrix	192×192
NE	25
TR	4000 ms
scan time	12:47 min
TIR Sequence	
FOV	$250 \times 250\,\mathrm{mm}^2$
slice thickness	4 mm
matrix	192×192
TR	7000 ms
TE	7.8 ms
TI	$100 - 3100$ ms
NI	5
turbo factor	7
PI acceleration	2
ACL	31
scan time	8:45 min
Field map	
method	BLOCH SIEGERT shift [113]
sequence	FLASH
TR	200 ms
NS	5
FOV	$250 \times 250\,\mathrm{mm}^2$
slice thickness	8 mm
matrix	64×32
pulse	Gaussian
duration	8 s
$B_{1,\mathrm{peak}}$	0.11 G
K_{BS}	21.3 rad/G^2/ms
f_{OR}	8 kHz
scan time	32 sec

Table 8.3: *MRI parameters for human brain acquisitions evaluated in Section 8.3.3.*

be found.

		Acceleration Factor			
GF	Pixel Fitting	1	4	6	10
Anterior Cingulate	71 ± 6	71 ± 6	71 ± 6	71 ± 6	70 ± 7
Insular Cortex	74 ± 7	74 ± 7	76 ± 8	77 ± 8	77 ± 10
Thalamus	59 ± 2	59 ± 2	60 ± 2	61 ± 3	59 ± 3
Putamen	55 ± 4	55 ± 4	56 ± 4	57 ± 4	56 ± 4
Internal Capsule	69 ± 4	68 ± 4	69 ± 4	70 ± 4	69 ± 4
Frontal White Matter	59 ± 2	58 ± 2	59 ± 2	60 ± 3	59 ± 3
Mono					
Anterior Cingulate	101 ± 8	101 ± 8	99 ± 8	98 ± 9	98 ± 8
Insular Cortex	100 ± 10	99 ± 10	99 ± 10	98 ± 10	99 ± 11
Thalamus	84 ± 3	84 ± 3	83 ± 3	83 ± 3	84 ± 4
Putamen	76 ± 5	75 ± 5	75 ± 5	75 ± 6	75 ± 6
Internal Capsule	96 ± 6	95 ± 6	93 ± 5	93 ± 6	94 ± 6
Frontal White Matter	81 ± 3	81 ± 3	80 ± 3	79 ± 3	80 ± 4

Table 8.4: *ROI-based analysis of T_2 relaxation times from model-based reconstructions of the human brain. The result from gf-MARTINI and mono-exponential MARTINI are compared for different acceleration factors. T_2 values (ms) represent mean ± SD.*

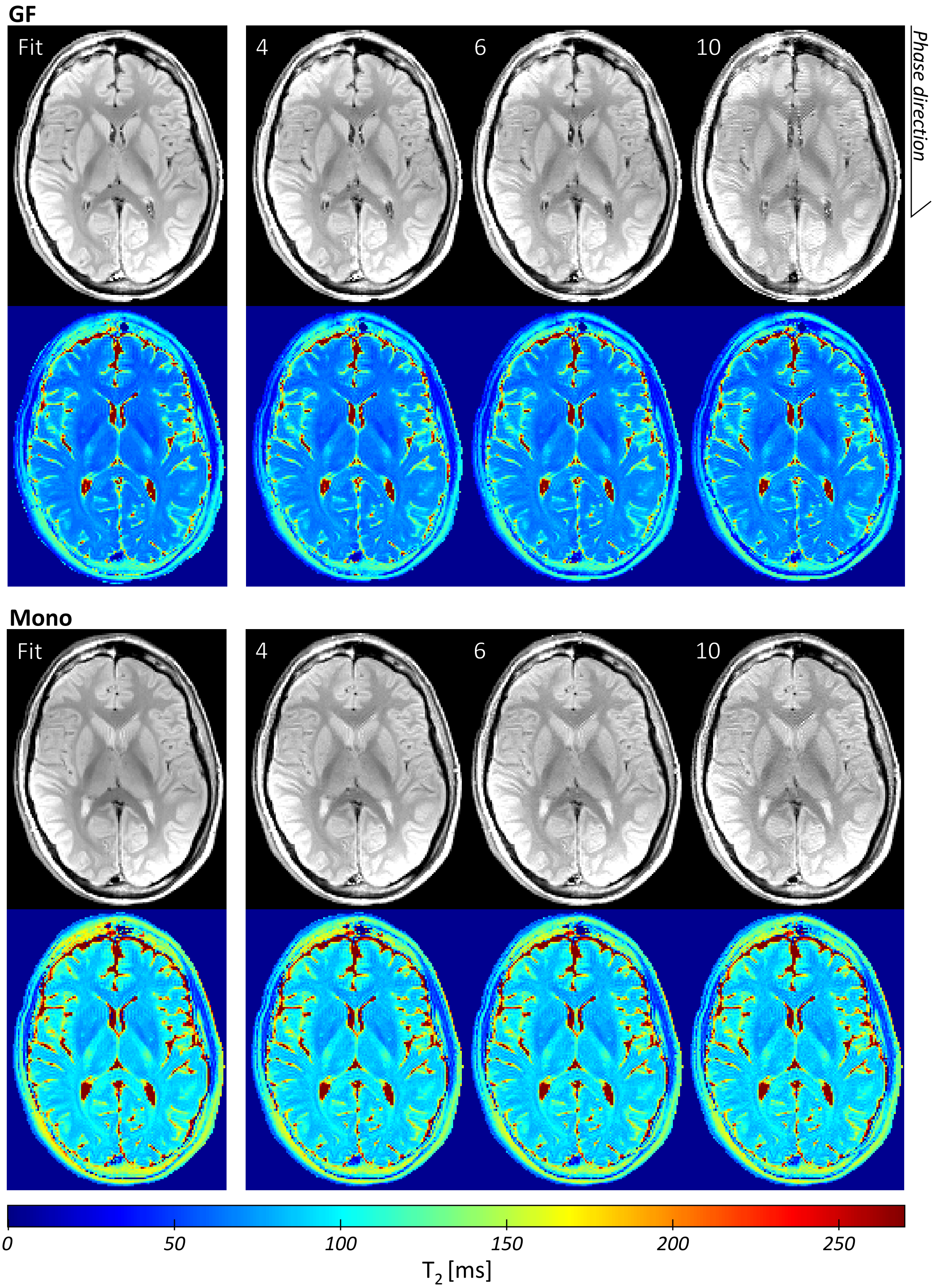

Figure 8.6: *Pixel-based fitting (fully sampled k-space data) versus model-based reconstructions of spin-density and T_2 maps of the human brain at different degrees of undersampling. The gf-MARTINI approach (top) is compared to mono-exponential MARTINI (bottom). Spin-density maps from the different models are individually windowed.*

8.4 Discussion

The studies demonstrate that the recently introduced GF approach for accurate T_2 mapping is applicable for model-based reconstructions from undersampled data. The resulting modeled signal curves fit accurately to the true signal decay of CPMG sequences. Especially the capability of the GF model to recreate the hypo-intense first echo demonstrates the insufficiency of the wide-spread mono-exponential model. While the visual impression of the reconstructed T_2 maps from undersampled data is comparable to the reconstructions using mono-exponential modeling, the result for spin-density reconstruction in human brain MRI appears more prone to artifacts. However, due to the quantitative superiority of the GF model [111, 112], the method is still beneficial in applications where the actual T_2 values are of higher relevance than just the qualitative tissue contrast. Also, as for EPG-based fitting [114], the approach may improve the comparability of T_2 estimations from different sites or MRI systems which is often not the case for mono-exponential reconstructions [114].

The present proof-of-principle experiments reveal the necessity for an adaptive detection of regions with invalid signal behavior or prolonged T_2 when using the proposed model function with limited oversampling. However, the CG optimization cannot deal with dynamically changing objective functions and needs to be restarted after every adaption of the implemented mask. To avoid the disadvantageous increase in necessary iteration steps, the use of alternative optimization algorithms might be beneficial for this approach. For example, the GAUSS-NEWTON method with the mask updated after every Newton step might be a more appropriate choice.

Furthermore it is conceivable to treat the B_1 field map as an additional unknown to be jointly estimated from CPMG data rather than from an additional dedicated scan. Respective preliminary results are very promising for pixel-wise fitting. However, a stable implementation for model-based reconstruction is still under elaboration. In general, for routine use, an automatic initial dimensioning of the involved gradient scaling would be highly desirable.

9

Summary and Outlook

9.1 Summary

Model-based reconstructions of parametric maps serve several purposes: They may contribute to a reduction of the measuring time or - for a constant measuring time - increase the spatial resolution and thus improve the image quality. The optimal use of all available data might also be exploited to enhance the scanning efficiency, for example by allowing for more sections. The main advantage compared to FSE imaging is the access to quantitative measures of tissue properties. For the clinically relevant case of T_2 relaxation, the present work offers solutions that employ a standard spin-echo MRI sequence with multiple echoes. Because of the restraint to Cartesian encoding, the developed methods require only minor modifications for implementing the undersampling scheme. The calculation of differently T_2-weighted images from fully sampled k-space data is no longer necessary and the retrospective fitting by a T_2 relaxation decay is replaced by a direct nonlinear inversion of the underlying signal model.

The experiments in this work also reveal the strong dependency of a successful reconstruction on the ability to accurately model the true signal behavior in every point of the later images. For fully sampled data, image regions or pixels which do not comply with the model assumptions yield residual energy in the applied cost function. Removal of reconstruction constraints due to undersampling can then cause the optimization process to find numerically favorable results that lead to physically incorrect solutions. The corresponding artifacts in the reconstructed parameter maps are shaped by the point spread function of the undersampling procedure.

Experiments in Chapter 7 demonstrate the possibility to extend the reconstruction by less restrictive model formulations, for example by oversampling of the vector of unknowns. However, while this approach yields promising results for model violations related to data truncation, it does not assure artifact-free reconstructions for true MRI data with a broader variety of error sources. It is conceivable to further improve the reconstruction by incorporating prior knowledge into the cost function using suitable regularization terms. For example, penalizing the total variation of the maps may suppress ringing artifacts and preclude noise amplifications during the iterative optimization. However, because there is no generally accepted method for objectively choosing the inherent regularization parameters, this option is left for future extensions.

Truly accurate modeling of the CPMG echo train also requires more complicated model descriptions than the widely used mono-exponential decay. A good compromise between complexity and accuracy might be given by the recently reported generating function approach, which here is evaluated for model-based reconstructions in Chapter 8. As a disadvantage, the method relies on additional information such as T_1 and B_1 maps and still does not account for phase perturbations in image space.

Regardless of the method, all performed experiments reveal the necessity of an appropriate undersampling scheme to avoid ghosting artifacts due to remaining model insufficiencies. While a suitable scheme could be developed for Cartesian sampling, an alternative scheme for state-of-the-art MRI systems may also be found in radial trajectories, as proposed by Block et al. [2]. However, these techniques still pose additional challenges on both the acquisition and reconstruction site such as well adjusted hardware and regularization parameters. In contrast, the proposed Cartesian implementation provides a robust technical solution without manual tuning.

In conclusion, depending on the available SNR, all evaluated methods allow for much higher undersampling factors than commonly achievable by parallel imaging by exploiting data redundancy in parameter space. In fact, the methods even work without the need for data redundancy due to multiple receiver coils and therefore are applicable in settings where only a single or very few coils are available. This feature is of particular interest for animal MRI studies, where coil arrays with more than 4 elements are far less common than in state-of-the-art human MRI systems. On the other hand, the availability of multiple receiver coils not only ensures optimum SNR, but may improve the condition number of the undersampled reconstructions due to the inherent parallel imaging principles. Accordingly, the combined data redundancies from multiple coils and multiple echoes provide access to the largest undersampling factors that clearly exceed the values commonly obtained by conventional parallel MRI. Furthermore, due to the developed automatic gradient scaling, the MARTINI method in Chapter 5 is directly applicable for routine use. In cooperation with Siemens (Erlangen, Germany), the approach is therefore currently evaluated in a clinical study, where the required sampling pattern has already been successfully implemented on a commercial MRI system.

9.2 Future work

A practical drawback of all presented reconstruction methods is the relatively long reconstruction time. However, there are various possibilities for speed improvements. For example, so-called *array compression* techniques can be applied to the original data prior to the iterative optimization process. A commonly used method for reducing the dimensionality of a problem is the principal component analysis (PCA) [115], which has already been successfully included to the reconstruction algorithms and allows for a substantial speed-up when reconstruction is performed for more than 10 receiver channels. Moreover, MRI-specific adaptations of the PCA principles have been proposed that might further reduce the data overhead [116, 117, 118]. Furthermore, we expect a substantial reduction of the computational time with the use of graphical processing units as most of the calculations can be performed in parallel.

Despite extensive efforts, a robust transfer of the model-based reconstruction approach to a high-field animal MRI system has not yet succeeded. Increased phase perturbations in image space have been identified as the main experimental limitation. Although several model extensions have already been tested to account for the problems, the experiments indicate the necessity of additional improvements on the acquisition site, for example by choosing alternative pulse shapes or gradient correction schemes.

Finally, the developed reconstruction and simulation framework can further be extended for T_2^* and T_1 relaxation models and bears considerable potential to be transferred to other MRI sequences and applications in future.

A

Appendix

A.1 Derivatives of the model consistency term for k-MARTINI

The model consistency term in Section 7.2.3 has been defined as

$$\Phi_m = \frac{\lambda_m}{2} \sum_{n=1}^{\mathrm{NE}-1} \| \underbrace{S_r \, \mathrm{F}_{\mathrm{xy}}^{-1} \left[\mathrm{F}_{\mathrm{xy}}(E_s \, \mathbf{L}_s \, \tilde{\mathbf{s}}_n) \cdot \mathrm{F}_{\mathrm{xy}}(E_r \, \mathbf{L}_r \, \tilde{\mathbf{r}}) \right] - \mathbf{L}_s \, \tilde{\mathbf{s}}_{n+1}}_{\mathfrak{r}_n} \|_2^2, \tag{A.1}$$

with $\tilde{\mathbf{s}}_n$ and $\tilde{\mathbf{r}}$ as complex vectors of unknowns in k-space. The complex vector $\mathfrak{r}_n$ will be used as abbreviation for the residuum at echo number n in the following. While the results for Φ_m (and also the components in $\mathfrak{r}_n$) are nonlinearly dependent on the vectors of unknowns, the components of the gradient $\nabla\Phi$ can conveniently be derived from linear sub-problems using the known relation

$$\nabla \frac{1}{2} \|\mathbf{A}\mathbf{x} - \mathbf{y}\|_2^2 = \mathbf{A}^H (\mathbf{A}\mathbf{x} - \mathbf{y}). \tag{A.2}$$

The procedure will be described in the following.

Gradient with respect to $\tilde{\mathbf{s}}$

For the derivatives with respect to $\tilde{\mathbf{s}}_k$, Equation (A.1) can be written as

$$\Phi_m = \frac{\lambda_m}{2} \sum_{n=1}^{\mathrm{NE}-1} \|\mathbf{K} \, \tilde{\mathbf{s}}_n - \mathbf{L}_s \, \tilde{\mathbf{s}}_{n+1}\|_2^2, \tag{A.3}$$

with $\mathbf{K}$ being a combination of linear matrix operations:

$$\begin{aligned}
\mathbf{K} &= \mathbf{S}_r\ \mathbf{F}^H\ \mathbf{Q}\ \mathbf{U}, \qquad &\text{(A.4)}\\
\mathbf{Q} &= \operatorname{diag}\left\{\mathrm{F}_{\mathrm{xy}}(E_r\ L_r\ \tilde{\mathbf{r}})\right\} &\text{(A.5)}\\
&= \operatorname{diag}\left\{\mathbf{F}\ \mathbf{E}_r\ \mathbf{L}_r\ \tilde{\mathbf{r}}\right\}, &\text{(A.6)}\\
\mathbf{U} &= \mathbf{F}\ \mathbf{E}_s\ \mathbf{L}_s, &\text{(A.7)}
\end{aligned}$$

and the bold $\mathbf{F}$, $\mathbf{E}$ and $\mathbf{L}$ being matrix representations of the respective "normal-lettered" operators. With that, the partial gradients

$$\nabla_{\tilde{\mathbf{s}}_k}\Phi_m = \lambda_m \sum_j \nabla_{\tilde{\mathbf{s}}_k}\ \Phi_{m,j} \tag{A.8}$$

can be evaluated separately for different ranges of n.

For $n = k$, $k = 1$ ... NE -1 the gradient for this equation can be calculated according to Equation (A.2):

$$\begin{aligned}
\nabla_{\tilde{\mathbf{s}}_k}\Phi_{m,1} &= \nabla_{\tilde{\mathbf{s}}_k}\frac{1}{2}\|\mathbf{K}\ \tilde{\mathbf{s}}_k - \mathbf{L}_s\ \tilde{\mathbf{s}}_{k+1}\|_2^2 \qquad &\text{(A.9)}\\
&= \mathbf{K}^H(\mathbf{K}\ \tilde{\mathbf{s}}_k - \mathbf{L}_s\ \mathbf{s}_{k+1}) &\text{(A.10)}\\
&= (\mathbf{S}_r\ \mathbf{F}^H\ \mathbf{Q}\ \mathbf{U})^H\mathfrak{r}_n &\text{(A.11)}\\
&= \mathbf{U}^H\ \mathbf{Q}^H\ \mathbf{F}\ \mathbf{S}_r^H\ \mathfrak{r}_n. &\text{(A.12)}
\end{aligned}$$

With $\mathbf{S}^H = \mathbf{E}$ and assuming the diagonal scaling matrices $\mathbf{L}$ to be real:

$$\nabla_{\tilde{\mathbf{s}}_k}\Phi_{m,1} = \mathbf{L}_s\ \mathbf{S}_s\ \mathbf{F}^H\ \mathbf{Q}^H\ \mathbf{F}\ \mathbf{E}_r\ \mathfrak{r}_n. \tag{A.13}$$

For $n = k - 1$, $k = 2$ ... NE the gradient

$$\nabla_{\tilde{\mathbf{s}}_k}\Phi_{m,2} = \nabla_{\tilde{\mathbf{s}}_k}\ \frac{1}{2}\|\mathbf{K}\ \tilde{\mathbf{s}}_{k-1} - \mathbf{L}_s\ \tilde{\mathbf{s}}_k\|_2^2 \tag{A.14}$$

can be reordered to:

$$\nabla_{\tilde{\mathbf{s}}_k}\Phi_{m,2} = \nabla_{\tilde{\mathbf{s}}_k}\ \frac{1}{2}\|\mathbf{A}\ \tilde{\mathbf{s}}_k - \mathbf{y}\|_2^2, \tag{A.15}$$

with $\mathbf{A} = -\mathbf{L}_s$ and $\mathbf{y} = -\mathbf{K}\ \mathbf{s}_{k-1}$. Again, according to Equation (A.2):

$$\begin{aligned}
\nabla_{\tilde{\mathbf{s}}_k}\Phi_{m,2} &= \mathbf{A}^H(\mathbf{A}\ \tilde{\mathbf{s}}_k - \mathbf{y}) \qquad &\text{(A.16)}\\
&= -\mathbf{L}_s^H(-\mathbf{L}_s\ \tilde{\mathbf{s}}_k + \mathbf{K}\ \tilde{\mathbf{s}}_{k-1}) &\text{(A.17)}\\
&= \mathbf{L}_s(\mathbf{L}_s\ \tilde{\mathbf{s}}_k - \mathbf{K}\ \tilde{\mathbf{s}}_{k-1}) &\text{(A.18)}\\
&= \mathbf{L}_s(\mathbf{L}_s\ \tilde{\mathbf{s}}_{n+1} - \mathbf{K}\ \tilde{\mathbf{s}}_n) &\text{(A.19)}\\
&= -\mathbf{L}_s\mathfrak{r}_n. &\text{(A.20)}
\end{aligned}$$

Gradient with respect to $\tilde{\mathbf{r}}$

For the gradient with respect to $\tilde{\mathbf{r}}$, the cost function can be simplified to:

$$\Phi_m = \frac{\lambda_m}{2} \sum_{n=1}^{\mathrm{NE}-1} \|\mathbf{K}\ \tilde{\mathbf{r}} - \mathbf{y}\|_2^2, \tag{A.21}$$

with $\mathbf{y} = \mathbf{L}_s\ \tilde{\mathbf{s}}_{n+1}$ and $\mathbf{K}$ being again the composition:

$$\mathbf{K} = \mathbf{S}_r\ \mathbf{F}^H\ \mathbf{Q}\ \mathbf{U} \tag{A.22}$$

of the re-defined matrix operators:

$$\mathbf{Q} = \operatorname{diag}\left\{\mathbf{F}\ \mathbf{E}_s\ \mathbf{L}_s\ \tilde{\mathbf{s}}_n\right\}, \tag{A.23}$$

$$\mathbf{U} = \mathbf{F}\ \mathbf{E}_r\ \mathbf{L}_r. \tag{A.24}$$

With that, the gradient yields:

$$\begin{aligned}
\nabla_{\tilde{\mathbf{s}}_r}\Phi_m &= \lambda_m \nabla_{\tilde{\mathbf{s}}_r} \sum_{n=1}^{\mathrm{NE}-1} \frac{1}{2}\|\mathbf{K}\ \tilde{\mathbf{s}}_k - \mathbf{y}\|_2^2 && \text{(A.25)}\\
&= \lambda_m \sum_{n=1}^{\mathrm{NE}-1} \mathbf{U}^H\ \mathbf{Q}^H\ \mathbf{F}\ \mathbf{S}_r^H\ \mathfrak{r}_n && \text{(A.26)}\\
&= \lambda_m \sum_{n=1}^{\mathrm{NE}-1} \mathbf{L}_r\ \mathbf{S}_r\ \mathbf{F}^H\ \mathbf{Q}^H\ \mathbf{F}\ \mathbf{E}_r\ \mathfrak{r}_n. && \text{(A.27)}
\end{aligned}$$

Scaling

As the overall energy in the different echo numbers reduces with n, a standardization of every gradient component would require individual scaling for every echo. However, for the CG-Descent optimization of Equation (A.1) to succeed, it is sufficient to roughly scale the gradient components to the same order of magnitude. Therefore, the residuals $\mathfrak{r}_n$ have been assumed to be similar for every echo ($\mathfrak{r}_1 \approx \mathfrak{r}_2 \approx \ldots \approx \mathfrak{r}$) and a single diagonal matrix $\mathbf{L}_s$ has been used for all echoes.

Working on the original vector size, the matrices for vector shrinking ($\mathbf{S}$) and enlargement ($\mathbf{E}$) reduce to the identity $\mathbf{I}$. For the dimensioning of the scaling vectors, the operators $\mathbf{F}$ and $\mathbf{F}^H$ can also be substituted by the identity, as the DFT preserves all energy in the data. With that, the gradients for $\tilde{\mathbf{r}}$ and the central echo samples $\tilde{\mathbf{s}}$ can be simplified to

$$\nabla_{\tilde{\mathbf{s}}}\Phi_m = \mathbf{L}_s(\hat{\mathbf{r}} - \mathbf{1}) \cdot \mathfrak{r} \tag{A.28}$$

$$\nabla_{\tilde{\mathbf{r}}}\Phi_m = \mathbf{L}_r \sum_n \hat{\mathbf{s}}_n \cdot \mathfrak{r}, \tag{A.29}$$

with $(\cdot)$ denoting point-wise multiplication and $\mathbf{1} = (1, 1, \ldots, 1)$.
Accordingly, the scaling matrices can be approximated to

$$\mathbf{L}_s = \left[(\hat{\mathbf{r}} - \mathbf{1})\right]^{-1} \tag{A.30}$$

$$\mathbf{L}_r = \left[\sum_n \hat{\mathbf{s}}_n\right]^{-1}. \tag{A.31}$$

Abbreviations

T_1	spin-lattice relaxation time
T_2	spin-spin relaxation time
T_2^*	effective spin-spin relaxation time
ADC	analog-to-digital converter
AF	acceleration factor
CG	conjugate gradient
CPMG	Carr-Purcell-Meiboom-Gill
CT	computerized tomography
DFT	discrete Fourier transform
EPG	extended phase graph
FAISE	fast acquisition interleaved spin echo
FFT	fast Fourier transform
FISP	fast imaging with steady state precession
FLASH	fast low angle shot
FOV	field of view
FSE	fast spin echo
GF	generating function
iDFT	inverse discrete Fourier transform
IRGNM	iteratively regularized Gauss-Newton method
MSE	multiple spin echo
NE	number of echoes

NMR	nuclear magnetic resonance
OMP	orthogonal matching pursuit
PCA	principal component analysis
PI	parallel imaging
ppm	parts per million
RAM	random access memory
RARE	rapid acquisition with relaxation enhancement
RF	RARE factor
rf	radiofrequency
RSS	root of sum of squares
SENSE	sensitivity encoding
SMASH	simultaneous acquisition of spatial harmonics
SNR	signal-to-noise ratio
STEAM	stimulated echo acquisition mode
TE	echo time
TR	repetition time
TSE	turbo spin echo

Bibliography

[1] PC Lauterbur et al. Image formation by induced local interactions: examples employing nuclear magnetic resonance. *Nature*, 242(5394):190–191, 1973. 1, 11, 16

[2] KT Block, M. Uecker, and J. Frahm. Model-based iterative reconstruction for radial fast spin-echo MRI. *IEEE*, 28(11):1759–1769, 2009. 2, 27, 47, 114

[3] EM Haacke, RW Brown, MR Thompson, and R. Venkatesan. *Magnetic resonance imaging: physical principles and sequence design*, volume 82. Wiley-Liss New York:, 1999. 2, 5, 6

[4] ZP Liang, PC Lauterbur, IEEE Engineering in Medicine, and Biology Society. *Principles of magnetic resonance imaging: a signal processing perspective*. IEEE Press series in biomedical engineering. SPIE Optical Engineering Press, 2000. 5, 6, 8

[5] MA Bernstein, KE King, XJ Zhou, and W. Fong. Handbook of MRI pulse sequences. *Medical Physics*, 32:1452, 2005. 5, 24, 40, 41, 43

[6] F. Bloch, WW Hansen, and M. Packard. Nuclear induction. *Physical review*, 70(7-8):460–474, 1946. 5, 9

[7] EM Purcell, HC Torrey, and RV Pound. Resonance absorption by nuclear magnetic moments in a solid. *Physical review*, 69(1-2):37–38, 1946. 5

[8] W. Gerlach and O. Stern. Über die Richtungsquantelung im Magnetfeld. *Annalen der Physik*, 379(16):673–699, 1924. 6

[9] A. Hendrix. *Magnets, Spins, and Resonance: An introduction to the basics of Magnetic Resonance*. Siemens AG, 2003. 6

[10] CP Slichter. *Principles of magnetic resonance*, volume 1. Springer Verlag, 1990. 6, 7, 10

[11] *Collins dictionary*. HarperCollins, 2010. 6

[12] HC Torrey. Bloch equations with diffusion terms. *Physical Review*, 104(3):563, 1956. 9

[13] EL Hahn. Spin echoes. *Physical Review*, 80(4):580, 1950. 10

[14] EL Hahn and DE Maxwell. Spin echo measurements of nuclear spin coupling in molecules. *Physical Review*, 88(5):1070, 1952. 10

[15] O. Natt. *Entwicklung von Verfahren für In-vivo-NMR-Untersuchungen des Gehirns der Maus*. Cuvillier, 2002. 10

[16] J. Frahm, KD Merboldt, W. Hanicke, and A. Haase. Stimulated echo imaging. *Journal of Magnetic Resonance (1969)*, 64(1):81–93, 1985. 10

[17] J. Frahm, KD Merboldt, and W. Hänicke. Localized proton spectroscopy using stimulated echoes. *Journal of Magnetic Resonance (1969)*, 72(3):502–508, 1987. 10

[18] A. Kumar, D. Welti, and RR Ernst. NMR fourier zeugmatography. *Journal of Magnetic Resonance (1969)*, 18(1):69–83, 1975. 11

[19] CE Shannon. Communication in the presence of noise. *Proceedings of the IRE*, 37(1):10–21, 1949. 15

[20] DC Peters, JA Derbyshire, and ER McVeigh. Centering the projection reconstruction trajectory: reducing gradient delay errors. *Magnetic resonance in medicine*, 50(1):1–6, 2003. 16

[21] CB Ahn, JH Kim, and ZH Cho. High-speed spiral-scan echo planar NMR imaging. *IEEE Transactions on Medical Imaging*, 5(1):2–7, 1986. 16

[22] DC Noll. Multishot rosette trajectories for spectrally selective MR imaging. *IEEE Transactions on Medical Imaging*, 16(4):372–377, 1997. 16

[23] K. Scheffler and J. Hennig. Frequency resolved single-shot MR imaging using stochastic k-space trajectories. *Magnetic resonance in medicine*, 35(4):569–576, 1996. 16

[24] R. Van de Walle, T. Voet, and I. Lemahien. The motion sensitivity of magnetic resonance imaging: A comparison between fourier transform imaging and projection reconstruction. In *Engineering in Medicine and Biology Society, 1995., IEEE 17th Annual Conference*, volume 1, pages 457–458. IEEE, 1995. 16

[25] M. Uecker, S. Zhang, D. Voit, A. Karaus, K.D. Merboldt, and J. Frahm. Real-time MRI at a resolution of 20 ms. *NMR in Biomedicine*, 23(8):986–994, 2010. 16

[26] S. Zhang, KT Block, and J. Frahm. Magnetic resonance imaging in real time: Advances using radial flash. *Journal of Magnetic Resonance Imaging*, 31(1):101–109, 2010. 16

[27] JM Jin. *Electromagnetic analysis and design in magnetic resonance imaging*. Biomedical engineering series. CRC Press, 1999. 16

[28] PB Roemer, WA Edelstein, CE Hayes, SP Souza, and OM Mueller. The NMR phased array. *Magnetic Resonance in Medicine*, 16(2):192–225, 1990. 17

[29] DO Walsh, AF Gmitro, and MW Marcellin. Adaptive reconstruction of phased array MR imagery. *Magnetic Resonance in Medicine*, 43(5):682–690, 2000. 17

[30] M. Bydder, DJ Larkman, and JV Hajnal. Combination of signals from array coils using image-based estimation of coil sensitivity profiles. *Magnetic Resonance in Medicine*, 47(3):539–548, 2002. 17

[31] CJG Bakker, CN Graaf, and P. Dijk. Derivation of quantitative information in NMR imaging: a phantom study. *Physics in medicine and biology*, 29:1511, 1984. 19

[32] R. Damadian. Tumor detection by nuclear magnetic resonance. *Science*, 171(3976):1151, 1971. 19

[33] PA Bottomley, TH Foster, RE Argersinger, and L.M. Pfeifer. A review of normal tissue hydrogen NMR relaxation times and relaxation mechanisms from 1–100 mhz: dependence on tissue type, NMR frequency, temperature, species, excision, and age. *Medical Physics*, 11:425, 1984. 19

[34] KR Rao and PC Yip. *The transform and data compression handbook*. CRC Press, 2001. 22

[35] M. Hutchinson and U. Raff. Fast MRI data acquisition using multiple detectors. *Magnetic resonance in Medicine*, 6(1):87–91, 1988. 23

[36] JR Kelton, RL Magin, and SM Wright. An algorithm for rapid image acquisition using multiple receiver coils. In *Proceedings of the SMRM 8th Annual Meeting, Amsterdam*, page 1172, 1989. 23

[37] JB Ra and CY Rim. Fast imaging using subencoding data sets from multiple detectors. *Magnetic resonance in medicine*, 30(1):142–145, 1993. 23, 25

[38] KP Pruessmann, M. Weiger, MB Scheidegger, and P. Boesiger. Sense: sensitivity encoding for fast MRI. *Magnetic Resonance in Medicine*, 42(5):952–962, 1999. 23, 24

[39] DK Sodickson and WJ Manning. Simultaneous acquisition of spatial harmonics (smash): fast imaging with radiofrequency coil arrays. *Magnetic Resonance in Medicine*, 38(4):591–603, 1997. 23

[40] KP Pruessmann, M. Weiger, P. Börnert, and P. Boesiger. Advances in sensitivity encoding with arbitrary k-space trajectories. *Magnetic Resonance in Medicine*, 46(4):638–651, 2001. 23

[41] PM Jakob, MA Grisowld, RR Edelman, and DK Sodickson. Auto-smash: a self-calibrating technique for smash imaging. *Magnetic Resonance Materials in Physics, Biology and Medicine*, 7(1):42–54, 1998. 23, 25

[42] MA Griswold, PM Jakob, RM Heidemann, M. Nittka, V. Jellus, J. Wang, B. Kiefer, and A. Haase. Generalized autocalibrating partially parallel acquisitions (grappa). *Magnetic Resonance in Medicine*, 47(6):1202–1210, 2002. 23

[43] RM Heidemann, Ö. Özsarlak, PM Parizel, J. Michiels, B. Kiefer, V. Jellus, M. Müller, F. Breuer, M. Blaimer, MA Griswold, et al. A brief review of parallel magnetic resonance imaging. *European radiology*, 13(10):2323–2337, 2003. 23

[44] M. Blaimer, F. Breuer, M. Mueller, RM Heidemann, MA Griswold, and PM Jakob. Smash, sense, pils, grappa: how to choose the optimal method. *Topics in Magnetic Resonance Imaging*, 15(4):223, 2004. 23

[45] EH Moore. On the reciprocal of the general algebraic matrix. *Bull. Amer. Math. Soc*, 26:394–395, 1920. 24

[46] R. Penrose. A generalized inverse for matrices. In *Proc. Cambridge Philos. Soc*, volume 51, page C655. Cambridge Univ Press, 1955. 24

[47] WS Hoge, DH Brooks, B. Madore, and WE Kyriakos. A tour of accelerated parallel MR imaging from a linear systems perspective. *Concepts in Magnetic Resonance Part A*, 27(1):17–37, 2005. 24

[48] MR Hestenes and E. Stiefel. Methods of conjugate gradients for solving linear systems. *Journal of Research of the National Bureau of Standards*, 49(6):409–436, December 1952. 24

[49] CA McKenzie, EN Yeh, MA Ohliger, MD Price, and DK Sodickson. Self-calibrating parallel imaging with automatic coil sensitivity extraction. *Magnetic resonance in medicine*, 47(3):529–538, 2002. 25

[50] KP Pruessmann, M. Weiger, MB Scheidegger, and P. Boesiger. Coil sensitivity maps for sensitivity encoding and intensity correction. In *ISMRM 6th Annual Meeting, Sydney*, page 2087. ISMRM 6th Annual Meeting, 1998. 25

[51] M. Uecker, T. Hohage, KT Block, and J. Frahm. Image reconstruction by regularized nonlinear inversion - joint estimation of coil sensitivities and image content. *Magnetic Resonance in Medicine*, 60(3):674–682, 2008. 26

[52] L. Ying and J. Sheng. Joint image reconstruction and sensitivity estimation in sense (jsense). *Magnetic Resonance in Medicine*, 57(6):1196–1202, 2007. 26

[53] WW Hager and H. Zhang. A new conjugate gradient method with guaranteed descent and an efficient line search. *SIAM Journal of Optimization*, 16(1):170, 2006. 27, 47

[54] DL Donoho. Compressed sensing. *IEEE Transactions on Information Theory*, 52(4):1289–1306, 2006. 27

[55] EJ Candès, J. Romberg, and T. Tao. Robust uncertainty principles: Exact signal reconstruction from highly incomplete frequency information. *IEEE Transactions on Information Theory*, 52(2):489–509, 2006. 27

[56] KT Block, M. Uecker, and J. Frahm. Undersampled radial MRI with multiple coils. iterative image reconstruction using a total variation constraint. *Magnetic Resonance in Medicine*, 57(6):1086–1098, 2007. 27

[57] M. Lustig, D. Donoho, and JM Pauly. Sparse MRI: The application of compressed sensing for rapid MR imaging. *Magnetic Resonance in Medicine*, 58(6):1182–1195, 2007. 27

[58] M. Doneva, P. Börnert, H. Eggers, C. Stehning, J. Sénégas, and A. Mertins. Compressed sensing reconstruction for magnetic resonance parameter mapping. *Magnetic Resonance in Medicine*, 2010. 27

[59] S. Lee, JA Fessler, and D. Noll. A simultaneous estimation of field inhomogeneity and R2* maps using extended rosette trajectory. In *Proc. Intl. Soc. Mag. Reson. Med*, page 2327, 2002. 27

[60] BP Sutton, SJ Peltie, JA Fessler, and DC Noll. Simultaneous estimation of I, Rz*, and field map using a multi-echo spiral acquisition. In *Proc. Intl. Soc. Mag. Reson. Med.*, volume 10, page 1323, 2002. 27

[61] C. Graff, Z. Li, A. Bilgin, M. Altbach, AF Gmitro, and EW Clarkson. Iterative T2 estimation from highly undersampled radial fast spin-echo data. In *Proc. Intl. Soc. Mag. Reson. Med*, volume 14, page 925, 2006. 27

[62] VT Olafsson, DC Noll, and JA Fessler. Fast joint reconstruction of dynamic $R2*$ and field maps in functional MRI. *IEEE Transactions on Medical Imaging*, 27(9):1177–1188, 2008. 27

[63] J. Fessler. Model-based image reconstruction for MRI. *Signal Processing Magazine, IEEE*, 27(4):81–89, 2010. 28

[64] H. Wilbraham. On a certain periodic function. *Cambridge & Dublin Math. J*, 3:198–201, 1848. 31

[65] M. Bôcher. Introduction to the theory of fourier's series. *The Annals of Mathematics*, 7(3):81–152, 1906. 31

[66] JW Gibbs. Fourier's series. *Nature*, 59(1522):200–200, 1898. 31

[67] JW Gibbs. Fourier's series. *Nature*, 59(1539):606–606, 1899. 31

[68] FJ Harris. On the use of windows for harmonic analysis with the discrete fourier transform. *Proceedings of the IEEE*, 66(1):51–83, 1978. 31

[69] RN Bracewell. *The Fourier transform and its applications*. McGraw-Hill series in electrical and computer engineering. McGraw Hill, 2000. 34

[70] R. Kories and H. Schmidt-Walter. *Taschenbuch der Elektrotechnik: Grundlagen und Elektronik*. Harri Deutsch Verlag, 2008. 34

[71] AC Kak, M. Slaney, IEEE Engineering in Medicine, and Biology Society. *Principles of computerized tomographic imaging*. IEEE Press, 1988. 35

[72] R. Van de Walle, HH Barrett, KJ Myers, MI Aitbach, B. Desplanques, AF Gmitro, J. Cornelis, and I. Lemahieu. Reconstruction of MR images from data acquired on a general nonregular grid by pseudoinverse calculation. *IEEE Transactions on Medical Imaging*, 19(12):1160–1167, 2000. 35

[73] KT Block. *Advanced Methods for Radial Data Sampling in Magnetic Resonance Imaging*. PhD thesis, Georg-August-Universitaet Goettingen, 2008. 35

[74] CG Koay, JE Sarlls, and E. Özarslan. Three-dimensional analytical magnetic resonance imaging phantom in the fourier domain. *Magnetic Resonance in Medicine*, 58(2):430–436, 2007. 35

[75] LA Shepp and BF Logan. The fourier reconstruction of a head section. *IEEE Trans. Nucl. Sci*, 21(3):21–43, 1974. 35

[76] LA Shepp et al. Computerized tomography and nuclear magnetic resonance. *J. Comput. Assist. Tomogr*, 4(1):94–107, 1980. 35

[77] IR Young, DJ Bryant, and JA Payne. Variations in slice shape and absorption as artifacts in the determination of tissue parameters in NMR imaging. *Magnetic Resonance in Medicine*, 2(4):355–389, 1985. 38

[78] HY Carr and EM Purcell. Effects of diffusion on free precession in nuclear magnetic resonance experiments. *Physical Review*, 94(3):630, 1954. 40

[79] S. Meiboom and D. Gill. Modified spin-echo method for measuring nuclear relaxation times. *Review of Scientific Instruments*, 29(8):688–691, 1958. 40

[80] A. Haase, J. Frahm, D. Matthaei, W. Hanicke, and K.D. Merboldt. Flash imaging. rapid NMR imaging using low flip-angle pulses. *Journal of Magnetic Resonance (1969)*, 67(2):258–266, 1986. 40

[81] J. Frahm, A. Haase, W. Haenicke, KD Merboldt, and D. Matthaei. Hochfrequenz-Impuls und Gradienten-Impuls-Verfahren zur Aufnahme von schnellen NMR-Tomogrammen unter Benutzung von Gradientenechos. *Deutsche Patentanmeldung*, page P35, 1985. 40

[82] A. Oppelt. FISP-a new fast MRI sequence. *Electromedica*, 54:15–18, 1986. 40

[83] WD. Rooney, G Johnson, X Li, ER Cohen, S Kim, K Ugurbil, and CS Springer. Magnetic field and tissue dependencies of human brain longitudinal 1h2o relaxation in vivo. *Magnetic Resonance in Medicine*, 57(2):308–318, 2007. 41

[84] N. Gelman, JR Ewing, JM Gorell, EM Spickler, and EG Solomon. Interregional variation of longitudinal relaxation rates in human brain at 3.0 T: relation to estimated iron and water contents. *Magnetic resonance in medicine*, 45(1):71–79, 2001. 41

[85] J. Hennig, A. Nauerth, and H. Friedburg. RARE imaging: a fast imaging method for clinical MR. *Magnetic Resonance in Medicine*, 3(6):823–833, 1986. 42

[86] RV Mulkern, STS Wong, C. Winalski, and FA Jolesz. Contrast manipulation and artifact assessment of 2D and 3D RARE sequences. *Magnetic resonance imaging*, 8(5):557–566, 1990. 42

[87] PS Melki, RV Mulkern, LP Panych, and FA Jolesz. Comparing the faise method with conventional dual-echo sequences. *Journal of Magnetic Resonance Imaging*, 1(3):319–326, 1991. 42

[88] PL Roux and RS Hinks. Stabilization of echo amplitudes in FSE sequences. *Magnetic resonance in medicine*, 30(2):183–190, 1993. 42

[89] RV Mulkern, PS Melki, P. Jakab, N. Higuchi, and FA Jolesz. Phase-encode order and its effect on contrast and artifact in single-shot RARE sequences. *Medical physics*, 18:1032, 1991. 43

[90] RT Constable, AW Anderson, J. Zhong, and JC Gore. Factors influencing contrast in fast spin-echo MR imaging. *Magnetic resonance imaging*, 10(4):497–511, 1992. 43

[91] J. Nocedal and SJ Wright. *Numerical optimization*. Springer verlag, 1999. 47

[92] DE Woessner. Effects of diffusion in nuclear magnetic resonance spin-echo experiments. *The Journal of Chemical Physics*, 34:2057, 1961. 60, 99

[93] S. Majumdar, SC Orphanoudakis, A. Gmitro, M. O'Donnell, and JC Gore. Errors in the measurements of T2 using multiple-echo MRI techniques. II. Effects of static field inhomogeneity. *Magnetic resonance in medicine*, 3(4):562–574, 1986. 60

[94] S. Majumdar, SC Orphanoudakis, A. Gmitro, M. O'donnell, and JC Gore. Errors in the measurements of T2 using multiple-echo MRI techniques. I. Effects of radiofrequency pulse imperfections. *Magnetic resonance in medicine*, 3(3):397–417, 1986. 60

[95] AP Crawley and RM Henkelman. Errors in T2 estimation using multislice multiple-echo imaging. *Magnetic resonance in medicine*, 4(1):34–47, 1987. 60

[96] HE Smith, TJ Mosher, BJ Dardzinski, BG Collins, CM Collins, QX Yang, VJ Schmithorst, and M.B. Smith. Spatial variation in cartilage T2 of the knee. *Journal of Magnetic Resonance Imaging*, 14(1):50–55, 2001. 61, 99

[97] TJ Mosher, Y. Liu, and CM Torok. Functional cartilage MRI T2 mapping: evaluating the effect of age and training on knee cartilage response to running. *Osteoarthritis and Cartilage*, 18(3):358–364, 2010. 61, 99

[98] RE Wendt III, PH Murphy, JJ Ford, RN Bryan, and JA Burdine. Phase alterations of spin echoes by motion along magnetic field gradients. *Magnetic Resonance in Medicine*, 2(6):527–533, 1985. 74, 78

[99] SC Park, MK Park, and MG Kang. Super-resolution image reconstruction: a technical overview. *Signal Processing Magazine, IEEE*, 20(3):21–36, 2003. 81

[100] GS Mayer and ER Vrscay. Measuring information gain for frequency-encoded super-resolution MRI. *Magnetic resonance imaging*, 25(7):1058–1069, 2007. 81

[101] M Uecker. *Nonlinear Reconstruction Methods for Parallel Magnetic Resonance Imaging*. PhD thesis, Georg-August-Universitaet Goettingen, 2009. 83

[102] KT Block, M. Uecker, and J. Frahm. Suppression of MRI truncation artifacts using total variation constrained data extrapolation. *International Journal of Biomedical Imaging*, 2008, 2008. 96

[103] J. Sénégas, W. Liu, H. Dahnke, H. Song, E.K. Jordan, and JA Frank. Fast T2 relaxometry with an accelerated multi-echo spin-echo sequence. *NMR in Biomedicine*, 23(8):958–967, 2010. 96

[104] J. Hennig. Multiecho imaging sequences with low refocusing flip angles. *Journal of Magnetic Resonance (1969)*, 78(3):397–407, 1988. 99

[105] J. Hennig. Echoes-how to generate, recognize, use or avoid them in MR-imaging sequences. part I: Fundamental and not so fundamental properties of spin echoes. *Concepts in Magnetic Resonance*, 3(3):125–143, 1991. 99

[106] V.G. and Kiselev. Calculation of diffusion effect for arbitrary pulse sequences. *Journal of Magnetic Resonance*, 164(2):205 – 211, 2003. 99

[107] Y Zur. An algorithm to calculate the NMR signal of a multi spin-echo sequence with relaxation and spin-diffusion. *Journal of Magnetic Resonance*, 171(1):97 – 106, 2004. 99

[108] NN Lukzen and AA Savelov. Analytical derivation of multiple spin echo amplitudes with arbitrary refocusing angle. *Journal of Magnetic Resonance*, 185(1):71–76, 2007. 99, 100

[109] L. Comtet. *Advanced combinatorics: the art of finite and infinite expansions*. D. Reidel Pub. Co., 1974. 99

[110] HS Wilf. *Generatingfunctionology*. A K Peters, 2006. 99

[111] A. Petrovic, E. Scheurer, R. Stollberger, and K. Yen. Improved T2-quantification with slice selective MSE-sequences. Number 2749. Proc. Intl. Soc. Mag. Reson. Med., 2010. 100, 112

[112] A. Petrovic, E. Scheurer, R. Stollberger, and K. Yen. Monte carlo analysis of T1-mixing errors for MSE T2 mapping. Number 2750. Proc. Intl. Soc. Mag. Reson. Med., 2010. 100, 106, 112

[113] LI Sacolick, F. Wiesinger, I. Hancu, and MW Vogel. B1 mapping by Bloch-Siegert shift. *Magnetic Resonance in Medicine*, 63(5):1315–1322, 2010. 109

[114] WD Rooney, JR Pollaro, SC Forbes, DJ Wang, K. Vandenborne, and GA Walter. Application of the extended phase graph technique to improve T2 quantification across sites. In *Proc. Intl. Soc. Mag. Reson. Med.*, volume 19, page 138, 2011. 112

[115] IT Jolliffe. *Principal Component Analysis*. Springer Series in Statistics. Springer, 2002. 115

[116] SB King, SM Varosi, F. Huang, and GR Duensing. The MRI eigencoil: 2n-channel snr with n-receivers. In *Proc. Intl. Soc. Mag. Reson. Med.*, volume 11, page 712, 2003. 115

[117] SB King, SM Varosi, and GR Duensing. Eigenmode analysis for understanding phased array coils and their limits. *Concepts in Magnetic Resonance Part B: Magnetic Resonance Engineering*, 29(1):42–49, 2006. 115

[118] M. Buehrer, KP Pruessmann, P. Boesiger, and S. Kozerke. Array compression for MRI with large coil arrays. *Magnetic Resonance in Medicine*, 57(6):1131–1139, 2007. 115

Curriculum Vitae

Personal Data

Name:	Tilman Johannes Sumpf
Date of Birth:	June 13, 1982 in Aachen, Germany
Sex:	Male
Nationality:	German
Degree:	Dipl.-Ing.

Education

1995 - 2002	Grotefend Gymnasium, Hann. Münden, Germany Abitur, June 2002
2002	Metallumform, Hann. Münden, Germany Technical Internship
2002 - 2008	Technische Universität (TU) Carolo-Wilhelmina, Braunschweig, Germany Studies of Electrical Engineering (Diploma)
2008	Airbus, Hamburg, Germany Diploma thesis
since 2009	Max-Planck Institute for Biophysical Chemistry, Göttingen, Germany PhD Student at the Biomedizinische NMR Forschungs GmbH

Exchange semester

2006	University of Nottingham, Nottingham, England

Professional Experience

2005	Institute for Control Engineering, TU Braunschweig, Germany Student Assistant
2005	Institut für Elektrische Messtechnik und Grundlagen der Elektrotechnik, TU Braunschweig, Germany Student Assistant
2007	Philips Research, Hamburg, Germany Technical Internship in Tomographic Imaging

List of Publications

Journal Publications

- Tilman J. Sumpf, Martin Uecker, Susann Boretius and Jens Frahm, Model-Based Nonlinear Inverse Reconstruction for T_2 Mapping Using Highly Undersampled Spin-Echo MRI. *Journal of Magnetic Resonance Imaging*, 34(2):420-428 (2011).

- Martin Uecker, Tilman J. Sumpf and Jens Frahm, Reply to: MRI resolution enhancement: How useful are shifted images obtained by changing the demodulation frequency. *Magnetic Resonance in Medicine*, 66(6):1511-1212 (2011).

Conference Contributions

- Tilman J. Sumpf, Martin Uecker, Susann Boretius and Jens Frahm, Nonlinear Inverse Reconstruction for T_2 Mapping using Highly Undersampled Spin-Echo MRI, Workshop on Novel Reconstruction Strategies in NMR and MRI. Göttingen, 2010, Poster 7.

- Tilman J. Sumpf, Martin Uecker, Susann Boretius and Jens Frahm, Nonlinear Inverse Reconstruction for T_2 Mapping from Highly Undersampled Cartesian Spin-Echo MRI. Joint Annual Meeting ISMRM Montreal 2011, In *Proc. Intl. Soc. Mag. Reson. Med.* 19 (2011):2741.

- Amir Moussavi, Martin Uecker, Tilman J. Sumpf, Roland Tammer, Jens Frahm und Susann Boretius, Real-time Multi-slice MRI of Renal Filtration in the Mouse. Joint Annual Meeting ISMRM Montreal 2011, In *Proc. Intl. Soc. Mag. Reson. Med.* 19 (2011):950.

- Tilman J. Sumpf, Amir Moussavi, Martin Uecker, Susann Boretius and Jens Frahm, Effects of phase alternations in nonlinear inverse T_2 reconstructions from undersampled data. Joint Annual Meeting ISMRM Melbourne 2012, In *Proc. Intl. Soc. Mag. Reson. Med.* 20 (2012):2400.

- Tilman J. Sumpf, Florian Knoll, Jens Frahm, Rudolf Stollberger and Andreas Petrovic, Nonlinear inverse reconstruction for T_2 mapping using the generating function formalism on undersampled Cartesian data. Joint Annual Meeting ISMRM Melbourne 2012, In *Proc. Intl. Soc. Mag. Reson. Med.* 20 (2012):2398.

- Amir Moussavi, Martin Uecker, Tilman J. Sumpf, Roland Tammer, Jens Frahm and Susann Boretius, Real-time Lung MRI of the Mouse. Joint Annual Meeting ISMRM Melbourne 2012, In *Proc. Intl. Soc. Mag. Reson. Med.* 20 (2012):3976.

Other Publications

- Tilman J. Sumpf, Realisierung eines Fluxgate-Magnetometers mit einem PSoC-Mikrocontroller, Institut für Elektrische Messtechnik und Grundlagen der Elektrotechnik, Technische Universität Carolo-Wilhelmina, Braunschweig, 2006.
- Tilman J. Sumpf, Regelung von Gebläsen in großen Transportflugzeugen (diploma thesis), Airbus Deutschland, Hamburg, 2008.
- Tilman J. Sumpf, Warum dauert eine MRT-Aufnahme so lange?, Frag den Wissenschaftler, *Extra Tip*, Göttingen, 2011.

Acknowledgments

First of all, I would like to thank Prof. Dr. Jens Frahm, head of the Biomedizinische NMR Forschungs GmbH am Max-Planck-Institut für biophysikalische Chemie, for the support of my work, extensive assistance in the preparation of manuscripts and for offering me a chance to work in this excellent research facility.

I am very grateful to Prof. Dr. Meinhard Schilling from the Institut für Elektrische Messtechnik und Grundlagen der Elektrotechnik of the Technische Universität Braunschweig for the supervision of my thesis and for the continuous support of my studies and scientific work since more than six years.

I am deeply indebted to my former colleagues Prof. Dr. Susann Boretius and Dr. Martin Uecker for uncountable discussions, encouragement, and guidance throughout the years and for the deep understanding of the topic.

Further, I would like to thank all the present and former staff members of the Biomedizinische NMR Forschungs GmbH for a very pleasant working atmosphere and numerous table-soccer sessions.

Finally I owe my deepest gratitude to my parents, family, and friends for encouraging me and for helping to keep my life in context.